

PHENIX  $\pi^0 - h^\pm$  Two Particle Correlations Measurements in 200 GeV Au+Au Collisions  
and Development of Pi0 Calibrations Technique for sPHENIX Electromagnetic Calorimeter

A dissertation presented to  
the faculty of  
the College of Arts and Science of Ohio University

In partial fulfillment  
of the requirements for the degree  
Doctor of Philosophy

S. B. Chauhan  
August 2024  
© 2024 S. B. Chauhan. All Rights Reserved.

This dissertation titled

PHENIX  $\pi^0 - h^\pm$  Two Particle Correlations Measurements in 200 GeV Au+Au Collisions  
and Development of Pi0 Calibrations Technique for sPHENIX Electromagnetic Calorimeter

by

S. B. CHAUHAN

has been approved for

the Department of Physics and Astronomy

and the College of Arts and Science by

Justin E. Frantz

Associate Professor

Matthew Ando

Dean, College of Arts and Sciences

## ABSTRACT

CHAUHAN, S. B., Ph.D., August 2024, Physics and Astronomy

---

PHENIX  $\pi^0 - h^\pm$  Two Particle Correlations Measurements in 200 GeV Au+Au Collisions  
and Development of Pi0 Calibrations Technique for sPHENIX Electromagnetic Calorimeter  
(183 pp.)

Director of Dissertation: Justin E. Frantz

We present two topics relevant to the advancement of the field of Relativistic Heavy Ion collision physics: a novel technique development for calibrating a detector in sPHENIX and a physics analysis using PHENIX data with the goal of studying the possibility of jet-quenching in so-called small collision systems. Calibrating the electromagnetic calorimeter (EMCal) of the sPHENIX experiment to the electromagnetic scale is an important task which will allow many important analyses to succeed. The established known mass of the  $\pi^0$  particle is utilized for development of a new technique to perform calibration of the PHENIX EMCal. The sPHENIX experiment uses many different methods and particles to calibrate the detectors, which complement each other. This pi0-method is one of the methods that has been used to successfully calibrate the sPHENIX electromagnetic calorimeter to its electromagnetic scale in the first sPHENIX running period 2023. The second part of this work is about studying the possibility of production of quark-gluon plasma (QGP), a state of matter that is a regular occurrence in ultrarelativistic high-energy heavy-ion collisions at RHIC and LHC. However, the same cannot be definitively said for small collision systems. However, multiple recent research results have indicated the presence of QGP formation in small collision systems. We employ an analysis of two-particle jet correlations between pi0-h particles using PHENIX data to investigate whether a jet suppression signal using the new observable  $R_I$  exists. Several small collision systems were investigated, including d+Au,  ${}^3\text{He}+\text{Au}$ , and primarily, peripheral centrality (65-70%) Au+Au collisions, which serve as proxies for small systems in terms of the number of nucleons involved during the

collision. This study focuses on the latter. Our study aims to examine the Au+Au collision system with two different system sizes: one involving nearly central collisions where QGP formation is expected, and the other involving peripheral collisions where QGP formation is still under the topic of research.

**DEDICATION**

*To my loving mother*

## ACKNOWLEDGMENTS

I would like to express my gratitude to my advisor, Justin Frantz, for his invaluable feedback and assistance throughout my Ph.D. Needless to say, without his support, this research would not have been possible. Justin always had a smile on his face and patiently explained the novice questions that I struggled with. He encouraged me to explore and learn independently, but was always available to provide clarifications when needed.

I would like to thank my dissertation committee members: Morgan L. Vis, Julie Roche, and Chaden Djalali for their time and effort and the feedback that they had to improve my work.

I am grateful to the PHENIX Collaborations for granting me access to the data used in this thesis. I am also grateful to the sPHENIX Collaboration for letting me use the simulation data and test my calibration codes on the EMCal coding framework. I also got to see the implementation of my calibration method with the real sPHENIX data collected in 2023.

I am thankful to the Department of Physics and Astronomy at Ohio University for accepting me as a graduate student, which allowed me to explore in the field of research.

Last but not least, I want to acknowledge my family for their unwavering support throughout my PhD journey.

## TABLE OF CONTENTS

	Page
Abstract . . . . .	3
Dedication . . . . .	5
Acknowledgments . . . . .	6
List of Tables . . . . .	10
List of Figures . . . . .	11
 1 Introduction . . . . .	17
1.1 Background . . . . .	20
1.2 Introduction of the Heavy-Ion Fields . . . . .	26
1.3 Quantum Chromodynamics (QCD) . . . . .	29
1.3.1 <i>Running of the Coupling Constant</i> . . . . .	33
1.3.2 <i>Experimental Evidence of QCD</i> . . . . .	35
1.3.3 <i>Perturbative QCD</i> . . . . .	37
1.3.4 <i>Lattice QCD</i> . . . . .	38
1.3.5 <i>Effective Field Theories</i> . . . . .	40
1.4 Relativistic Heavy Ion Collisions . . . . .	42
1.5 Coordinate System for Colliders of Relativistic Heavy Ions . . . . .	44
1.6 Quark Gluon Plasma . . . . .	45
1.6.1 <i>Signatures of QGP</i> . . . . .	46
1.6.1.1 Flow Behavior of QGP . . . . .	46
1.6.1.2 Jet Quenching . . . . .	47
1.6.1.3 Quarkonia Suppression . . . . .	51
1.6.1.4 Strangeness Enhancement . . . . .	52
1.6.7 Motivation of the Research . . . . .	54
 2 The Experimental Methods . . . . .	56
2.1 RHIC . . . . .	56
2.2 PHENIX . . . . .	56
2.2.1 <i>Magnets</i> . . . . .	60
2.2.2 <i>Global Detectors</i> . . . . .	61
2.2.2.1 BBC . . . . .	62
2.2.2.2 ZDC . . . . .	63
2.2.3 <i>Central Arm Detectors</i> . . . . .	64
2.2.3.1 Drift Chambers (DC) . . . . .	65
2.2.3.2 Pad Chambers (PC) . . . . .	65

2.2.3.3	Ring-Imaging Cherenkov (RICH) . . . . .	66
2.2.3.4	Electromagnetic Calorimeter (EMCal) . . . . .	68
2.2.4	<i>Software and Data Acquisition and Trigger Systems (DAQ) in PHENIX</i>	72
2.2.5	<i>Trigger Systems</i> . . . . .	73
2.2.5.1	Definition of Minimum Bias (MB) Trigger . . . . .	74
2.2.5.2	EMCal/RICH Trigger (ERT) . . . . .	74
2.2.6	<i>EMCal Clustering in PHENIX</i> . . . . .	75
2.2.7	<i>Centrality Determination in PHENIX</i> . . . . .	76
2.3	sPHENIX . . . . .	77
2.3.1	<i>sPHENIX Electromagnetic Calorimeter (EMCal)</i> . . . . .	79
3	sPHENIX Pi0 Tower-by-Tower Calibration Technique: Development and Method	83
3.1	Calibration of sPHENIX Electromagnetic Calorimeter . . . . .	83
3.2	Development of Pi0 Tower By Tower Method . . . . .	87
3.3	Basic Method Algorithm and Implementation . . . . .	89
3.4	Implementation . . . . .	91
3.5	Iterative Aspects of the Method . . . . .	93
3.6	Histogram Fitting and Small Simulation Demonstration of Method . . . . .	95
3.7	Method Extension: Eta Ring by Eta Ring Method . . . . .	101
4	sPHENIX Pi0 Tower-by-Tower Calibration Technique : Optimization and Results	104
4.1	Optimization of Kinematic Cuts for Maximizing Statistical Precision . . . . .	104
4.2	Simulation Test Results of Pi0 Tower by Tower Method . . . . .	112
4.3	Simulation and Data Results of Pi0 Eta Ring by Eta Ring Method . . . . .	118
5	PHENIX AuAu 2PC Analysis: Data Preparations and Analysis . . . . .	128
5.1	Introduction and Motivation . . . . .	128
5.2	Datasets and Preparations . . . . .	130
5.2.1	<i>Data Selections</i> . . . . .	132
5.2.2	<i>Run Selections</i> . . . . .	132
5.2.3	<i>Event Selections</i> . . . . .	133
5.2.4	<i>Particle Selections With Various Cuts</i> . . . . .	133
5.2.4.1	Shower Shape Cut: $\chi^2 < 3$ . . . . .	134
5.2.4.2	Charged Hadron Veto: $r_{emc-pe3}^{veto} < 8.0$ cm . . . . .	134
5.2.4.3	Further Single-Photon Selection Criteria . . . . .	135
5.2.4.4	Cuts on the $\pi^0$ Triggers . . . . .	135
5.2.4.5	Cuts on the Charged Hadrons . . . . .	136
5.3	Validating Our Selection Cuts With Previous Work . . . . .	138
5.4	RI-Related Analysis Details . . . . .	138
5.4.1	<i>Detector Corrections</i> . . . . .	138
5.4.2	<i>Two Particle Correlations</i> . . . . .	140
5.4.3	<i>Jet Pair Quantification</i> . . . . .	143
5.4.3.1	$I_{AA}$ . . . . .	143

5.4.3.2	$R_I$	144
5.4.3.3	Corrections Performed to $R_I$ Observable	145
5.4.4	<i>Error analysis</i>	148
5.4.4.1	Uncertainty from the Mis-Constructed $\pi^0$ Combinatorics	148
5.4.4.2	Uncertainty from ZYAM	152
5.4.4.3	Uncertainty from Bleeding Correction	153
5.4.4.4	Uncertainty from $R_{\Delta\eta}$	153
5.4.4.5	Uncertainty from the $v_n$	153
5.4.4.6	Tabulation of Systematical Uncertainties	156
6	PHENIX AuAu 2PC Analysis: Results and Discussions	158
6.1	Correlation Function and Jet Function of Baseline pp Collisions	158
6.2	Correlation Function and Jet Function of the Run-14 AuAu Collisions Data	158
6.2.1	<i>Run-14 AuAu Collisions For 20-40% Centrality Bins</i>	159
6.2.2	<i>Run-14 AuAu Collisions For 65-70% Centrality Bins</i>	162
6.3	$R_I$ Plots	164
6.3.1	<i><math>R_I</math> Plot for Run-14 With 20-40% Centrality</i>	165
6.3.2	<i><math>R_I</math> Plot for Run-14 With 65-70% Centrality</i>	165
6.3.3	<i><math>R_I</math> Plot for Run-16 Au+Au With 65-70% Centrality</i>	167
6.3.4	<i><math>R_I</math> Plot for Combined Data From Run-14 and Run-16</i>	168
6.4	Interpretation and Comparison of $R_I$ of Au+Au Collision Systems With Centrality Bins 65-70% With Previous $R_I$ Plots	170
7	Summary and Future Outlook	173
	References	175
	Appendix: List of Acronyms	179
	Appendix: Data Table for $R_I$ Observable Along With errors	181

## LIST OF TABLES

Table	Page
1.1 Fundamental Forces and its properties. . . . .	24
4.1 Comparison of $p_1$ ( $\pi^0$ fitted mean) parameter from the fit with the various possible estimator functions. . . . .	111
5.1 Comparing the number of participants for various systems [1]. . . . .	131
5.2 PHENIX Data selected for this thesis analysis. . . . .	132
5.3 Signal-to-Background (S/B) values for centrality of 20-40% and 65-70% for the $\pi^0$ trigger- $p_T$ bins of 5-7 GeV/c and 7-9 GeV/c. . . . .	149
5.4 Systematic Uncertainties for Run-14 Au+Au Collision data with Centrality bins of 20-40%. . . . .	157
B.1 $R_I$ values of Run-14 Au+Au with 20-40% centrality . . . . .	181
B.2 $R_I$ values of Run-14 Au+Au with 65-70% centrality . . . . .	182
B.3 $R_I$ values of Run-16 Au+Au with 65-70% centrality . . . . .	183

## LIST OF FIGURES

Figure	Page
1.1 The Standard Model of Elementary Particles [2]. There are mainly three groups of elementary particles namely quarks, leptons, and bosons. . . . .	21
1.2 Illustration of the number of participants and binary collisions involved during the collision of two nucleus. The red nucleons from both nucleus are considered to participate in the collisions whereas green nucleons are the spectators that pass through without any collisions. . . . .	29
1.3 The running coupling constant ( $\alpha_s$ ) of QCD as a function of the momentum transfer $Q$ . The value of coupling constant at Z boson mass is also shown [3]. . . . .	35
1.4 DIS structure function $F_2$ showing scaling behavior with momentum transfer, $Q^2$ [4]. . . . .	39
1.5 Different stages of the heavy-ion collision evolving with time increased along the horizontal axis [5]. . . . .	43
1.6 Various flow coefficients. $v_2$ (red), $v_3$ (blue), and $v_4$ (pink) for the charged hadrons vs. centrality of the collisions in Pb+Pb collisions in ALICE [6]. . . . .	48
1.7 $R_{AA}$ vs. $p_T$ in central Au+Au collisions. We can see the suppressions of the yields of $\pi^0$ (orange), $\eta$ (red) particles, and not in the case of direct photons $\gamma$ (purple) [7]. . . . .	50
1.8 Two-particle correlation study shows the suppression in Au+Au collisions seen by STAR experiment [8]. . . . .	52
1.9 Enhancement of the production of strange baryons as a function of mean number of participating nucleons in Pb+Pb collisions seen by ALICE collaboration [9]. . . . .	53
2.1 Relativistic Heavy Ion Collider (RHIC) complex at Brookhaven National Lab in Upton, NY, USA. [10]. . . . .	57
2.2 PHENIX setup during the Run 14 data-taking period. The top image shows the view along the beam line, whereas the bottom image shows from the side-view of the beam line [11]. . . . .	58
2.3 The PHENIX detector cutaway view showing majority of the sub-detectors [12]. . . . .	60
2.4 PHENIX magnetic systems showing its field lines. The beam runs along the horizontal line and collides at $z = 0.0$ m [13]. . . . .	61
2.5 PHENIX global detectors BBCs and ZDCs colored in “orange blobs”. . . . .	62
2.6 The PHENIX BBC counter [14]. (a) Each BBC array contains 64 BBC elements for both North and the South. (b) A single BBC element consists of quartz Cherenkov radiator and meshed dynode PMT. . . . .	63
2.7 PHENIX ZDC shown in the red blocks along the line of beam [15]. . . . .	64
2.8 Left: PHENIX Drift Chamber mechanical drawing. Center: Sector of a drift chamber. Right: Top view of the drift chamber with wire orientations showing U, X, and V wires [16]. . . . .	66

2.9	The cartoon depiction of the PHENIX pad chambers showing PC1, PC2, and PC3 [16]. . . . .	67
2.10	A cutaway view of one of the arms of the PHENIX RICH detector [17]. . . . .	68
2.11	A cutaway view of module of PbSc showing the alternating Pb and scintillator tiles and other components [18]. . . . .	70
2.12	The exploded view of the PbGl supermodule [18]. . . . .	71
2.13	The flow of data in PHENIX system. The Local Level-1 Trigger and Global Level-1 Trigger helps to collect the events that are of higher importance and interesting for physics analysis. . . . .	73
2.14	Left: Clock method. Right: BBC only method. They helps to determine the centrality in the PHENIX [19]. . . . .	77
2.15	Correlation of the final state observables $N_{ch}$ and the observables calculated by the Glauber Monte Carlo model [20]. . . . .	78
2.16	The cut-a-way engineering plot of sPHENIX Detector [21]. The height of the detector from the ground to the top of the rack is about 15-20 m. The beam-pipe is shown in the silver color that runs through the center of the detector which is then surrounded by several layers of detector subsystems. . . . .	79
2.17	The cylindrical shaped sPHENIX EMCal housed inside of the Inner Hadronic Calorimeter (IHCal) is being installed. The lower inset image shows the actual sPHENIX EMCal sectors being laid around the barrel shaped IHCal. The EMCal sector is shown in Figure 2.18. . . . .	81
2.18	The sPHENIX EMCal sector layout showing blocks and electronics components [22]. . . . .	82
3.1	Decay of $\pi^0$ and the possible combination of photon pairs in the case of two $\pi^0$ . True pair reflects the photons from common parent, while undesired pair forms from the pairing of photons from different parents creating huge background. . . . .	86
3.2	Basic flow-chart of the $\pi^0$ -calibration method. The top cross-line shapes are a representations of the clusters in sPHENIX EMCal. . . . .	90
3.3	Demonstration of the fit method I devised. Left: Plotting only the background part of the histogram just below and above the peak area with second degree polynomial. The idea is to gather as many good seed as possible for the later total fits of the histogram. Right: All three part of the fitting function shown together. . . . .	98
3.4	Fits on all the eta slices (or eta rings) to do the sanity checks by eye that the fits are not failing in any of the eta slices. . . . .	99
3.5	One of 192 pages of each tower fits. Each page consists of 128 fits to inspect. Quickly inspecting such plots is a good way to do the sanity checks if the fit fails or not. . . . .	100
3.6	Pi0 Tower by Tower (TbT) method applied to calibrate small 16x16 region of sPHENIX EMCal. Initially we see some decalibration shifts i.e. some kinds of pattern which is removed after few iterations. All of the towers in the final iteration aligns pi0 peak mass of 0.135 GeV. . . . .	101

3.7	sPHENIX EMCAL barrel shape representation. S and N represent the South and North direction where beamline runs through. The bottom part is the representation of the unrolled sPHENIX barrel shape. Each column is considered at eta slice i.e. eta ring with 256 towers in them. There are total of 96 eta slices in the sPHENIX EMCAL. . . . .	102
4.1	An estimator function whose shape needs to be determined. The most likely curve for the estimator function will be the blue (A) [online] as the relative error tends to increase after some lower limit on $p_T$ because too much background starts to accumulate then. The x-axis photon1 $p_T$ denotes the $p_T$ of one of the photons of pi0 decay photons. . . . .	105
4.2	Signal and background region selected using the simple side-band analysis method. Once the signal and background regions are selected we can just count use the integral function of the ROOT to calculate the counts of the signals and background values that is used later in the equations. . . . .	107
4.3	Signal vs. photon1 $p_T$ . The blue marks are the counts of signal region. The red line is a fit. . . . .	108
4.4	Background vs. photon1 $p_T$ . The blue marks are the counts from the background region. The red line is a fit. . . . .	109
4.5	An estimator function showing that there exists a optimal photon $p_T$ that minimizes the relative statistical error. Blue line is taking mass-resolution into account, and red line without the mass-resolution effect. The simple estimator function follows the data-points reasonably. . . . .	112
4.6	RMS of base level sPHENIX EMCAL response to $\pi^0$ s. Base level non-uniformities is within 2.0 %. . . . .	113
4.7	sPHENIX EMCAL 2d histogram showing the response to $\pi^0$ particles. The z-axis shows the mass value of pi0 obtained from the fits. . . . .	114
4.8	The one-dimensional histogram of the Figure 4.7. We can see that several towers near the TPC regions do not have pi0 mass values well-aligned with the target of 0.135 GeV. . . . .	115
4.9	Decalibration pattern applied to sPHENIX EMCAL which forces $\pi^0$ mass to vary from 0.11 to 0.16 GeV. The white spots are considered as the dead-towers and so those histograms won't get filled. The z-axis is the fitted $\pi^0$ mass for each towers. . . . .	116
4.10	Fitted $\pi^0$ mass values as seen by the sPHENIX EMCAL after applying the de-calibration patterns. Non-uniformities have now increased to about 5% in the EMCAL. . . . .	117
4.11	State of the calibration after 11 iterations. The non-uniformities calculated using RMS (std. deviation) has dropped to less than 0.10%. . . . .	118
4.12	Left: The 2D histogram showing how well pi0-tbt method recovered input de-calibration shifts. Right: The 1D distribution of the figure on the left. The value of 1.00 means that the final correction values almost completely recovered the input decalibration. . . . .	119

4.13 Calibration of the sPHENIX EMCal 96 slices along the $\eta$ direction using the $\pi^0$ -calibration method. The x-axis labelled “eta” is actually the etaslices along the $\eta$ directions of the sPHENIX detector. Each eta slice consists of 256 towers integrated in the $\phi$ direction embedded into them. This illustrates that the method successfully converges the mean of the pi0 for each eta slice to the target value of 0.135 GeV, even within five iterations. . . . .	120
4.14 Pi0 Peak Fits to Eta bins (2/4th of the expected statistics as indicated by zooming in on the histogram names) for Run 21813. Much less statistics were collected due to a premature end of data-taking during RHIC Run year 2023 because of an accelerator component breaking. Although there were less statistics, the fitting method were able to fit the data without any failure. This also indicates that our method is robust. . . . .	121
4.15 First fitting of pi0 peak locations at the start of the pi0 method steps of the calibration procedure, for runs 9613 and 21813. . . . .	123
4.16 Fitting after indicated number of iterations demonstrating readjustment of the pi0 peak locations (gaus fit means) from the method converging to the value of the 165 MeV input which in this case was chosen as the target mass value instead of 135 MeV for reasons explained in the text. . . . .	125
 5.1 Comparing $R_l$ observable between d+Au and ${}^3\text{He}+\text{Au}$ collision systems from PHENIX experiment [1]. The two systems demonstrate the dependence of QGP formation that scales with system sizes, with larger systems exhibiting greater suppression due to the formation of a larger QGP (medium) as compared to the smaller system. . . . .	129
5.2 Comparisons of the total correlation functions between our dataset with Run-14 Au+Au with 20-40% centrality and Anthony Hedges [16] same run year with same centrality analysis result. The similar structures of the correlation function verifies our selection cuts and the analysis methods are working as expected. . .	139
5.3 Illustration of the two particle correlation study [1]. . . . .	140
5.4 PHENIX $\Delta\eta$ acceptance corrections vs. the jet widths for near-side and away-side. For the near-side, the function looks linear whereas for the away-side corrections is the constant value [23]. . . . .	147
5.5 $\pi^0$ invariant mass distribution for $AuAu$ in Centrality 20 – 40 % (Top row), and 65 – 70 % (Bottom row). The first column is for pi0 pT bins of 5-7 and the second column is for pi0 pT bins of 7-9. The signal-to-background (S/B) is calculated by dividing the integrals of the blue signal line by the red background line. The integral is calculated within the two green lines, which is also the nominal acceptance region $\pi^0$ chosen for this analysis. . . . .	150

5.6 Comparisons of yields ( $R_I$ ) for the nominal pi0 region and the side-bands region in the case of 20-40% centrality. Left: The red line is a constant fit line showing the average $R_I$ for high- $p_T$ points to be at $0.5097 \pm 0.04858$ using the $\pi^0$ nominal region of selection. Right: The red line shows the fit to the high- $p_T$ values of $R_I$ showing the average value at $0.5031 \pm 0.077$ for the $\pi^0$ from the side-band regions from the $\pi^0$ nominal region. . . . .	151
5.7 Comparisons of yields ( $R_I$ ) for the nominal pi0 region and the side-bands region in the case of 65-70% centrality. The plot on the left shows the average $R_I$ for the last three high- $p_T$ points to be $1.079 \pm 0.1802$ using the red fit line. It is the plot for $\pi^0$ in the nominal $\pi^0$ region of selection. The right plot shows the fit line average value for high- $p_T$ points to be at $0.4338 \pm 0.2589$ . It is the plot for $\pi^0$ from the side-bands region of the $\pi^0$ nominal range. . . . .	152
5.8 The charged hadron higher-order flow coefficients $v_2$ , $v_3$ , and $v_4$ from the ATLAS experiment [24]. The x-axis shows the centralities from the range of 0 to 80% range for the flow coefficients. . . . .	154
5.9 The systematics due to the effect of $v_3$ coefficients on the final $R_I$ values are calculated by making the $R_I$ plots with and without $v_3$ terms used in the calculations. The systematic error values are calculated and shown for each data points. . . . .	156
 6.1 Correlation function between $\pi^0$ -hadrons in the Run-15 p+p collision data. Trigger $p_T$ bins: [5.0-7.0, 7.0-9.0] GeV/c going along the top to the bottom. Partner $p_T$ bins: [0.6-1.0, 1.0-2.0, 2.0-3.0, 3.0-5.0 and 5.0-7.0] GeV/c going along the left to right. The red line represents the total fit to the correlation function whereas purple line is the fit to the background level. . . . .	159
6.2 Jet function between $\pi^0$ -hadrons in the Run-15 pp collision data. Trigger $p_T$ bins: [5.0-7.0, 7.0-9.0] GeV/c going along the top to the bottom. Partner $p_T$ bins: [0.6-1.0, 1.0-2.0, 2.0-3.0, 3.0-5.0 and 5.0-7.0] GeV/c going along the left to right. . . . .	160
6.3 Correlation function between $\pi^0$ -hadrons in the Run-14 AuAu collision data with centrality bins of 20-40%. Trigger $p_T$ bins: [5.0-7.0, 7.0-9.0] GeV/c going along the top to the bottom. Partner $p_T$ bins: [0.6-1.0, 1.0-2.0, 2.0-3.0, 3.0-5.0 and 5.0-7.0] GeV/c going along the left to right. The red line is the fit to the total correlation function whereas the purple line represents the fit to the background. . . . .	161
6.4 Jet function between $\pi^0$ -hadrons in the Run-14 AuAu collision data with centrality bins of 20-40%. Trigger $p_T$ bins: [5.0-7.0, 7.0-9.0] GeV/c going along the top to the bottom. Partner $p_T$ bins: [0.6-1.0, 1.0-2.0, 2.0-3.0, 3.0-5.0 and 5.0-7.0] GeV/c going along the left to right. . . . .	162

6.5	Correlation function between $\pi^0$ -hadrons in the Run-14 AuAu collision data with centrality bins of 65-70%. Trigger $p_T$ bins: [5.0-7.0, 7.0-9.0] GeV/c going along the top to the bottom. Partner $p_T$ bins: [0.6-1.0, 1.0-2.0, 2.0-3.0, and 3.0-5.0] GeV/c going along the left to right. The red line represents the fit to the total correlation function whereas the purple line represents the fit to the background level. . . . .	163
6.6	Jet function between $\pi^0$ -hadrons in the Run-14 AuAu collision data with centrality bins of 65-70%. Trigger $p_T$ bins: [5.0-7.0, 7.0-9.0] GeV/c going along the top to the bottom. Partner $p_T$ bins: [0.6-1.0, 1.0-2.0, 2.0-3.0, and 3.0-5.0] GeV/c going along the left to right. . . . .	164
6.7	$R_I$ plot of 20-40% Centrality bins of Run-14 Au+Au data with Run-15 p+p data as the baseline. The red line shows the straight line fit to obtain the average value of $R_I$ for the high- $z_T$ . The average fit value is shown at $0.510 \pm 0.049$ . The vertical lines represent the statistical error and the systematic errors are shown as the box around the points. . . . .	166
6.8	$I_{AA}$ as a function of hadron $p_T$ for Run-14 Au+Au 20-40% centrality bins [16] used to compare with our $R_I$ observable with the same centrality and trigger $p_T$ bins of 5 – 7 GeV/c and 7 – 9 GeV/c. . . . .	167
6.9	$R_I$ plot of 65-70% Centrality bins of Run-14 Au+Au data with Run-15 p+p data as the baseline. The red line shows the straight line fit to obtain the average value of $R_I$ for the high- $z_T$ . The average value is shown at $1.038 \pm 0.125$ . The vertical lines represent the statistical error and the systematic errors are shown in the boxes. . . . .	168
6.10	$R_I$ plot of 65-70% centrality bins of Run-16 Au+Au data with Run-15 p+p data as the baseline. The red line shows the straight line fit to obtain the average value of $R_I$ for the high- $z_T$ . The average values is shown at $1.045 \pm 0.212$ . The vertical lines represent the statistical error and the systematic errors are showin the boxes. . . . .	169
6.11	RI plot for combined statistics from Run-14 and Run-16 datasets for the centrality bins of 65-70%. The average fit value of $1.055 \pm 0.123$ is shown by the red line. . . . .	170
6.12	$R_I$ plot for ${}^3\text{He}+\text{Au}$ reproduced from [1] with more directly comparable new averaging range ( $z_T > 0.25$ ) for comparison to Run-14 and Run-16 datasets 65-70% result. The red-line shows the constant fit to the high $z_T$ points. The average $z_T$ shows the value of $0.877 \pm 0.038$ . The statistical errors are shown by the lines while systematical errors are shown by the boxes. . . . .	171

## 1 INTRODUCTION

The exploration of the fundamental building blocks of nature and their interactions to form observable matter has been a long-standing pursuit of humanity. The prevailing understanding is that the universe originated from an event called “the Big Bang” approximately 13.8 billion years ago. In the immediate aftermath of this event within the few microseconds after the Big-Bang, it is believed that the universe existed in a state known as the Quark-Gluon Plasma (QGP). The QGP is hypothesized to consist of the most fundamental particles known as “quarks” and “gluons,” which constitute the building blocks of all baryonic matter in our surroundings.

While direct access to the quarks and gluons of the early universe is not possible, scientists have devised methods to create QGP in laboratory settings here on Earth. The data for this thesis work have been derived from the Relativistic Heavy Ion Collider (RHIC), which is a facility designed to generate QGP and study it. In order to recreate the QGP state, two highly energetic particles are accelerated in opposite directions to nearly the speed of light within a circular beam. These particles collide at specific locations along the beam pipe, where state-of-the-art detectors are strategically placed to study the resulting “debris” produced after the collision takes place. By conducting thorough examinations of the resultant particles, scientists are able to confirm the production of QGP and provide insights into its characteristics.

Our objective in this thesis is to deepen our understanding of the QGP state of matter by investigating an experimental probe that contains information about their interactions with QGP matter. Various types of probe have been extensively examined to quantify the extent of their interaction with QGP previously. Specifically, probes containing the “color” charge engage with the QGP, which also possesses color charges, resulting in the loss of energy by the probes to the medium. It is these mechanisms by which the high- $p_T$  probes loose energy to the QGP medium that are interesting to us. When the various ways in which

probes lose energy and processes are understood, it tells about the QGP medium itself. By studying the characteristics of these probes and their interactions with QGP, we can obtain valuable insight into the nature of QGP itself. Different types of probes provide different kinds of information about the QGP medium.

In this thesis, we used the method called two-particle correlation analysis (discussed briefly in 1.6.1.2) of  $\pi^0$  particles that are high- $p_T$  probes, as well as charged hadrons as partners or associated particles. The reasons for choosing these particular pairs of particles for analysis will be explained in Section 5.2.4. By examining the correlations between these two particles in collision events, where they are correlated by the same physical phenomena, i.e. the same hard-scattering processes, we can gain valuable information regarding the fundamental nature and behavior of the QGP medium.

Initially, it was believed that QGP matter could only be formed when heavy ions collided in the colliders. This was because heavy ions contain a significant number of nucleons, which generate the high temperatures (about 170 MeV) and energy densities (1 GeV/fm<sup>3</sup>) required to create QGP. However, subsequent research indicated that QGP matter might also be generated in smaller collision systems. Although there are debates of the exact nature of the QGP found in these small systems as compared to the large systems of collisions. Signs of QGP signatures in such small collision systems were first observed in high-multiplicity proton-proton ( $p - p$ ) collisions at LHC [25]. In fact, our research group led by Justin Frantz at Ohio University has already investigated several such small collision systems such as  $dAu$  [26] and  ${}^3HeAu$  [1] and have found some hints for the possibility of such an extreme medium produced in these systems, although smaller in sizes. These studies were conducted to explore the possibility of QGP formation and to characterize the resulting QGP matter, if formed, in small collision systems. The findings of these investigations contribute to the growing body of evidence suggesting that hot QCD matter with similarities to QGP could be created in small collision systems, expanding our understanding of QGP

formation beyond traditional heavy-ion collisions. One of the detailed reviews on the small collision systems done by James Nagle and William Zajc [27] covers a lot more information for interested readers.

In this thesis, we studied the collision system of AuAu in two centrality bins (discussed in detail in 2.2.7), i.e. 20-40% and 65-70%. The 20-40% centrality bin is more central in collisions where we expect QGP formations, whereas in the 65-70% centrality bin it is more like peripheral collisions between AuAu nuclei, where we do not know whether QGP should exist or not. Our aim is to compare the 65-70% bin results with Pun's PhD thesis [1] because of the similar system sizes during the collisions.

Additionally, this thesis also contains the development of a calibration method of the sPHENIX electromagnetic calorimeter (EMCal, hereafter). The sPHENIX work is also part of service work for graduate students to be allowed to use the data for their PhD analyses from PHENIX and sPHENIX Collaborations. Following the completion of the PHENIX experiment [28] in 2016, it was decommissioned to make way for a new experiment known as sPHENIX [29]. Unlike PHENIX, which had detector arms extending towards the east and west sides only, and not towards up or down, and with limited pseudorapidity reach and incomplete azimuthal coverage, sPHENIX features a barrel-shaped detector design to overcome PHENIX limitations. The sPHENIX experiment also offers increased luminosity, enabling faster triggering and the capture of larger volumes of data. Additionally, sPHENIX has a broader kinematic reach and pseudorapidity coverage compared to PHENIX. One notable addition to sPHENIX is the inclusion of hadronic calorimeters, which were not present in PHENIX. These calorimeters play a crucial role in measuring the energy of hadronic particles. The first operations of sPHENIX started in the summer of 2023, where the initial focus was to do the commissioning of the detectors and to make it ready for future physics runs. Subsequent years will see higher luminosity runs, during which a substantial amount of physics data will be collected. These runs will form the basis for extensive data

analyses and investigations into various research topics ranging from understanding the jets to QGP properties to the fundamentals of QCD theory. The main emphasis during the initial stage will be on the successful functioning and calibration of the detector, while the subsequent higher-luminosity runs will provide the bulk of the data for in-depth physics studies.

This thesis is organized as follows. The following sections will introduce briefly the fundamental theory of strong force called QCD, QGP matters, heavy-ion collision physics, jets, and jet quenching mechanisms. These are crucial topics for understanding the overall physics of heavy-ion collisions. Chapter 2 gives explanations of the experimental detectors and their working mechanisms. Chapter 3 describes the development of the calibration method for the sPHENIX electromagnetic calorimeter. Chapter 4 describes further optimization of the calibration method along with some results. Chapter 5 will have the preliminary analysis techniques set up for the two-particle correlation study, and Chapter 6 contains the results together with the discussions. Finally, in Chapter 7 a brief summary and the future outlook are discussed.

## 1.1 Background

Everything we perceive in our daily lives is made up of matter particles, mainly protons, neutrons, and electrons. On a macroscopic scale, numerous matter particles have been identified and characterized on the basis of their distinctive properties such as charge, mass, and spin (a quantum property of particles). However, as we delve into the realm of the quantum world, it becomes apparent that all observed entities within our visible universe are constructed from only a handful of fundamental particles. These particles are referred to as “fundamental” because they are not composed of any smaller constituent particles according to current understanding. These fundamental particles are organized systematically in a structure known as “the Standard Model”, which can be visualized as

a table-like arrangement. The Standard Model encapsulates our current understanding of elementary particles and their interactions, and it provides a framework that categorizes the various types of fundamental particles and organizes them into groups based on their properties and behavior. Figure 1.1 illustrates the arrangement of these particles in the Standard Model.

## Standard Model of Elementary Particles

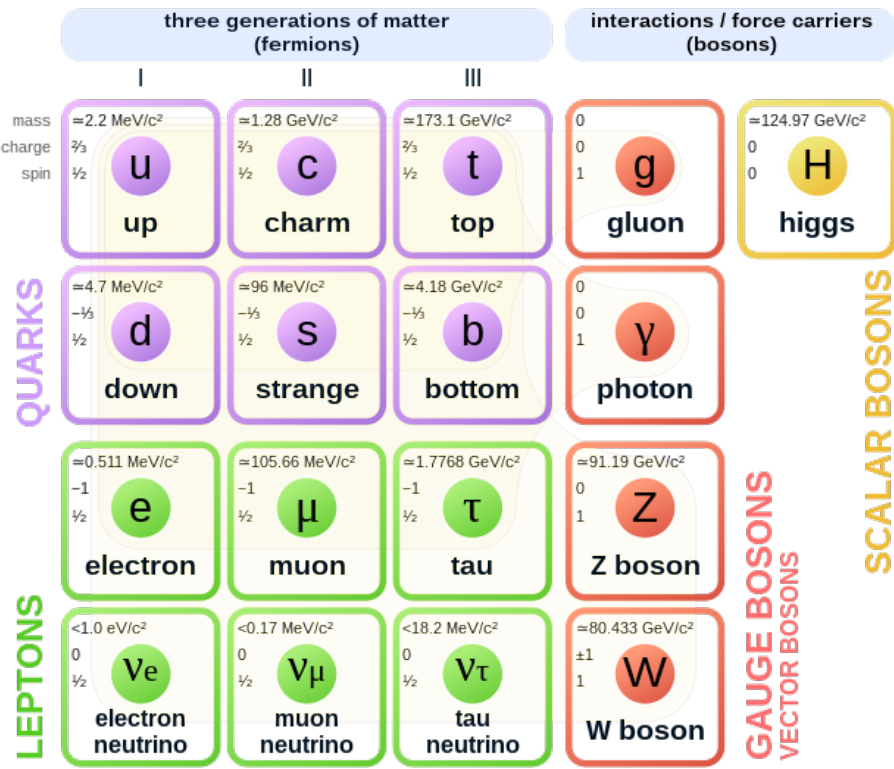


Figure 1.1: The Standard Model of Elementary Particles [2]. There are mainly three groups of elementary particles namely quarks, leptons, and bosons.

The discovery and detection stories of individual particles are indeed fascinating to study by themselves, and many articles and textbooks, such as Griffith's "Introduction to Particle Physics" [30], provide comprehensive accounts of these narratives. As discussed

above only the particles listed in the Standard Model are fundamental in nature as far as our state-of-the-art instruments/detectors can tell us. The Standard Model particles can be broadly divided into two types i.e. Fermions and Bosons. Fermions are particles that have half-integral spins and include quarks and leptons. Bosons have integral spins. The concept of quarks was first introduced by Gell-Mann and Zweig independently in 1964 introducing a model called the “Quark Model” [31]. The quark model would become the first model that arranges the myriad of particles discovered in early times. Scientists needed an explanation to nicely arrange this ever-increasing number of new particle discoveries. Quarks and leptons come in three generations with increasing masses from generation I to generation III. Most baryonic matter is made up of only a few fundamental particles, especially the up quark, down quark, strange quarks, and electrons. The higher generation, i.e. heavier particles, are unstable, and even if they are formed under some suitable conditions, they will not last long enough to form any stable matter around us. If we focus on the quarks part of the Standard Model, they possess electric charges but in the fractional units of electron charge. The fractional units of each quark when added to make matter particles namely baryons which contain three quarks ( $qqq$ ) will as a whole add up to an integer unit of electric charge, and mesons which contain a quark and antiquark ( $q\bar{q}$ ) also add up to the integral unit of electric charge. Quarks are fermions, and they are spin-1/2 particles. One peculiar property of the quarks is that they are involved in the strong nuclear interactions and possess a “color” charge in them. Each quark, for example the up  $u$  quark, can be in three flavors of color, i.e. red, blue, or green. The combination of three colors in baryons and a color and an anticolor in mesons makes them color neutral in a whole. The concept of color saved the Standard Model because otherwise some of the hadrons (another name for particles that can be either baryons or mesons) like the Delta baryon ( $\Delta^{++}$ ) are made up of all three up  $u$  quarks like ( $uuu$ , and this would violate the Pauli exclusion principle, which states no two quantum particles can occupy the same quantum state. In this case, the up quarks are all the

same except for the color quantum number. Three up quarks have to be of different colors to make them color neutral as a whole.

Now focusing on lepton's properties, we can see electron  $e^-$ , muon  $\mu$ , and tau  $\tau$  possess electric charges but their partner neutrinos namely electron neutrino  $\nu_e$ , muon neutrino  $\nu_\mu$ , and tau neutrino  $\nu_\tau$  don't. Leptons are also Fermions and so they are spin-1/2 particles. Neutrinos are among the weakly interacting particles that doesn't want to interact with other matter particles. Neutrinos could pass right through the earth and not interact with any of the matters on its way.

Finally, the third types of elementary particles in the Standard Model are the bosons. Bosons are the particles that mediate the interaction among the particles. For example, gluons mediates strong interactions that involve color-containing particles. This interaction is called a strong nuclear force because it is the strongest of all the forces in nature. However, the range of strong force is very small, i.e. in the quantum scale. The strong force is the reason nuclei are stable, otherwise the electromagnetic force between the like charges in atoms should already explode atoms and should have never been stable. Electromagnetic force is the force mediated by another type of boson, called the photon ( $\gamma$ ) which mediates the electric charge interactions among the particles. Another type of interaction that the standard model explains is the weak nuclear force and those are mediated by  $W^\pm$  and  $Z^0$ . All bosons have integral spins, where gluons, photons, and  $W^\pm$  and  $Z^0$  have spin 1. The spin 0 nature of the Higgs boson or the Higgs field is a required feature in order to provide masses to the fundamental particles when they interact with the Higgs field. In the Standard Model, the vacuum contains the condensate of the Higgs bosons, and they are color and charge neutral. That means it will not interact with the gluons and the photons, only other gauge boson ( $W^\pm$ ) and  $Z^0$ , quarks and leptons interact with the condensate and thus gains mass. There is one caveat to the standard model, it does not include gravitational force. This means we don't know the quantum scale of the gravitational interactions like

we do for other types of interactions. In the subatomic realm, it is not yet understood how the gravitational force behaves or whether it exhibits quantization like other forces. To understand how particles interact through the exchange of bosons, it is necessary to observe the behavior of forces in real-life scenarios. On a macroscopic scale, Newton's equations of motion can be used to predict the movement of objects like cars. However, at the atomic level, quantum mechanics must be employed. In this realm, the wavefunction  $\psi$  can be used to measure and predict how a system will evolve. Unfortunately, the Schrodinger equation, which describes the motion of a system, is not invariant under Lorentz transformations and therefore cannot be used to accurately describe subatomic particles. Instead, relativistic quantum mechanics field theory must be employed at this scale, using complex notation such as 4-vectors and energy-momentum relations in "natural units"  $c = \hbar = 1$ . Note that the masses of photons in this theory are not actually always zero; they can also be "virtual photons" that possess all the properties of real photons except that they can carry any mass, including negative or imaginary values. This allows for the equations describing particle collisions to be balanced. Quantum gravity is an active area of research. This limitation of the Standard Model begs new physics that extends beyond the Standard Model.

Table 1.1: Fundamental Forces and its properties.

Force	Particles Affected	Strength	Range	Boson
Strong	Quarks and Gluons containing particles	1	$10^{-15}$ m	gluon
Electromagnetic	Electrically charged particles	$10^{-2}$	$\infty$	photon
Weak	All particles	$10^{-13}$	$10^{-18}$ m	$W^\pm, Z^0$
Gravitational	All particles	$10^{-38}$	$\infty$	graviton (?)

We briefly discussed the different fundamental forces of nature, and so it is worth showing the table here that nicely summarizes these fundamental forces of nature and its properties as shown in Table 1.1. The strength of the strong force is taken to be 1, and the strength of the other forces is shown compared to the strong force. Although quarks were an established concept that nicely explained the nice organizations of the ever-growing particles zoo of the discovery, no evidence of direct observations of the quarks was present. This means that many scientists would not believe quark theory, and they would comment that quarks are some mathematical tricks to satisfy the needs for an explanation for the growing number of particle discoveries. Even though the deep inelastic scattering experiments at Standard Linear Accelerator Center (SLAC) had established that inside protons there are small lumps and that was named “partons” - a combined name, still used, for quarks and gluons, skeptics were still not convinced that something like quarks exists as it could not be independently found. The supporter of the quark model argued that quarks cannot be found independently because of the “confinement”. Confinement means that only color-neutral baryons and mesons can be found independently in nature. Individual color quarks or gluons are confined together to form colorless entities.

For the quark model to be accepted by all, discovery of a heavy meson particle called  $J/\psi$  played a huge role. It was discovered in the month of November in 1974 by the two independent groups, one from Brookhaven National Laboratory who named it the  $J$  part and another from the SLAC group who named it the  $\psi$  part, and this event is now famously known as “the November revolution”. The  $J/\psi$  meson was exceptionally heavier, electrically neutral, and had a longer life. The existence of  $J/\psi$  that contains charm  $c$  and anti-charm  $\bar{c}$  quarks meant that the symmetrical number of generations of quarks and leptons is possible according to the assumptions of the quark model, because only few of the quark types namely up  $u$ , down  $d$ , strange  $s$  were initially discovered when the quark model was put forward. Soon other types of quark, bottom quark  $b$  would be discovered in a similarly

heavier meson called bottomonium composed of  $b\bar{b}$ . Top quarks on the other hand is too heavy to combine to form mesons or baryons, because it would decay almost instantly after its formation. The discovery of top quark took long time but its discovery would make the leptons and quarks numbers symmetrical.

After a brief overview of the historical developments of the Quark Model leading to the acceptance of the Standard Model, and scientists searching physics beyond the Standard Model; I would now like to discuss some of the important topics that are relevant for the further development of our understanding in this thesis in a more detailed and structured way.

## 1.2 Introduction of the Heavy-Ion Fields

Heavy-ion physics itself is about 40 years old. The first discovery of the sub- nuclear particles began its journey from the discovery of electrons in about 1900, then protons in about 1920, and neutrons in about 1930. By the time we reach 1960, the floods of many of these subnuclear particles are seen in our discovery lists. Before we learned about quarks as we do today, we had another theory called ‘Hagedorn’ theory, which basically means that no nuclear particle is fundamental and in this sense all of these are equal. They were interacting through the exchange of other hadrons. This theory was working almost perfectly until we reached the higher energy and mass of the particles in the spectrum. This is the time that we require quarks and gluons into the scene at higher energy levels. The confirmation of quarks is verified via various processes such as the DIS experiments, the discovery of  $J/\psi$  at BNL and SLAC. Quarks were widely accepted by 1975. Lattice QCD is a theory that allows calculations that provide a modern understanding of low-energy QCD and quarks and gluons. This is the non-perturbative regime of the QCD. Here, we discretize the spacetime into the lattice-like structure, and the separation of the lattice points ensures that the ultraviolet divergence does not occur and can be avoided. At the end, of the model

calculations, however, you will take the limit of the separations to be zero, this way we try to be as close to reality as possible. Around 150 MeV, we can see the deconfinements and the partonic degrees of freedom. So many types of experiments began to search for these deconfined states of matter using various types of detector system possible, including TPCs, single-arm spectrometers, etc. It was known that if this QGP existed, then it would be very short-lived. If found, do we have the probe that went through the QGP and has brought us the information. of the QGP, what to look for in the final states of the system that has produced QGP? Two early things were proposed; one is that the production of strangeness (or strange particles) is enhanced and  $J/\psi$  suppression occurs. Chiral symmetry is restored in the QGP phase, and then the strange quarks arise due to this and manifest themselves as strangeness enhancements. The suppression of the heavy quarkonia occurs because the radius of these particles is larger than the screening length of the color charge of the QCD and hence the two heavy-quark radii are larger and they cannot see each other, meaning they do not form a quarkonia due to screening of the color charges, and so we see the suppressions of the heavy quarkonia, such as J/Psi, formations. During the RHIC runs, one of the fundamental physics they observe is the azimuthal asymmetry of the collisional particles based on the geometry of the collisions. Most of the non-central collisions are asymmetric in azimuth, i.e. in the transverse momentum distribution of the produced particles. This transfer of the asymmetry (i.e. initial geometrical shape of the collisions) to the momentum space helps us to provide a measure of the strength of the collective flow, which in turn tells us about the QGP itself. If the QGP were to be more towards the ideal gas state, then the mean free path of the particles would be too large and the particles would stream out isotropically (equally coming out from all directions) irrespective of the initial collisional geometry, and that would mean that the system would have no memory of the asymmetry of the initial state of the collisions. However, since we saw that there are larger particle density gradients, larger pressure gradients, larger momentum anisotropy in the system,

it was discovered to be more towards the ideal liquid i.e. that would have the zero mean free path in the hydrodynamic limit. QGP phase is a near-perfect liquid. To quantify flow asymmetry, we used the Fourier expansion of the angular distribution of the particles where  $v_n$  is the amplitude of the  $n$ -th harmonic of the transverse momenta from a large fraction of the particles in a single event. In the mid-rapidity collision region ( $\theta = 90^0, \eta = 0$ ) the contribution of  $v_1 \sim 0$  and the asymmetry are given almost exclusively by  $v_2$ . Here,  $v_2$  signifies the elliptic flow or  $n = 2$  coefficient. And, experimentally, at low  $p_T$ , we see large  $v_2$  due to the hydrodynamic limit. The assymmetries in these observable outgoing particle flows measured as these finite  $v_n$  values are the flow effects we see, and theorist can successfully predict it using the hydrodynamic model.

Another study we do is to study the  $R_{AA}$ , which is the nuclear modification factor and is defined as:

$$R_{AA} = \frac{(dN/dp_T)_{AA}}{\langle N_{coll} \rangle (dN/dp_T)_{pp}} \quad (1.1)$$

In the example collision shown in Figure 1.2 we can see that the colored-red nucleons (online) are the nucleons that will participate in the collision between the two nuclei. Other light green-colored spectators will be those who fly away from each other without interaction. But to scale these collisions, if we see it in terms of "binary" collisions, we can have a total of 12 binary collisions ( $3 \times 4 = 12$  possibilities). This means that in the hard-scattering processes where the high transverse momentum  $p_T$  particles are produced, we expect that in the absence of the QGP formations we should get the particle productions as scaled by the binary nucleon collisions. Therefore, we look for the nuclear modification factors  $R_{AA}$  to be less than 1, as a signature of QGP formation, the suppression of the particles occurred due to the formation of QGP.

$R_{AA}$  is defined as the yield of certain  $p_T$  particles in heavy-ion collisions to the yield of the same  $p_T$  particles in  $pp$  collisions, which is scaled by the number of binary collisions.

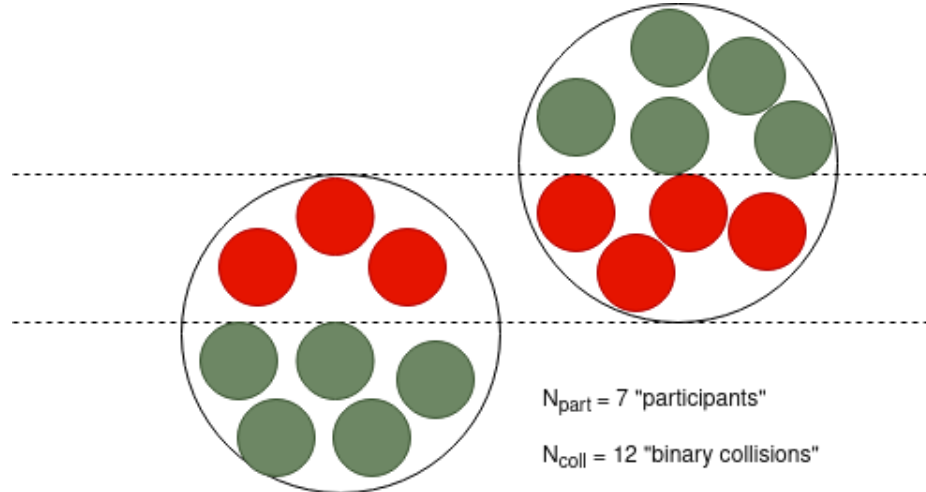


Figure 1.2: Illustration of the number of participants and binary collisions involved during the collision of two nucleus. The red nucleons from both nucleus are considered to participate in the collisions whereas green nucleons are the spectators that pass through without any collisions.

$R_{AA} = 1$  means there are no QGP formations and hence no effect on particle production during the collision. If we go to the peripheral collisions, we see that at high- $p_T$ ,  $R_{AA}$  is towards the limit of 1, meaning there is no suppression of the particles going on, and at the most central collisions, we see the suppression, i.e.  $R_{AA} < 1$ . This means that the partons have lost energies because of the dense QGP matter formed in the collision.

### 1.3 Quantum Chromodynamics (QCD)

As discussed in Section 1.1, there are 4 fundamental forces in nature. Of which, the strong nuclear force is the main topic that this thesis revolves around, so I will discuss the strong force in a somewhat more detailed way.

In 1935, Yukawa proposed that the strong nuclear force between nucleons could be explained by the exchange of a particle called a pion, which has a mass between that of a

proton and an electron. Initially, non-relativistic potential models were used to describe nuclear processes and were successful to some extent. These models represented the potential between nucleons as attractive at larger distances and repulsive at closer distances. However, as experiments moved towards the relativistic regime, these non-relativistic potentials were found to be inadequate. This led to the development of a quantum field theory of strong interactions, known as quantum chromodynamics (QCD). Like other theories, QCD is associated with certain symmetries. At the most fundamental level, QCD requires the existence of chiral symmetry. However, in the baryonic world, chiral symmetry is broken, resulting in particle masses modifications. The QCD formalism is based on the theory of groups  $SU(3)$ . Gell-Mann played a crucial role in the early development of QCD, introducing the concept of the “Eightfold Way” to classify particles, which ultimately led to the formulation of the Quark model. The arrangement of baryons and mesons suggested that baryons are composed of three “quarks” while mesons are composed of quarks and antiquarks. The term “quarks” was coined by Gell-Mann, although their existence was initially met with skepticism due to a lack of experimental evidence. Even Richard Feynman referred to them as “partons” when the SLAC experiment on  $ep$  deep-inelastic scattering produced results. Bjorken observed that this reaction follows a scaling law, where the cross section depends only on the ratio  $x$ , which is the square of the mass of virtual photons divided by the energy transfer to the nucleon multiplied by the nucleon mass. This ratio can vary from zero to one. This and similar scaling behavior indicated that the reactions were due to elastic scattering from partons that were fermions, which was consistent with the idea of quarks.

The color hypothesis, introduced by Gell-Mann, was necessary to explain how three otherwise identical quarks could combine to form certain baryons. Without this hypothesis, the Pauli exclusion principle, which states that identical quantum particles cannot occupy the same states, would have been violated. The three combinations of up quarks ( $uuu$ ),

which are present in the delta baryon  $\Delta^{++}$ , consist of three up quarks  $u$  with an additional “color” charge that differentiates them. It is important to note that the term “color” used here does not refer to the colors that we perceive in everyday life. The color hypothesis was cleverly formulated to ensure that the total possible color charges a particle can possess are “red,” “green,” and “blue.” When these colors are combined, the resulting object is colorless. Similarly, when three different colors are combined with a quark  $u$  in the case of  $\Delta^{++}$ , the resulting baryons are color neutral. The concept of color confinement is one of the reasons why we do not observe color particles such as quarks or gluons in isolation.

Unlike QED, which describes the interaction between particles carrying electric charges, QCD is a more complex field theory due to the presence of color charge. In QED, the boson that mediates the interaction, known as the photon ( $\gamma$ ), does not carry electric charges and therefore does not interact with itself. However, in QCD, the boson that mediates the interaction, known as gluons ( $g$ ), carries color charges and thus interacts with itself. This self-interaction of gauge bosons makes QCD calculations significantly more complex. QCD is also referred to as a non-Abelian gauge field. Another characteristic of QCD is “asymptotic freedom,” which suggests that quarks and gluons, when probed at very short distances, behave almost like free particles, exhibiting weak interactions among themselves at high-energy and short-distance scales. The discovery of the  $J/\psi$  meson played a crucial role in the formal development of QCD within the physics community, ultimately leading to the establishment of the Standard Model. Theories of addressing strong interactions were already becoming a requirement in 1973 [32].

The Lagrangian of QCD is defined as follows:

$$\mathcal{L}_{QCD} = -\frac{1}{4}F_{\mu\nu}^A F^{A\mu\nu} + i\bar{q}\gamma^\mu \left( \partial_\mu + ig_s \frac{1}{2} \lambda^A A_\mu^A \right) q - \bar{q}_R M q_L - \bar{q}_L M^\dagger q_R - \theta_w \quad (1.2)$$

The gluons are described by the gauge field  $A_\mu^A$  which belongs to the color group  $SU_c(3)$  and  $c$  runs from 1 to 8 (there are 8 types of colored gluons),  $g_s$  is the corresponding coupling constant. The field strength tensor is given by  $F_{\mu\nu}^A$  and is defined by

$$F_{\mu\nu}^A = \partial_\mu A_\nu^A - \partial_\nu A_\mu^A - g_s f_{ABC} A_\mu^B A_\nu^C \quad (1.3)$$

where  $f_{ABC}$  are the structure constants of the  $SU(3)$  group. The Dirac fields  $q$  represent various quark flavors, as  $q = u, d, s, c, b, t$  and  $q_R = \frac{1}{2}(1 + \gamma_5)q$ ,  $q_L = \frac{1}{2}(1 - \gamma_5)q$  are their right- and left-handed components.  $\lambda^A$  are  $3 \times 3$  Gell-Mann matrices that act on the color label and also satisfy the following commutation relation.

$$[\lambda^A, \lambda^B] = 2if_{ABC}\lambda^C \quad (1.4)$$

and, the Dirac matrices  $\gamma^\mu$  operate on the spin index. The compact form of the QCD Lagrangian as shown in Equation 1.2 hides the labels for the flavors or quarks, the color of the quarks and gluons, and the spin indexes. The mass matrix  $M$  acts on the flavor index. The constant  $\theta$  is referred to as the vacuum angle and  $w$  refers to the density of the winding number defined as

$$w = \frac{g_s^2}{32\pi^2} F_{\mu\nu}^A \tilde{F}^{A\mu\nu} \quad (1.5)$$

where  $\tilde{F}^{A\mu\nu} = \frac{1}{2}\epsilon^{\mu\nu\rho\sigma}F_{\rho\sigma}^A$  is the dual of the field strength.

If we consider a simple case where the electroweak interactions are turned off and the three lightest quarks ( $u, d, s$ ) are treated as massless, and the remaining others as infinitely heavy, then the Lagrangian contains a single parameter  $g_s$  which can be considered as the net color of a quark. The quark color depends on the radius of the region considered, and from the perturbation theory, the color in a sphere of radius  $r$  grows logarithmically as

$$\alpha_s \equiv \frac{g_s^2}{4\pi} = \frac{2\pi}{9|\log(r\Lambda)|} \quad (1.6)$$

It is interesting to note that quantum field theory, specifically quantum chromodynamics (QCD), includes a dimensionful quantity called  $\Lambda$ . This intrinsic scale is responsible for the appearance of divergences. In a simple model of massless light quarks, the couplings of the  $u$ ,  $d$ , and  $s$  quarks to the gauge field are identical. This implies that the QCD Lagrangian in this massless quark model is invariant under  $SU(3)_R \times SU(3)_L$ , where left- and right-handed components can undergo independent flavor rotations. This gives rise to the chiral symmetry discussed earlier. The breaking of chiral symmetry from the assumption of massless quark flavors to the inclusion of quark masses is a complex process, and some progress has been made through Lattice QCD (discussed further in Section 1.3.4). However, in the real world, the lightest quarks do have masses, so the Lagrangian of QCD is only approximately invariant under chiral rotations. The masses of the up ( $u$ ), down ( $d$ ), and strange ( $s$ ) quarks serve as parameters for the breaking of chiral symmetry. However, as long as these masses are smaller than the intrinsic QCD scale ( $\Lambda$ ), the approximate symmetry principles can be applied to simplify the calculations. Additionally, the quark masses can be seen as a perturbation that can be neglected in a first-order approximation, resulting in the simplest case of massless light quarks that obey chiral symmetries.

### 1.3.1 *Running of the Coupling Constant*

The Lagrangian for Quantum Chromodynamics (QCD) describes two distinct regions: one where quarks and gluons are nearly free from interactions at small distances or high-energy transfers, resulting in a small coupling constant; and another where the distance scale is larger or energy transfer is smaller, leading to confinement and a larger coupling constant. This implies that the coupling constant is not a fixed quantity, as its name suggests, but rather a running coupling constant that changes with energy. The potential behaves like

the Coulomb potential at small distances, but exhibits confinement at intermediate distances. The potential that satisfies these conditions can be expressed as follows.

$$V(r) = -\frac{\alpha_s}{r} \left\{ 1 - \frac{r^2}{a^2} \right\} \quad (1.7)$$

where  $a$  is the scale of the linear potential. We can see a linear potential above that means that as the distance at intermediate scale increases between the color charges, the potential increases sharply giving rise to another pair of quark-antiquark pair rather than quarks separating freely. Hence we have confinement.

The behavior of the coupling constant with respect to momentum transfer can be seen in Figure 1.3.

The change in the coupling constant  $g_s$  as a function of renormalization mass  $\mu$  is given by the beta function  $\beta(g_s)$ :

$$\mu \frac{d}{d\mu} g_s(\mu) = \beta(g_s) \quad (1.8)$$

In perturbation theory, the beta function for QCD becomes:

$$\mu \frac{d}{d\mu} g_s(\mu) \simeq -\frac{1}{16\pi^2} \left( 11 - \frac{2}{3} n_f \right) g_s^3(\mu) \quad (1.9)$$

The term with “11” is due to the self-interaction of the gluons, and thus the asymptotic freedom is manifested.  $n_f$  is the number of different flavors of quarks. The energy dependence of the coupling constant can be shown in terms of the QCD scale parameter  $\Lambda$  as:

$$\alpha_s(\mu^2) \simeq \frac{4\pi}{\left( 11 - \frac{2}{3} n_f \right) \ln \left( \frac{\mu^2}{\Lambda^2} \right)} \quad (1.10)$$

The value of the coupling constant  $\alpha_s$  at the mass of the  $Z$  boson was calculated quite precisely, which turns out to be  $\alpha_s = 0.1189 \pm 0.0010$ . Finally, after a few of the experimental

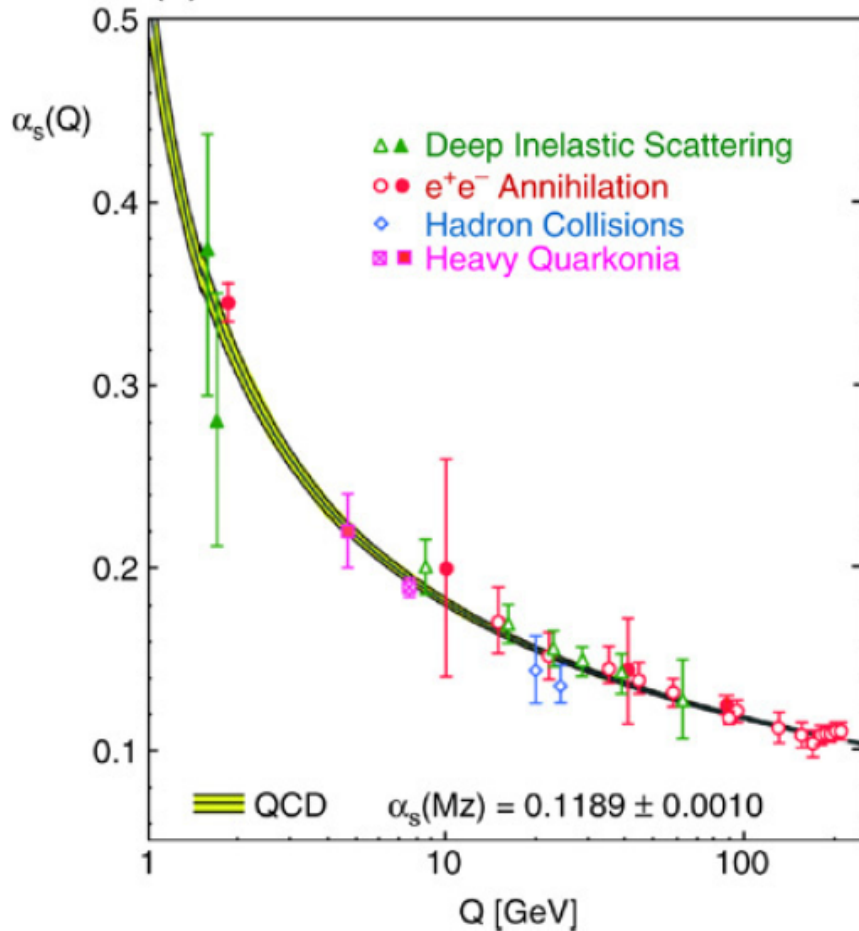


Figure 1.3: The running coupling constant ( $\alpha_s$ ) of QCD as a function of the momentum transfer  $Q$ . The value of coupling constant at Z boson mass is also shown [3].

discoveries of the quark jets and gluon jets, the QCD theory became a well-accepted theory of the strong interactions.

### 1.3.2 Experimental Evidence of QCD

As briefly mentioned in Section 1.1, the inability to observe independent quarks led to skepticism among scientists, who sought alternative theories to explain strong interactions. However, the discovery of  $J/\psi$  mesons in 1974 by two independent groups, known as

“the November Revolution”, ultimately convinced the scientific community to believe in QCD as the theory of strong interactions. The  $J/\psi$  particle is a bound state of charm and anti-charm quarks ( $c\bar{c}$ ). Subsequently, the search for the remaining quarks, bottom ( $b$ ) and top ( $t$ ), was undertaken in order to achieve symmetry between quarks and leptons in the Standard Model (see Figure 1.1). The discovery of these heavier quarks further supported theories about QCD, leading to a consensus within the scientific community that QCD, the Quark Model, and ultimately the Standard Model, provide the best explanation for most interactions. However, it is worth noting that the Standard Model does not yet integrate gravitational interactions or account for the quantum behaviors of gravity. Consequently, researchers are exploring physics beyond the Standard Model to address these and other limitations.

The  $ep$  scattering experiment conducted at SLAC confirmed the existence of quarks within a proton. In high-energy electron-positron annihilation, a quark and an antiquark can be generated. These quarks move away from each other at nearly the speed of light. However, since independent quarks do not exist, they fragment into two jets of hadrons, which are observed as sprays of particles resulting from the hard-scattering of the partons. The first observation of jets occurred in 1979 at the DESY collider and later at the LEP collider at CERN. Quarks, when they have sufficient energy, can emit gluons during the fragmentation process. This leads to the formation of three-jet events, consisting of two quark jets and one gluon jet, as seen in the process  $e^+e^- \rightarrow q\bar{q}g$ . Such three-jet events were also observed at DESY and CERN in 1979. In modern colliders like the LHC at CERN and RHIC at Brookhaven, the formation of three-jet events or even more jets is a routine occurrence. Furthermore, from the  $e^+e^-$  annihilation reaction, the ratio of the cross sections of the hadron and the production of  $\mu^+\mu^-$  indicates that the number of colors must be 3 ( $N_c = 3$ ) to satisfy other calculations. This ratio, denoted as  $R$ , is defined as:

$$R = \frac{\sigma_{e^+e^-} \rightarrow \text{hadrons}}{\sigma_{e^+e^-} \rightarrow \mu^+\mu^-} \quad (1.11)$$

The development of the Standard Model involved the contributions of numerous physicists and colliders. One such collider, the Stanford Linear Accelerator Center (SLAC), holds significant historical significance. In 1965, SLAC became the first accelerator to unveil the constituents within the proton. Through deep inelastic scattering experiments involving electrons and protons, SLAC successfully identified the presence of lighter quarks ( $u, d, s$ ).

$$e^- + p \rightarrow e^{-'} + X \quad (1.12)$$

The final bound state hadron particles produced in a collision are represented by  $X$ . Following the discovery of quarks and gluons through experimental evidence from different laboratories worldwide, the next question that naturally arose was: What governs the magnitude of the interactions ( $g_s$ ) between quarks and gluons?

### 1.3.3 Perturbative QCD

QCD is a well-established theory and is recognized as the Quantum Field Theory (QFT) that describes strong interactions. There are two regimes in QCD, namely perturbative QCD (pQCD) and non-perturbative QCD (Lattice QCD), which are distinguished based on the distance scales involved. At high energies (small distances), pQCD methods can be applied. In this regime, our calculations can be expanded as a power series using a small expansion parameter (QCD coupling). Including more terms in the expansion increases the accuracy of our results. The power expansion is possible because the coupling constant becomes smaller at small distance scales due to the asymptotic freedom of the partons, which refer to quarks and gluons. On the other hand, at low energies (large distances), the coupling constant becomes large, preventing us from expanding in a power series. In such cases, we have

to rely on computationally intensive methods, as discussed in Section 1.3.4, to obtain the answers. In this regime, we are dealing with the degree of freedom of hadrons. The pQCD regime is applicable to “hard” processes, which involve interactions between hadrons where the exchange of energy-momentum between the partons is larger than the QCD confinement scale. Examples of such processes include  $e^-e^+$  annihilation, deep-inelastic lepton-hadron scatterings, the production of heavy quarks and their bound states, and the production of high transverse momentum photons and hadron jets. The confinement of colored partons inside a nucleon is considered a “soft” (low-energy) process, as they are easily screened by the sea of partons that emerge from the vacuum. However, when the momentum transfer ( $q^2$ ) is sufficiently large, we can probe the colored partons at small distances.

$$x = -\frac{q^2}{2(q.P)} \quad (1.13)$$

In  $ep$  collisions,  $P$  represents the total momentum of the proton, while  $x$  denotes the fraction of proton momentum carried by the parton that is struck ( $x \simeq p_{\text{part}}/P$ ). According to the Bjorken hypothesis, the likelihood of finding a specific parton within the nucleon is unaffected by the momentum transfer  $q^2$ . However, this hypothesis only holds true as  $q^2 \rightarrow \infty$ , at which point the proton disintegrates to form other hadrons in the final state. Under these extreme conditions, when we examine the interior of protons, we observe that the colored partons behave almost like independent entities. This phenomenon is illustrated in Figure 1.4, where the structure function  $F_2$  remains unchanged even as the momentum transfer  $q^2$  increases from 1 to 6. Consequently, we do not observe any further interactions among the nearly independent colored partons within a nucleon.

### 1.3.4 Lattice QCD

Wilson proposed the Lattice QCD in 1974 [33] as a means to describe non-perturbative interactions in QCD, specifically in situations where the momentum transfer is low during

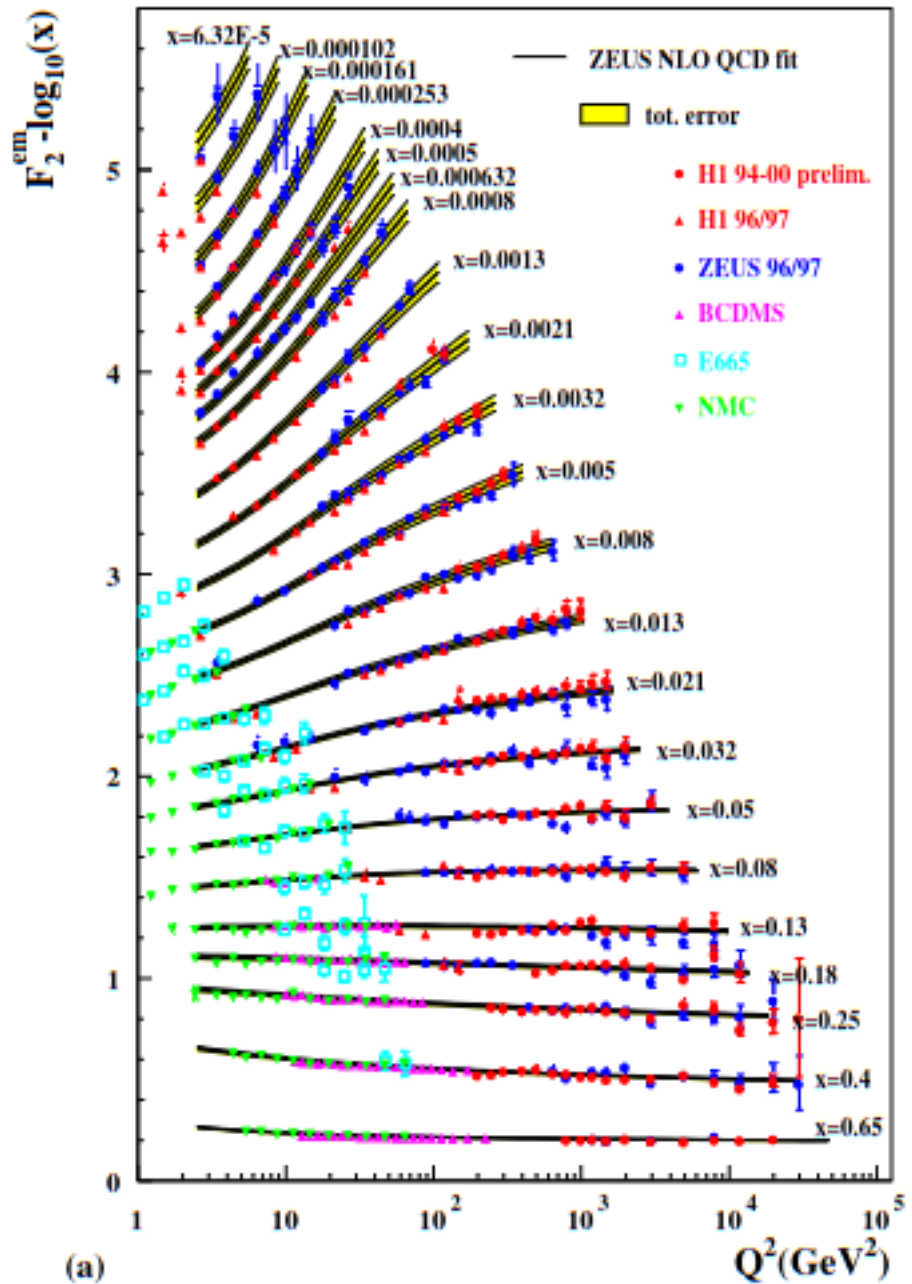


Figure 1.4: DIS structure function  $F_2$  showing scaling behavior with momentum transfer,  $Q^2$  [4].

particle scattering. Lattice QCD is a numerical approximation of QCD that captures the confinement-deconfinement transition, which occurs when the coupling constant ( $\alpha_s$ ) is large and perturbation methods cannot be applied. However, one limitation of lattice QCD is that it cannot be applied at non-zero baryon chemical potential ( $\mu_B$ ), requiring the net baryon density to be zero during the transition. This condition implies that all available baryons are strongly coupled to each other, resulting in a higher coupling constant that is suitable for the lattice QCD approach. Lattice QCD may still be applicable at small  $\mu_B/T$ . For large  $\mu_B$ , where there is an abundance of net extra baryons, a perturbative approach with a lower coupling constant is used.

Lattice QCD provides a first-principles, non-perturbative description of the strong interactions in QCD. It achieves this by discretizing space-time into a cubic lattice with a spacing of  $a$ , and using regularization to handle any infinities that arise during the calculations. Numerical simulations using Monte Carlo methods are employed in Lattice QCD. In order to obtain the final hadronic results, the regulator ( $a$ ) needs to be removed by carefully adjusting the bare parameter scales using a renormalization scheme. However, Lattice QCD is computationally demanding due to the need to incorporate all interactions, including sea quark effects, electromagnetic interactions, and isospin breaking, in addition to the minimum interactions of valence quarks and gluons. Despite these challenges, Lattice QCD has been successful in accurately predicting hadron masses and coupling constants using numerical techniques based on first principles.

### **1.3.5 *Effective Field Theories***

When there is a significant separation of energy scales in a problem, effective field theories (EFT) can be a valuable tool. Different EFTs exist for various energy and temperature scales. In the context of QCD, EFTs have been successfully applied to extend low-energy hadronic physics, specifically through chiral perturbation theory. This theory

serves as a foundation for Nucleon-Nucleon interactions up to 200 MeV. EFTs are also employed to study high-temperature QCD, enabling systematic calculations of the equation-of-state for a high-temperature quark-gluon plasma (QGP). Additionally, they allow for the calculation of QCD equations of state near the temperature at which phase transition occurs to form QGP. More in-depth explanations of the different types of EFTs can be found in literature such as [34]. For the purpose of this thesis, I will provide a brief overview of the relevant EFTs.

Chiral perturbation theory (ChPT) is an effective field theory (EFT) that provides an explanation for the physics of hadrons. It is specifically designed for low-energy scales, where the relevant degrees of freedom are the hadrons themselves rather than the underlying quarks and gluons. In the calculations within ChPT, the expansion amplitudes terms are based on the light-quark masses and momenta. Weinberg developed an extended version of ChPT, known as chiral effective field theory (ChEFT). ChEFT incorporates the concept of spontaneous symmetry breaking of Quantum Chromodynamics (QCD) and employs an effective Lagrangian that describes the interactions of pions and nucleons. In addition to hadrons, EFTs are also utilized to describe nonequilibrium systems, such as the Quark-Gluon Plasma (QGP) that is of interest in this thesis. While the QGP is considered to be locally thermalized, as a whole, it can be treated as a non-equilibrium system. Relativistic hydrodynamics provides a well-defined framework for understanding such systems. When considering hard probes, such as high- $p_T$  jets or heavy quarkonium, they can be treated as the non-equilibrium component that interacts with the thermal equilibrium environment of soft particles. As a result of these interactions, the hard probes lose a significant amount of their original energy to the medium. These interactions play a crucial role in characterizing the QGP, as the probes are sensitive to the transport properties of the medium, including the diffusion coefficient and the jet broadening or transport parameter  $\hat{q}$ .

## 1.4 Relativistic Heavy Ion Collisions

Heavy ions are characterized by having a large number of nucleons within their nuclei. When all of the electrons are removed through a series of electron-stripping processes, the remaining entity is referred to as an ion. In particle colliders, various ions are utilized, such as proton ( $p$ ), deuterium ( $^2H$ ), helium-3 ( $^3He$ ), copper ( $Cu$ ), gold ( $Au$ ), lead ( $Pb$ ), and others. With the exception of proton, deuterium, and helium-3, the remaining species are considered to be heavy ions. Collision data is available for most combinations of these species, encompassing light-light, light-heavy, and heavy-heavy ion collisions. This field of study is commonly referred to as heavy ion collision physics.

Two ion beams are accelerated to ultra-relativistic energies in a circular beampipe of a particle accelerator. These ions are then steered to collide at specific points around the beam-pipe. When the collision is head-on and involves a large momentum transfer between two partons from opposite nucleons, it can be calculated using the perturbative approach mentioned in 1.3.3. The two partons involved in the collision have high energy and are directed in opposite directions. However, because of confinement, the individual partons cannot separate, and the energy involved is sufficient to generate additional partons in a process known as a parton shower. These showers, also known as jets, are further discussed in section 1.6.1.2. As the showers or jets evolve, they start to lose energy and the process of hadronization begins. At this stage, the coupling between the partons is strong, and bound-state final particles start to form. Perturbative approaches are no longer applicable for calculations. Various jet reconstruction algorithms are available, which aim to distinguish the initial parton (quark flavor or gluons) that evolved into a jet in hadron-hadron or heavy-ion collisions. The different stages of heavy-ion collisions, from the initial collision to the formation of final-state hadrons, are briefly described below.

The two ions that collide and are accelerated close to the speed of light experience Lorentz contraction, appearing flattened like pancakes before the collisions due to their

relativistic speed. When the collision involves sufficient energy density and temperature, it can produce QGP. However, this state is short-lived and subsequently undergoes a series of evolutions, eventually hadronizing into the final state hadrons. This process is illustrated in Figure 1.5.

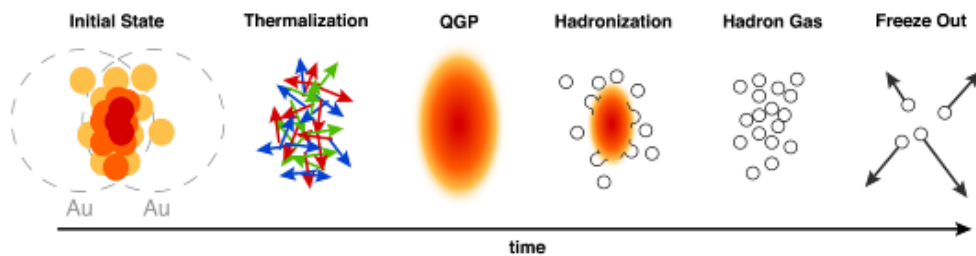


Figure 1.5: Different stages of the heavy-ion collision evolving with time increased along the horizontal axis [5].

In the initial state, two ions approach each other with a relativistic speed, resulting in the center-of-mass energy achieved by the collider. Understanding the initial state is crucial for understanding the subsequent stages of the heavy-ion collision. During collision, the nuclei of the colliding ions interact, generating a significant amount of energy within a small region. This leads to the creation of an environment suitable for the formation of the Quark-Gluon Plasma (QGP). The collision of multiple partons locally thermalizes a region of the collision, leading to the formation of the QGP. The QGP then expands and cools down, eventually transforming into hadrons through a process known as “hadronization”. Hadronization can occur through two main mechanisms: “recombination” and “fragmentation”. Recombination involves the combination of deconfined partons that have undergone thermalization and slight cooling, resulting in the formation of bound-state hadrons. Some partons with sufficient energy may separate from the main bulk matter, forming hadrons or hadron gas if many are formed in the low-energy regime. Eventually the entire volume is converted into hot

gas of hadrons. The final stage of the collision involves the cessation of collisions among the hadrons. The termination of inelastic collisions halts the formation of new hadrons, known as "chemical freezeout", while the termination of elastic collisions is referred to as "kinetic freezeout". The final-state particles then travel to the detector subsystem, where they interact with the detector materials and are detected.

## 1.5 Coordinate System for Colliders of Relativistic Heavy Ions

In order to describe many aspects of both the experimental and also descriptive physical details of relativistic heavy ion (RHI) collisions, it is useful to define a basic coordinate system. In particle physics generally a few different coordinate systems are used to define particle trajectories. As most RHI physics of interest currently focuses on data being collected at one of two colliders which work with two colliding beams as described in the previous section, we use a coordinate system based on the direction of the two beams which move in straight parallel overlapping lines (therefore, a single overlapping straight line) near whatever detectors are being used. Thus we use this line to define the z-direction of a 3D coordinate system. We use the typical three polar coordinate directions of  $z$  ( $-\infty \rightarrow \infty$ ),  $\phi$  ( $0 \rightarrow 2\pi$ ) and  $\eta$  ( $-\infty \rightarrow \infty$ ), where  $\eta$  is called the pseudorapidity, also referred to as the English name of the greek letter symbol, "eta". A polar coordinate system usually uses a  $\theta$  angle in place of this  $\eta$  variable, but these two variables are closely related since  $\eta$  is defined as

$$\eta = -\ln(\tan(\theta/2)) \quad (1.14)$$

where  $\theta$  is the angle between the beam line and any point, and thus it can range from 0 to 180 degrees which correspond to  $\eta = \pm\infty$  respectively.

Thus a value of zero pseudorapidity defines directions perpendicular to the beam, while finite, increasing values of pseudorapidity indicate directions more and more towards

either beam, either in one direction (positive values) or the other (negative values). Another variable that is almost numerically identical to pseudorapidity called rapidity  $y$  defined as  $y = \frac{1}{2} \ln \left( \frac{E+p_z}{E-p_z} \right)$  is also used to describe this direction in the field of RHI.

## 1.6 Quark Gluon Plasma

When two particles with a lot of energy collide in a particle collider such as RHIC, they create a hot and dense substance called a quark-gluon plasma (QGP). Unlike in smaller nucleons or hadrons, quarks and gluons in the QGP are free to roam around the much larger volume of the whole QGP. QGP is a strongly coupled substance that behaves like a nearly perfect fluid with low viscosity. To create QGP, collisions must have an energy density of about  $1 \text{ GeV/fm}^3$  and a critical temperature of around  $170 \text{ MeV}$ . The term QGP was introduced by Shuryak to describe matter with high temperature or high density, where asymptotic freedom and the possibly the restoration of chiral symmetry become apparent. After some time, the QGP reaches a state of local thermal equilibrium. It is believed to have formed in the early universe shortly after the Big Bang, within microseconds. QGP can be formed under two different conditions: high temperatures, as in the early universe and in colliders, and high densities, as possibly in the cores of neutron stars.

The use of a hydrodynamic models is suitable for describing the fluid-like nature of the Quark-Gluon Plasma (QGP). The final-state hadron formation and particle flow behavior are influenced by the initial geometry of the collision. In particular, the dominant factor in the production of final-state hadrons is the flow parameter  $v_2$ . This parameter is proportional to the number of valence quarks, indicating that the QGP consists of quarks and gluons. This observation further supports the presence of quarks and gluons within the QGP. The phenomenon of high- $p_T$  jets losing energy to the QGP is commonly referred to as "jet quenching". The degree of energy suppression in the jets can be quantified using the observable defined above called  $R_{AA}$ . This observable is defined as the ratio of final-state

hadron formations in heavy-ion collisions (with mass number  $A$ ) to that in  $pp$  collisions, taking into account the collision geometry by scaling to the number of binary collisions.

### **1.6.1 *Signatures of QGP***

The QGP matter that is created during heavy-ion collisions has a temporary existence, and only the final bound-state hadrons are detected by the detector components. The formation of QGP matter needs to be inferred from the detected final-state hadrons. There are several important signatures that indicate the formation of QGP matter, which are discussed below:

#### **1.6.1.1 *Flow Behavior of QGP***

Particle flow in quark-gluon plasma (QGP) refers to the coordinated movement of the constituent quarks and gluons within the QGP. The quarks and gluons in the QGP interact strongly and can move together as a unified entity, similar to the flow of atoms in a liquid or gas. The asymmetry in energy deposition during collisions, caused by fluctuations in the nucleons within the colliding ions and the noncentral collision geometry, leads to a pressure gradient. As a result, particles moving in-plane are boosted compared to those moving out-of-plane. This initial-state anisotropy is reflected in the final-state anisotropic momentum distribution of the final-state particles. The investigation of particle flow in QGP is a vibrant field of research in high-energy particle physics, as it offers insights into the behavior of quarks and gluons at high temperatures and densities, as well as the strong force that binds them within protons and neutrons. By examining the flow patterns of particles produced in heavy-ion collisions, scientists can gain a better understanding of the properties of QGP and its behavior under extreme conditions. Various techniques can be employed to study particle flow in QGP, including measurement of flow harmonics (such as elliptic flow and higher-order harmonics), analysis of particle correlations, and use of hydrodynamic models to describe the collective motion of particles. These techniques provide valuable

information on the transport properties of QGP, such as its viscosity and other transport coefficients. The distribution of final-state particles can be described using the Fourier expansion formula, as shown below:

$$E \frac{d^3N}{d^3p} = \frac{d^2N}{2\pi p_T dp_T dy} \left( 1 + \sum_{n=1}^{\infty} 2v_n \cos[n(\phi - \Phi_R)] \right) \quad (1.15)$$

where  $\phi$  represents the azimuthal angle,  $E$ ,  $p$ ,  $p_T$ ,  $y$ , and  $\Phi_R$  denote energy, momentum, transverse momentum, rapidity and reaction plane angle, respectively. Rapidity can also be defined as  $y = \frac{1}{2} \ln \left( \frac{E+p_z}{E-p_z} \right)$ , where  $p_z$  represents the longitudinal momentum. The Fourier coefficients  $v_n$  are expressed as follows:

$$v_n(p_T, y) = \langle \cos[n(\phi - \Phi_R)] \rangle \quad (1.16)$$

The absence of sine terms is due to the reflection symmetry in relation to the reaction plane. The flow coefficients are influenced by various factors, such as the energy, species, beam energy, and rapidity of the particles. The first harmonic coefficient, denoted as  $v_1$ , represents the direct flow or the radial flow of the final-state particles. On the other hand, the second harmonic coefficient, denoted  $v_2$ , represents the dominant elliptic flow observed in noncentral collisions. Lastly, the third harmonic coefficient, denoted as  $v_3$ , represents the triangular flow. Figure 1.6 shows the measurements of  $v_2$ ,  $v_3$ , and  $v_4$  for charged hadrons obtained from ALICE experiments. These measurements, which were conducted using fluid hydrodynamic models, provide evidence that QGP matter behaves like a fluid.

### 1.6.1.2 Jet Quenching

When two partons from colliding ions collide head-on at very high energy, it is referred to as hard scattering. In this process, the two partons move in opposite directions in the transverse plane with a high amount of energy to sustain the process. Since partons cannot exist independently, a new quark-antiquark pair is formed during their separation. This

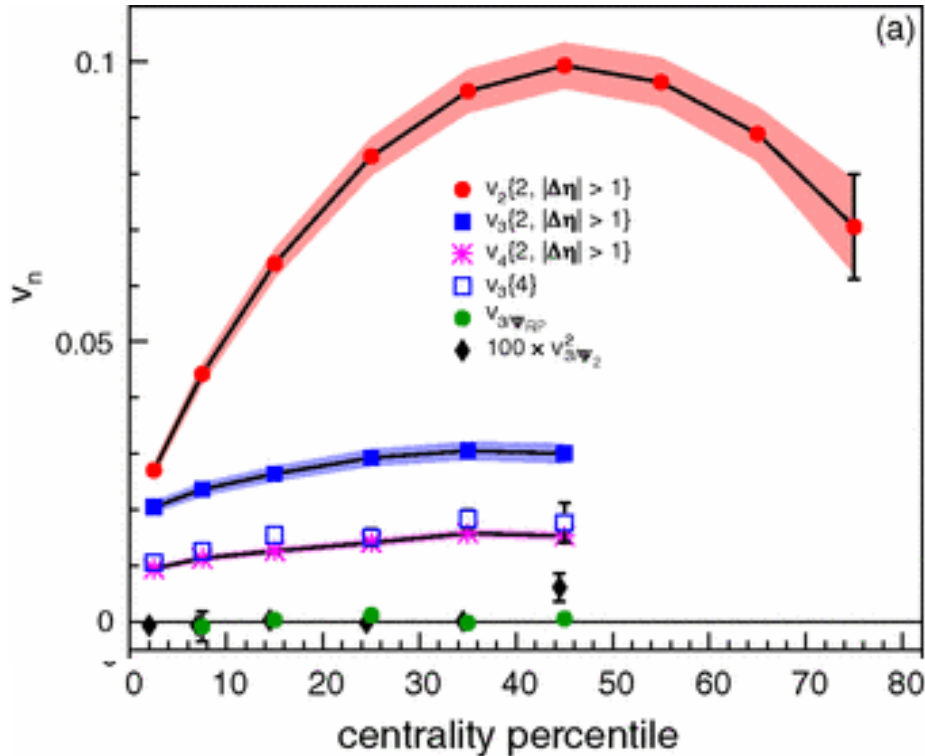


Figure 1.6: Various flow coefficients.  $v_2$  (red),  $v_3$  (blue), and  $v_4$  (pink) for the charged hadrons vs. centrality of the collisions in Pb+Pb collisions in ALICE [6].

process of pair creation continues until there is enough energy. As a result, the original parton moving in opposite directions forms a concentrated spray of particles, known as a "jet". Jet quenching occurs when the energy of a jet is reduced as it passes through a dense medium, typically the Quark-Gluon Plasma (QGP). This energy loss can happen through various mechanisms, including collisional energy loss (where the quarks and gluons in the jet collide with those in the QGP and transfer some energy), radiative energy loss (where the quarks and gluons in the jet emit gluons as they pass through the QGP), and elastic energy loss (where the quarks and gluons in the jet scatter off the quarks and gluons in the QGP). The study of jet quenching in heavy-ion collisions is an active research field, as it offers

insights into the properties of the QGP, the strong force, and the behavior of quarks and gluons at high temperatures and densities, as well as their interactions with the strong force.

There are numerous experimental measurements that indicate the occurrence of jet quenching in HI collision events. A few of these are elaborated upon below:

**Nuclear Modification Factor ( $R_{AA}$ ):** The nuclear modification factor ( $R_{AA}$ ) already defined above in Equation 1.1 is employed to quantify the phenomenon of jet quenching in collisions involving heavy ions. It is calculated as the ratio of the number of single inclusive hadrons produced in a heavy ion collision to that in a proton-proton collision, scaled by the number of binary collisions in the heavy ion collision.

The average number of nucleon-nucleon collisions in a single nucleus-nucleus collision is denoted as  $\langle N_{coll} \rangle$ . The parameter  $R_{AA}$  serves as a valuable tool in investigating jet quenching. It allows for a comparison between the number of jets produced in heavy ion collisions and the number of jets produced in proton-proton collisions on an equal basis. By comparing these quantities, researchers can determine if jet production is suppressed (indicating jet quenching) or enhanced (indicating jet enhancement) in heavy ion collisions. Additionally, the value of  $R_{AA}$  can be used to quantify the extent of jet quenching or enhancement, as well as to study the influence of variables such as jet energy and collision centrality. The Figure 1.7 illustrates the suppression of hadron yields as measured by  $R_{AA}$ .

A value of 1 for  $R_{AA}$  indicates that there is no suppression of hadrons in the collisions, while a value below unity suggests that suppression of hadrons has occurred. The suppression of  $\pi^0$  and  $\eta$  in Figure 1.7 is a result of the interaction between the color entities of the hadrons and the color charges of quarks and gluons in the medium. On the other hand, direct photons, being electrically neutral particles, do not possess color charges and therefore do not experience suppression. Other variations of nuclear modification factor observables, such as  $I_{AA}$  and  $R_I$ , exist and will be discussed further in subsequent chapters.

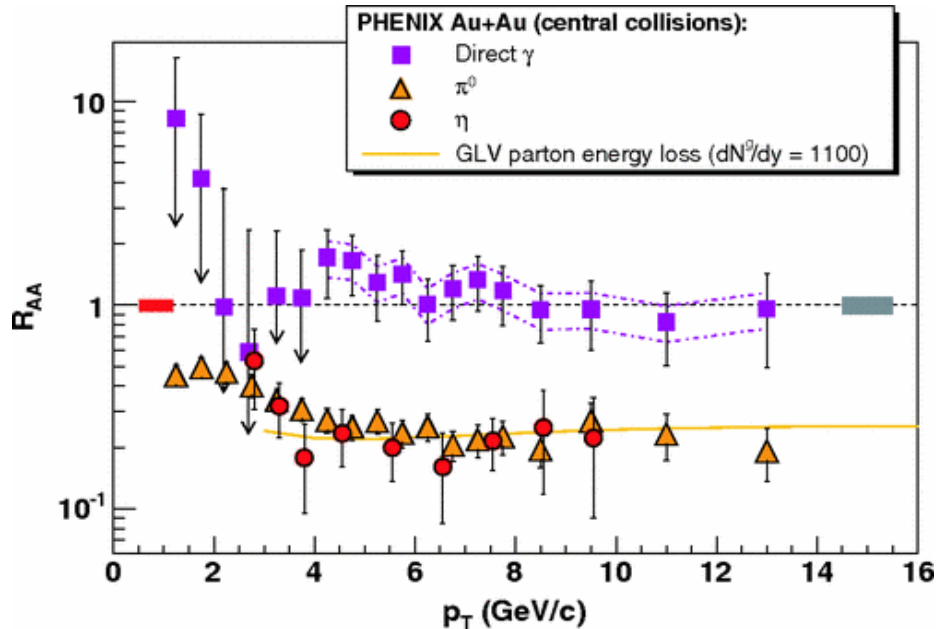


Figure 1.7:  $R_{AA}$  vs.  $p_T$  in central Au+Au collisions. We can see the suppressions of the yields of  $\pi^0$  (orange),  $\eta$  (red) particles, and not in the case of direct photons  $\gamma$  (purple) [7].

**Two Particle Correlation Study:** This thesis primarily uses this method to study jet quenching, which will be discussed in detail in the analysis chapter 5. The two-particle correlation function is employed to examine the correlations between pairs of particles generated in the same event of collisions. When a jet traverses the medium, the high-energy quarks and gluons within the jet can lose energy through interactions with the medium. This energy loss can impact the correlations between the particles produced in the back-to-back jets during the collision, resulting in either suppression or enhancement of the correlations compared to proton-proton collisions. To investigate jet quenching using the two-particle correlation function, researchers typically compare the correlation function for particle pairs in heavy-ion collisions to that in proton-proton collisions. By comparing these two quantities, researchers can determine whether the correlations are suppressed (indicating jet quenching) or enhanced (indicating jet enhancement) in heavy-ion collisions. Moreover, the

two-particle correlation function allows for the examination of how jet quenching depends on variables like jet energy and collision centrality. Extracting the two-particle correlation function from the data involves techniques such as the two-particle cumulant method or the two-particle correlation function method. These techniques involve constructing the correlation function from the two-particle distribution and fitting it to a suitable function to extract information about the strength and shape of the correlations. The resulting correlation function can then be used to investigate the properties of the medium and the interactions between the jets and the medium. Since the jets are back-to-back, it is expected that the two-particle distribution exhibits peaks around the azimuthal difference of  $\Delta\phi = 0$  and  $\Delta\phi = \pi$ . In Figure 1.8, the azimuthal distribution of two particles is depicted, with the peak near 0 showing no suppression, while the peak near  $\pi$  is suppressed due to the interaction of the jets away from the QGP medium produced in heavy-ion collisions compared to the baseline system. This phenomenon also characterizes the behavior of jet quenching and the formation of dense QGP matter.

### 1.6.1.3 Quarkonia Suppression

Quarkonia refer to bound states that consist of a heavy quark and a heavy antiquark, such as charm-anticharm or bottom-antibottom. These particular states can be generated through high-energy collisions of particles, and studying their characteristics can offer valuable insights into the strong force and the nature of the QGP medium. When a quarkonium state is formed within the QGP, the heavy quark and heavy antiquark can interact with the quarks and gluons present in the medium. As a result, they become screened by the color charges of the medium and experience a loss of energy. This energy loss can lead to the dissociation of the quarkonium state, causing the quark and antiquark to separate and exist as free entities rather than as a bound state. The extent to which quarkonia are suppressed in the QGP is contingent upon various factors, including the properties of the quarkonium

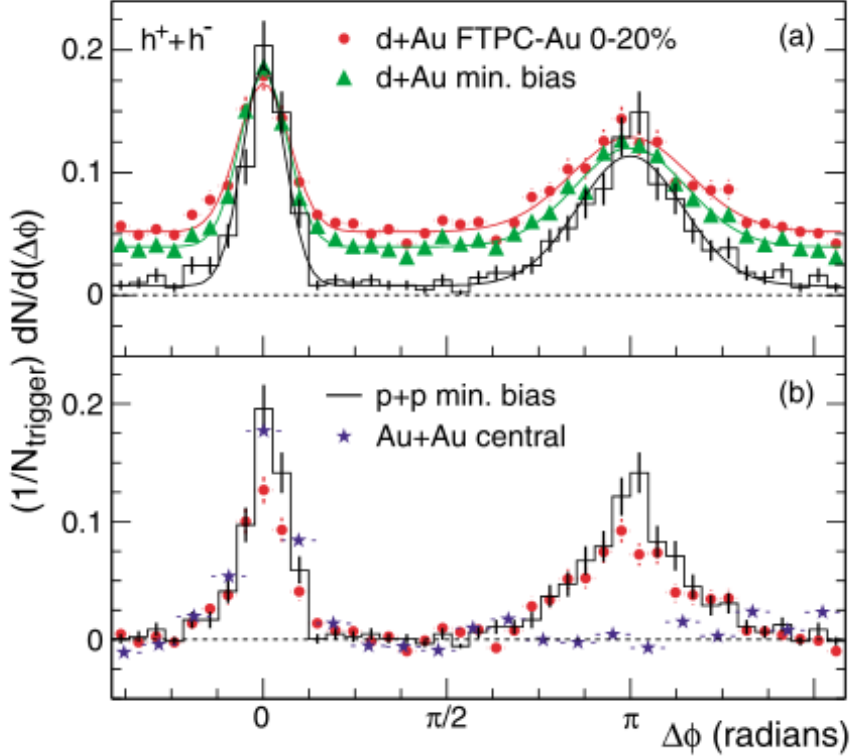


Figure 1.8: Two-particle correlation study shows the suppression in Au+Au collisions seen by STAR experiment [8].

state and the QGP itself (e.g., quarkonium mass, temperature and density of the QGP, and transport properties of the medium). Consequently, the suppression of quarkonia states is also regarded as an indication of the formation of the QGP.

#### 1.6.1.4 Strangeness Enhancement

The restoration of chiral symmetry leads to an increase in the production of strange quarks, resulting in a higher abundance of final state hadrons containing strange quarks. In a quark-gluon plasma (QGP), the presence of high temperatures and densities enhances the production of strange particles, which are particles that contain strange quarks. These extreme conditions increase the likelihood of producing strange quarks and antiquarks

through strong interactions. Moreover, the high energy density of the QGP promotes the production of gluons, which can then fragment into strange quarks and antiquarks as a result of the process  $gg \rightarrow s\bar{s}$ . The enhanced production of strange quarks and antiquarks leads to an increased production of strange particles such as kaons and hyperons, which also contain strange quarks. This enhancement in strange particle production within the QGP offers valuable insights into the properties of the QGP. Figure 1.9 illustrates how the production of strange particles increases with the number of participating nucleons during collisions, indicating the formation of a dense medium QGP in cases where a larger number of nucleons participate in the collisions.

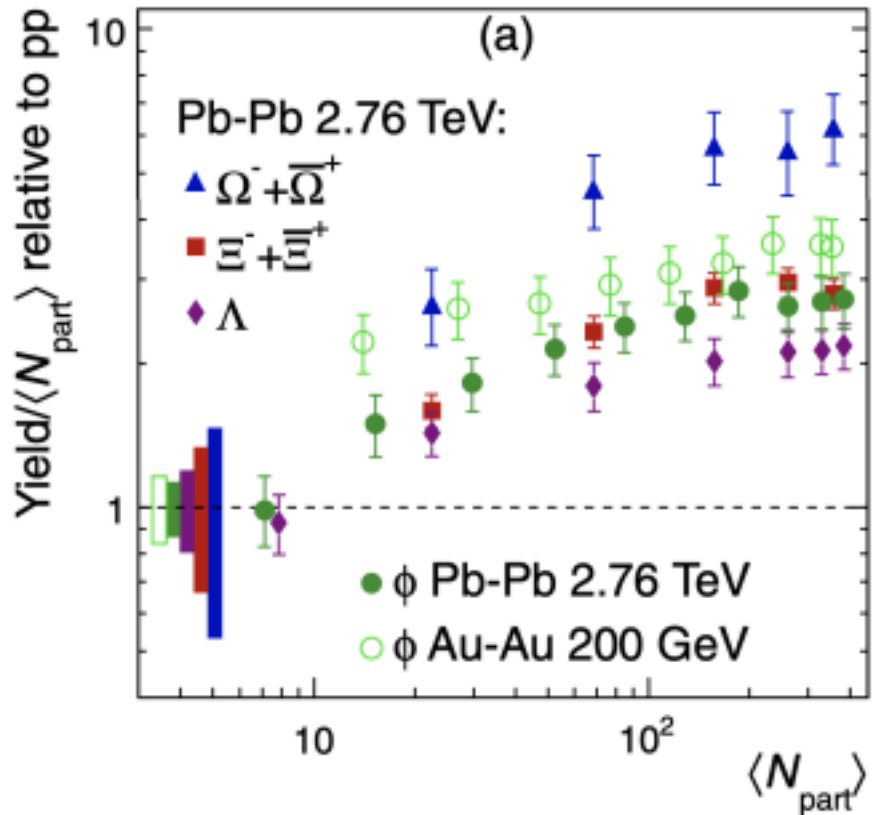


Figure 1.9: Enhancement of the production of strange baryons as a function of mean number of participating nucleons in Pb+Pb collisions seen by ALICE collaboration [9].

## 1.7 Motivation of the Research

There are two motivations for this thesis. The first part involves developing a calibration technique for the sPHENIX electromagnetic calorimeter using  $\pi^0$  particles, we call this method “ $\pi^0$  calibration method”. The  $\pi^0$  particles are reconstructed using the two photons which are the actual objects EMCal records during data-taking, with many photon-pair invariant mass values histogrammed and mathematically fitted. It is an iterative unfolding method where the effects of multiple towers are unfolded into a single tower when we consider the  $\pi^0$  particle for a tower. Many challenging technical advances were needed for this method to work in sPHENIX. For example, the sPHENIX EMCal has 24,576 towers/channels from which it can record the data, and a fit is performed for each of these towers multiple times, on order of about 10-20 times. Thus it is a challenging task to get enough statistics to fill for all the EMCal towers, as well as reliably apply an automated algorithm to perform the fitting without human intervention for hundreds of thousands of fits. Therefore, we were motivated to develop a robust method that could address several difficulties including these, that the sPHENIX EMCal poses during data collection.

The motivation for the other half of the thesis is primarily given later in Chapter 5 , Section 5.1 but can be summarized as follows: In order to create QGP matter in a collider system, it is necessary to have an appropriate environment with a sufficiently high energy density of at least  $1.0 \text{ GeV/fm}^3$  and/or a high temperature of approximately 170 MeV. Such an environment can be easily achieved in A+A collisions between two heavy ions, such as Au+Au in RHIC or Pb+Pb in LHC, but only in fairly central events. It was previously believed that QGP matter could only be formed in these large collision systems in very central events. However, results from some experiments indicate that QGP might also be formed in smaller collision systems [25], although smaller in size. This also brings up the question of what, if any, centrality even in the A+A collisions at peripheral centralities, defines the limit of when QGP can form in A+A collisions.

Thus the search for evidence of QGP formation in these small systems or peripheral A+A centralities, is an active area of research [35]. While some signatures of QGP formation, such as particle flow, have been observed, others, such as the jet quenching phenomenon, have not yet been observed. Several studies have been conducted in the direction of small systems, including some from our own Ohio group, a Ph.D. thesis of Bing Xia [26] that studies the d+Au collision, and another by Abinash Pun who studied  ${}^3\text{He}+\text{Au}$  collisions [1]. These studies unexpectedly found small hints (a small jet quenching suppression) of QGP, but remain hard to interpret without checking that even A+A collisions of similar sizes also have similar levels of suppression. This is especially true since there are other kinds of nuclear effects besides QGP which could cause these kinds of small levels of suppression. These small system results were also made using a new observable of jet quenching suppression called  $R_I$  which also needed checked to ensure it is as sensitive as more traditional jet suppression observables.

Therefore we were motivated to directly explore, in this dissertation, Au+Au collision systems with peripheral centralities, in particular those events in A+A which have a very similar number of participating nucleons as in the other small collision systems such as He+Au. For reasons explained in Section 5.1, we addressed this challenge by investigating Au+Au collisions using PHENIX data in two centrality ranges: 20-40% (representing central collisions where QGP formation and jet suppressions are anticipated so we can check that  $R_I$  works as expected) and 65-70% (representing more peripheral collisions).

## 2 THE EXPERIMENTAL METHODS

### 2.1 RHIC

The Relativistic Heavy Ion Collider (RHIC) is located at Brookhaven National Laboratory (BNL) in Upton, New York, USA. RHIC began data collection in 2000, with a per-nucleon energy of  $\sqrt{S_{NN}} = 200$  GeV for heavy ions. RHIC has the capability to collide various particle species, such as protons, copper, gold, and uranium nuclei, over a wide range of energies, from a few GeV to up to 510 GeV. RHIC also facilitates the collision of polarized proton beams to investigate the spin structure of particles. RHIC is made up of two counter-circulating beam lines with a circumference of about 3.8 km. The beam lines intersect at six different sites to allow for collision between ions. Along the beam line, there were four experimental halls: PHOBOS, BRAHMS, STAR, and PHENIX. Currently, there is a new experiment called sPHENIX in place of PHENIX. These different experiments were advantageous because the results obtained from one experiment can be complemented by the findings of other experiments. All experimental halls, with the exception of STAR and sPHENIX, have completed their data collection and have been decommissioned. Currently, scientists around the world are still analyzing the data obtained from the PHENIX experiment. The sPHENIX experiment has been taking data for two years necessitating further analysis of its experimental data. Further discussion of sPHENIX can be found in this chapter, particularly in Section 2.3. The image of the RHIC complex is shown in Figure 2.1.

### 2.2 PHENIX

The Pioneering High Energy Nuclear Interaction eXperiment (PHENIX) was an experiment conducted from 2000 to 2016 [12]. It was specifically designed to investigate high-energy heavy-ion collisions, with a primary focus on discovering Quark-Gluon Plasma (QGP) and studying its properties [28]. The PHENIX detector was capable of studying

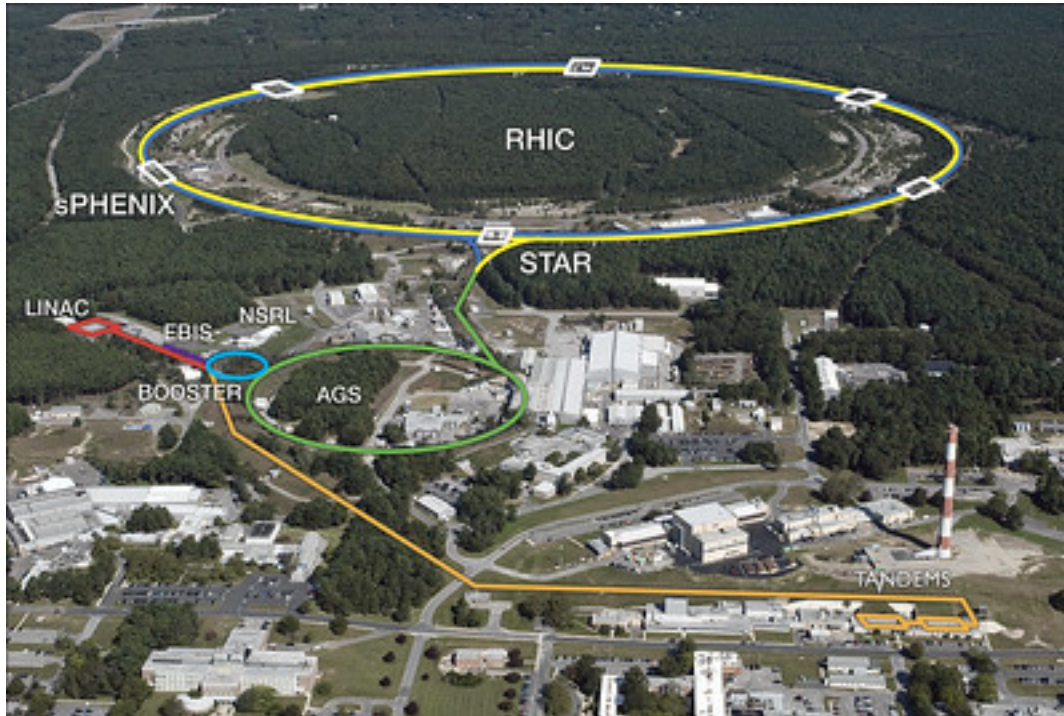


Figure 2.1: Relativistic Heavy Ion Collider (RHIC) complex at Brookhaven National Lab in Upton, NY, USA. [10].

collisions involving light-light ions ( $p - p$ ), light-heavy ions ( $p - Au$ ), and heavy-heavy ions ( $Au - Au$ ), to gain insight into nuclear matter under extreme conditions of high density and temperature. Additionally, PHENIX had the ability to measure the spin structure of nucleons through polarized proton collisions. It could accurately measure the energy and momentum of electrons, muons, photons, and hadrons. The detector consisted of numerous subsystems designed to detect and measure the particles produced in the collisions. The primary objective of PHENIX was to investigate the formation of QGP matter, which is believed to have occurred shortly after the birth of the universe. The ultimate goal was to improve our understanding of the strong interaction under such extreme conditions. Various probes, such as lepton and photon probes, were utilized to study this matter and examine the process of hadronization, which is ultimately observed by the detector subsystems.

Let us see one of the PHENIX detector setups for one of the RHIC beam run periods, that is, Run-14 corresponding to the Run year 2014 as shown in Figure 2.2. The total integrated luminosity during Run-14 for AuAu with  $\sqrt{s_{NN}} = 200 \text{ GeV}$  is  $7.5 \text{ nb}^{-1}$  and the number of events with a narrow vertex is 19 billion.

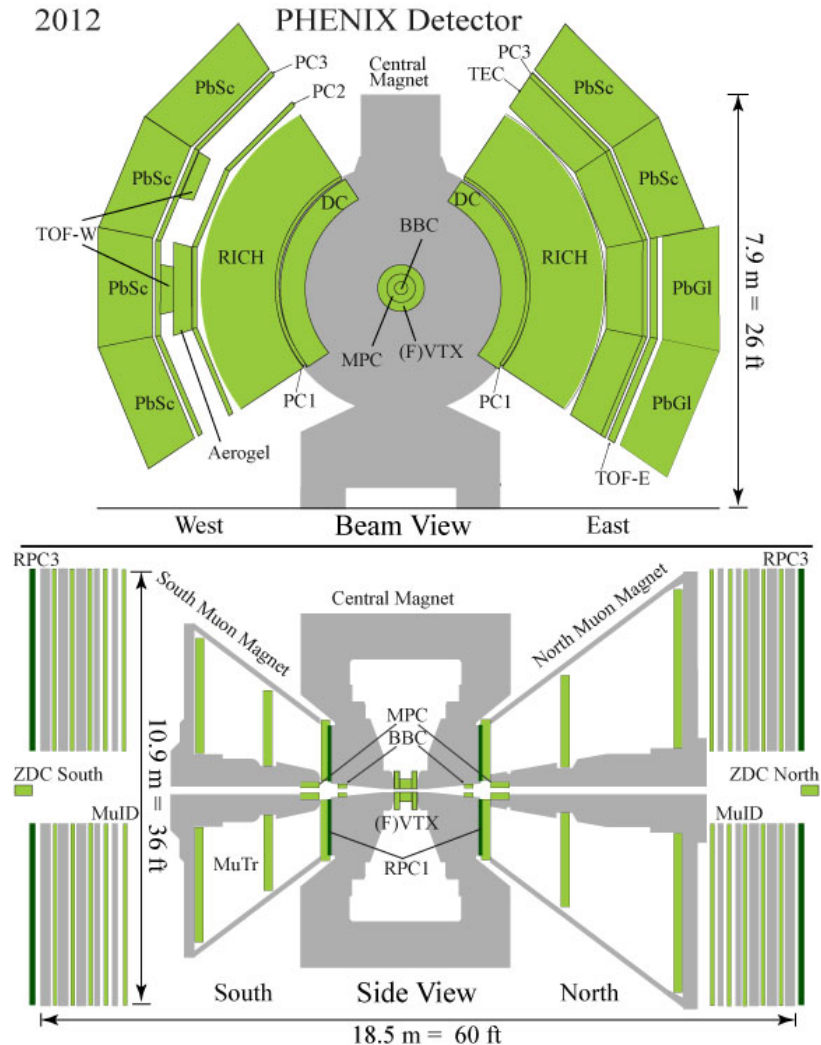


Figure 2.2: PHENIX setup during the Run 14 data-taking period. The top image shows the view along the beam line, whereas the bottom image shows from the side-view of the beam line [11].

PHENIX comprises multiple layers of subdetectors, each with specific tasks. The innermost layers are referred to as tracking detectors, which are responsible for tracing the trajectory, determining momentum, and identifying charged particles. Following the tracking detectors is the Electromagnetic calorimetry system, which measures the energy and momentum of the particles. Additionally, global detectors positioned near the beam line serve to characterize collision events or more so collision geometries. They provide information on the start time of the collision, the collision vertex, and the collision centrality. These global detectors selectively save the collision events that are of interest, as not all events captured by PHENIX are scientifically significant. Storing and processing every single collision event is impractical due to storage limitations and processing time constraints. The collision start time is crucial for time-of-flight detectors to measure the time taken by particles to travel from the collision point to the respective detector. Figure 2.3 displays an image of the PHENIX detector. This thesis will delve into a detailed discussion of the relevant subdetectors.

A nice summary of the complete subdetectors can be found on the PHENIX internal website located at [36]. Only detectors/sub-detectors that are relevant for this thesis shall be discussed below. Colloquially, the PHENIX detector can be divided into following subdivisions, the details of which can also be found in [37]:

- Magnets
- Global Detectors - Event Characterization Detectors
- Central Arm Detectors - All the important parts of the detector
- Muon Arm Detectors

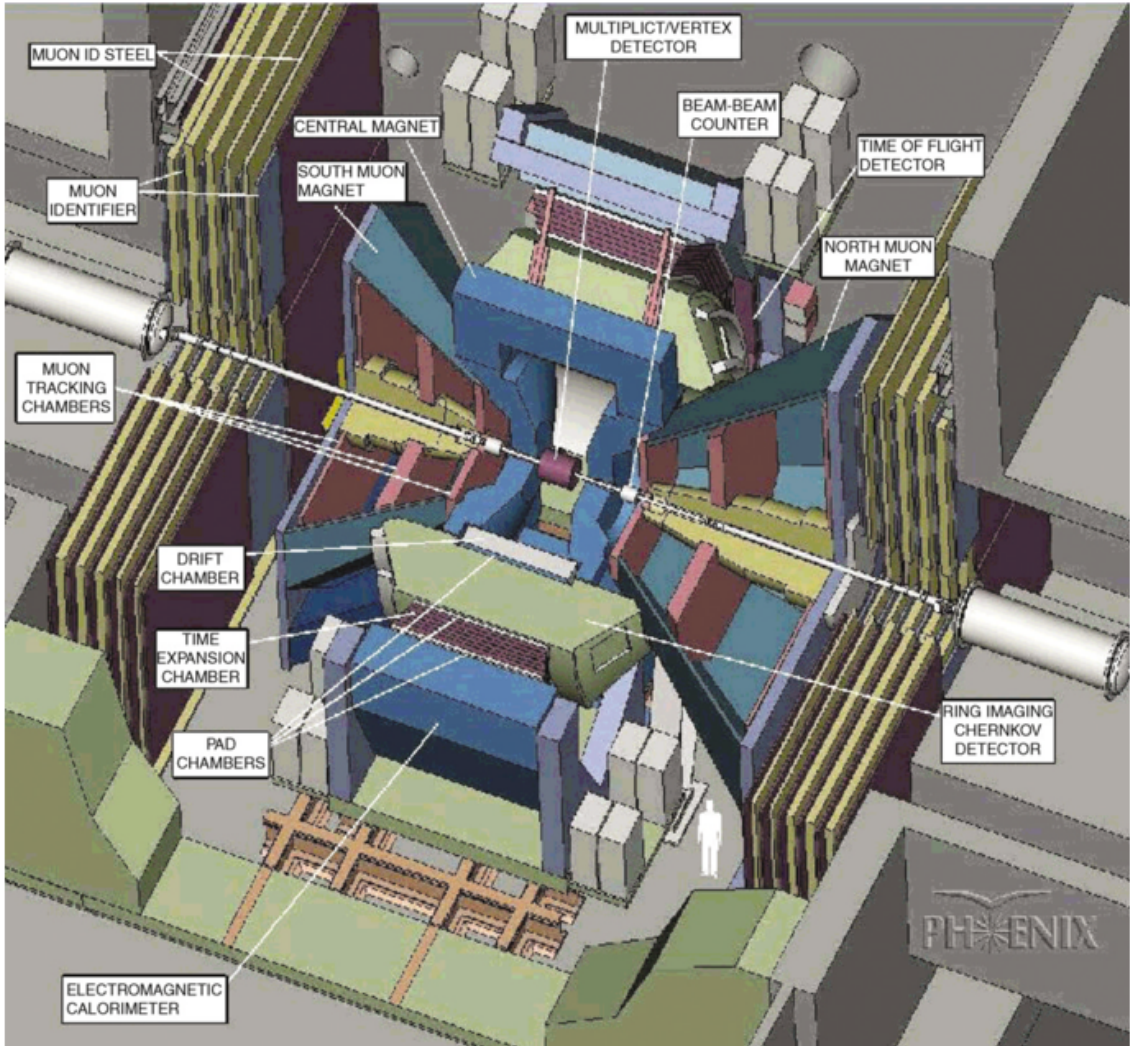


Figure 2.3: The PHENIX detector cutaway view showing majority of the sub-detectors [12].

### 2.2.1 *Magnets*

To analyze the momentum of charged particles, the detector uses magnets to bend them and direct them towards other detectors. The momentum is calculated using the Lorentz force law. In the PHENIX experiment, there are three magnet systems: central magnets for the central arm, forward magnet north (Muon Arm North) and forward magnet south (Muon Arm South). However, this thesis does not use any data from the forward arms, so we will

not discuss any sub-detectors related to them. Figure 2.4 shows the magnetic field lines in the central magnet. The central magnet is 9 meters tall and weighs approximately 500 tons, generates an axial field, and is powered by two pairs of concentric coils. These pairs can operate independently, together, or in opposite configurations. The acceptance range of the central magnet is  $|\eta| < 0.35$ .

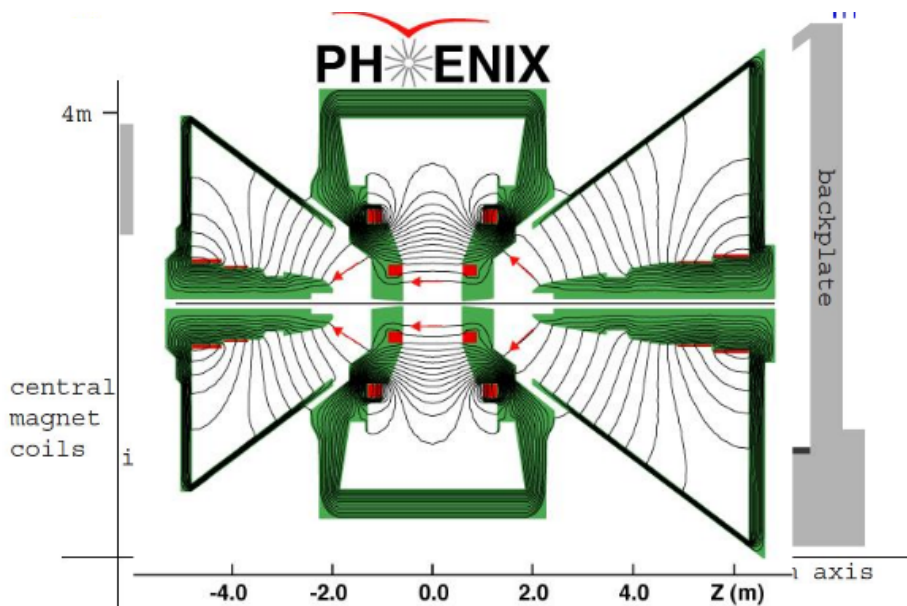


Figure 2.4: PHENIX magnetic systems showing its field lines. The beam runs along the horizontal line and collides at  $z = 0.0$  m [13].

### 2.2.2 Global Detectors

The arrangement of the global detectors in the PHENIX system can be seen in Figure 2.5. These detectors, highlighted in red blobs in Figure 2.5, are specifically designed for event characterization and triggering<sup>1</sup> purposes. The global detector components responsible for these tasks include the Beam-Beam Counters (BBCs), Zero-Degree Calorimeters

<sup>1</sup> Triggering, which will be discussed in more detail later, involves saving data from collision events when certain predetermined conditions for recording interesting events are met.

(ZDCs), and Reaction Plan Detector (RxNP). These detectors assist in determining the collision locations (vertex), initial collision time, interaction multiplicity (number of particles involved), centrality, and reaction plane.

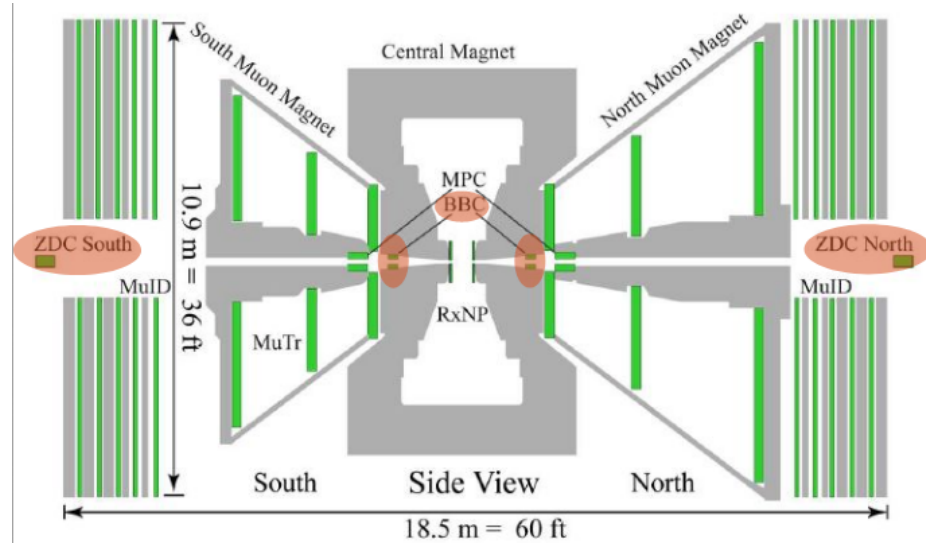


Figure 2.5: PHENIX global detectors BBCs and ZDCs colored in “orange blobs”.

### 2.2.2.1 BBC

The two identical BBCs are installed at a distance of approximately 144 cm from the PHENIX interaction region along the beam axis on both the North and the South sides. They cover the pseudo-rapidity range of  $3.0 < \eta < 3.9$  with full azimuthal coverage of  $2\pi$ . Each BBC counter consists of 64 BBC elements for the north and south arms, and each element consists of a quartz Cherenkov radiator and a meshed dynode PMT. The configuration of the BBC counters can be seen in Figure 2.6. The BBC can be used to calculate the initial time of the collisions as well as the vertex locations of the collisions. In order to measure the initial time of the collisions, we can use two timing parameters:  $T_N$ , which is the initial timing recorded by the north BBC arm, and  $T_S$ , which is the initial timing recorded by the

south BBC arm. The timing resolution is approximately  $52 \pm 4$  ps. Using these arrival times at the BBC, we can calculate the initial collision time  $T_0$  using Equation 2.1.

$$T_0 = \frac{T_S + T_N + 2L/c}{2} \quad (2.1)$$

where  $L = 144$  cm is the distance from BBC to the interaction region and  $c$  is the speed of light. Then, to calculate the z-vertex ( $z_0$ ), the location of the collision can be calculated as Equation 2.2

$$z_0 = \frac{T_S - T_N}{2} \times c \quad (2.2)$$

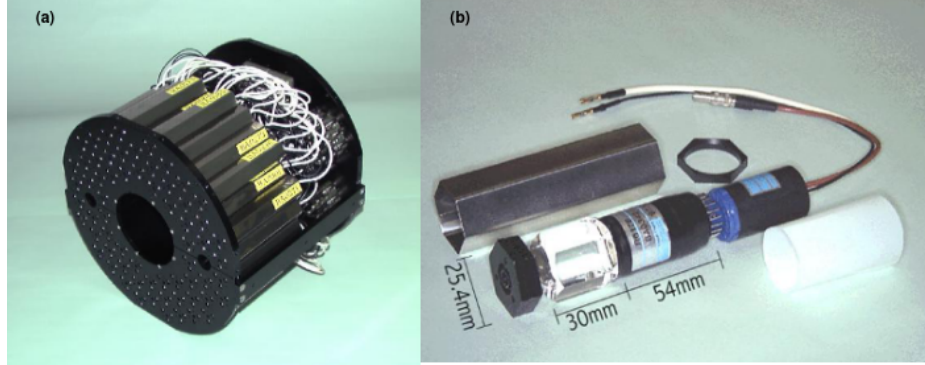


Figure 2.6: The PHENIX BBC counter [14]. (a) Each BBC array contains 64 BBC elements for both North and the South. (b) A single BBC element consists of quartz Cherenkov radiator and meshed dynode PMT.

### 2.2.2.2 ZDC

Like BBCs, ZDCs [38] also exist in pairs. They are positioned at a greater distance of approximately 18 m from the interaction region on both the north and south sides of the beam pipe. The ZDCs are situated behind the dipole magnets, which are responsible for steering the remaining beam away from the experimental detector area, and so the ZDC

only sees neutral neutron particles and not charged particles. As ZDCs function as hadronic calorimeters, they have the capability to detect the full energy neutrons which have the same per-nucleon energy as the beams, typically 100 GeV. Therefore, the ZDCs are specifically designed to capture the hadronic showers produced by the spectator neutrons. The ZDC configuration in the PHENIX can be seen in Figure 2.7, where the two red blocks shown in the figure are the ZDCs. ZDCs are used as complementary detectors for BBCs to measure the centrality of collisions.

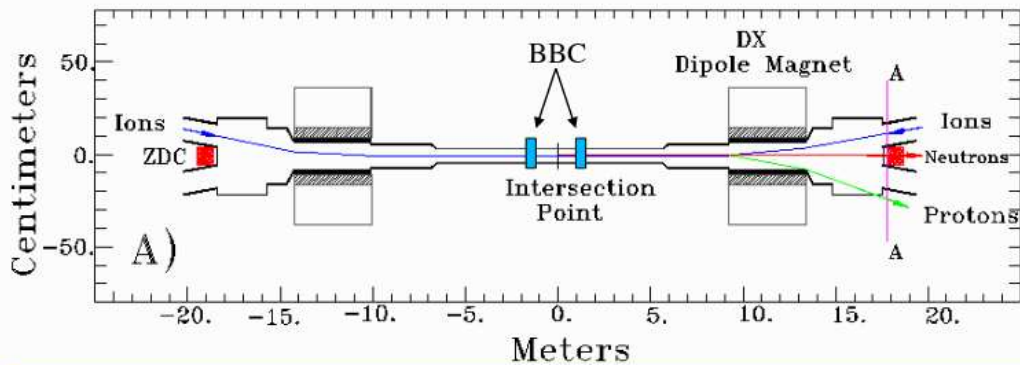


Figure 2.7: PHENIX ZDC shown in the red blocks along the line of beam [15].

### 2.2.3 Central Arm Detectors

In the context of this thesis, the central arm detectors encompass the main components of the detector that are of interest for our research objectives. These central arm detectors are positioned in the east-west directions at the central-rapidity region, perpendicular to the beam line. The two central arms are situated with their centers at zero rapidity and have a range of  $|\eta| \leq 0.35$ , providing a total azimuth coverage of  $\pi/2$  for each arm. The central arms primarily consist of the detector component systems and serve various purposes such as photon/electron reconstruction (tracking the charged particles), particle identification, and energy and momentum calculations. Specifically, the central arm of the PHENIX experiment

comprises Drift Chambers (DCs), Pad Chambers (PCs), Electromagnetic Calorimeter (EMCal), Ring Imaging Cherenkov Counters (RICH), and Time-of-Flight (TOF) detectors. The following section provides a brief overview of these components within the central arm of PHENIX.

### 2.2.3.1 Drift Chambers (DC)

The cylindrical-shaped drift chambers are located in the innermost part of the central arms of the east and west. They are positioned at a distance of 2 to 2.4 m from the beam line and extend 2 m along the beam pipe. For both the east and west arms, the azimuthal acceptance is  $90^\circ$  and with a pseudo-rapidity of  $\eta < 1.25$ . These chambers play a crucial role in measuring the path of charged particles and determining their momentum. They contain a gas mixture of Argon and Ethane with the 50/50 mix, which undergoes ionization when the charged particles pass through. DC also contains a large number of wires. The electric fields within the chambers drive the ionized electrons, allowing the trajectories of the charged particles to be determined. Moreover, inter-subsystem track matching helps to verify the presence of tracks and their detection by multiple subsystems within the PHENIX experiment. The wires within the DC are classified into U, V, and X groups, depending on their arrangement within the DC. The X-layer wire follows straight lines that are parallel to the beam, whereas the U and V layers form slight angles, as shown in Figure 2.8. These combinations of wires help reconstruct the track.

### 2.2.3.2 Pad Chambers (PC)

Pad Chambers (PCs) are used to provide track information and verify the results obtained from the drift chamber (DC). In the PHENIX experiment, there are a total of five pad chambers: two PC1s, one PC2 and two PC3s. PC1s are positioned between the DC and the RICH in the east and west arms. PC2 is present only in the west arm and is located behind the RICH. However, the PC3s are installed in both arms, positioned behind the

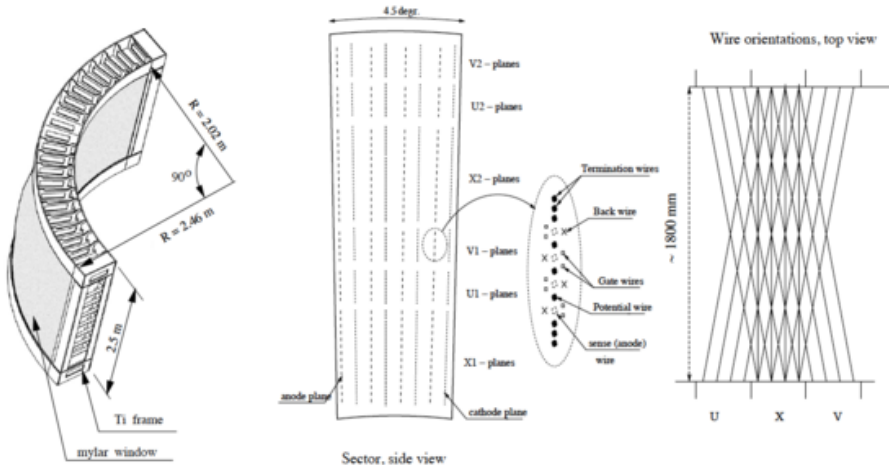


Figure 2.8: Left: PHENIX Drift Chamber mechanical drawing. Center: Sector of a drift chamber. Right: Top view of the drift chamber with wire orientations showing U, X, and V wires [16].

RICH and in front of the electromagnetic calorimeters. Figure 2.9 shows the location of the different pad chambers in the PHENIX experimental system. PC1s are used to measure the z coordinates of the track, which helps to cross-check the track construction with the drift chamber. The PC3s, on the other hand, are used to measure any charge particles at a higher radius just before they hit the electromagnetic calorimeter. This capability is useful in eliminating secondary charge-particle productions that are not relevant to the analyses. Please note that PC2 is not used in this thesis work.

### 2.2.3.3 Ring-Imaging Cherenkov (RICH)

In order to measure charged hadrons used in this correlation function analysis, it is necessary to exclude electrons from the charged track sample. The primary function of the RICH (Ring Imaging Cherenkov) is to discriminate the electrons produced in the collisions. The RICH is located in both central arms behind PC1. A cutaway view of the RICH detector is shown in Figure 2.10. When a charged particle travels through a medium at a speed

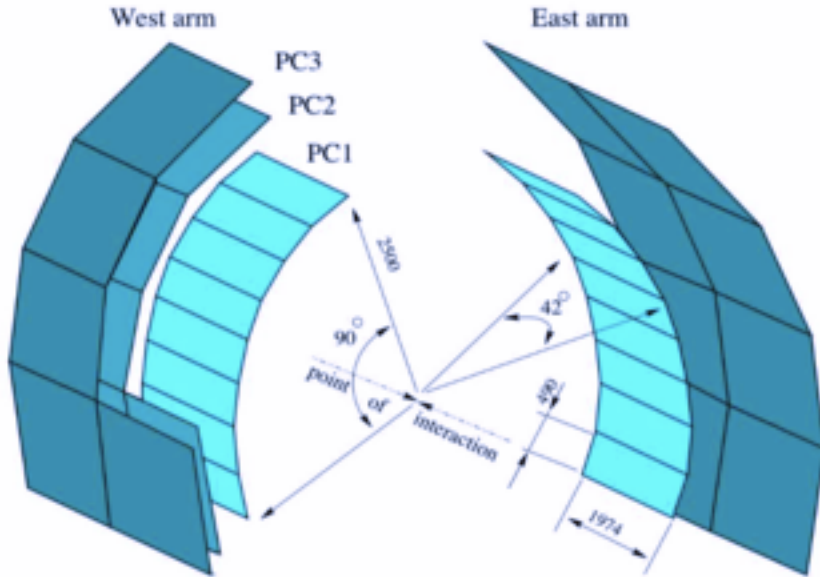


Figure 2.9: The cartoon depiction of the PHENIX pad chambers showing PC1, PC2, and PC3 [16].

greater than the speed of light in that medium, it emits electromagnetic radiation, known as Cherenkov radiation. In the RICH, the medium used is a CO<sub>2</sub> gas at a pressure of 1 atm, with a refractive index of 1.000410. The threshold for emitting Cherenkov radiation for pions and electrons is 4.65 GeV/c and 18 MeV/c, respectively. Since both particles of interest have momenta below 5 GeV/c, any measurements in the RICH above 5 GeV/c are disregarded when trying to separate electrons from the charge-hadron pools. Please note that charged hadrons with greater than 5 GeV/c energy are used if they are reconstructed by the other subdetectors. The emitted Cherenkov radiation is detected by the photomultiplier tubes (PMTs) installed in the RICH. By analyzing the shape of the hits or radii created by the radiation reaching the PMTs, it is possible to distinguish whether the Cherenkov radiation originated from electrons or other charged hadrons, such as pions. In this work, the RICH is employed to exclude electrons from the sample of charged tracks.

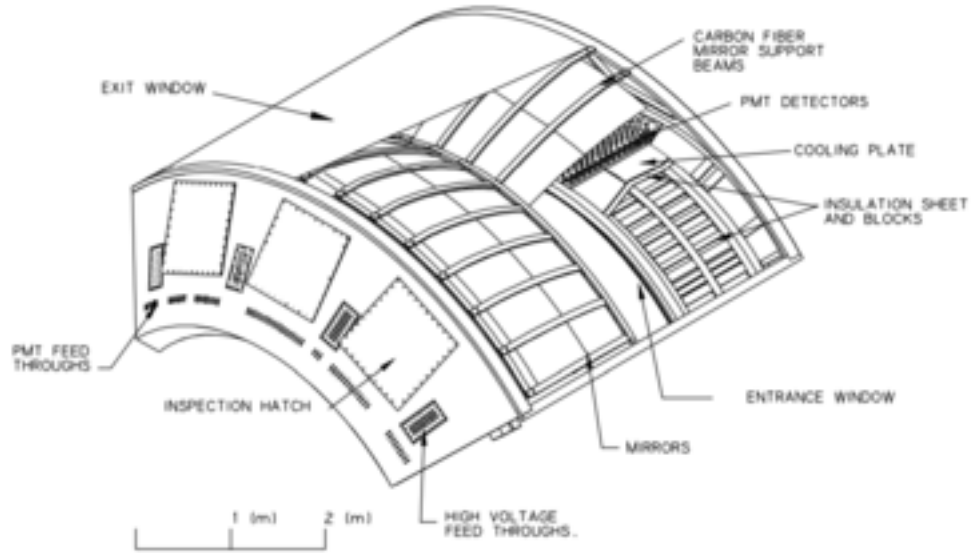


Figure 2.10: A cutaway view of one of the arms of the PHENIX RICH detector [17].

#### 2.2.3.4 Electromagnetic Calorimeter (EMCal)

The PHENIX ElectroMagnetic Calorimeter (EMCal) plays an important role in the collection of data needed in this thesis. The EMCal is capable of measuring the energy, position, and time of flight of electrons, positrons, and photons that interact with its materials. The other purpose of the EMCal is also to serve as an additional charged-tracking point and to contribute to particle identification (PID). Due to its fast response to energy depositions, EMCal can also be used to trigger high  $p_T$  photons and electrons. Its primary purpose is to measure the electromagnetic showers generated by photons and electrons when they collide with the EMCal; however, it is also capable of recording some of the hadron showers, too. The interaction between photons, electrons, and the EMCal materials is well understood and involves processes such as bremsstrahlung and pair production, which are part of the Quantum Electrodynamics (QED) mechanism. When high-energy electrons or positrons pass through the EMCal, they lose energy through Bremsstrahlung, resulting in the production

of photons. These photons can, in turn, undergo pair production, where they convert into charged particles such as ( $\gamma \rightarrow e^-e^+$ ). These two steps create a shower of particles until the last set of photons has enough energy to pair produce a particle. The particles created are detected as light or charge by signal-collecting materials called photomultiplier tubes (PMTs) embedded in the EMCAL. The resulting signals are then converted into pulse signals using the EMCAL electronics and recorded as data.

The PHENIX EMCAL has coverage that spans the entire acceptance of the central spectrometer, from  $70^\circ$  to  $110^\circ$  in the theta direction, on both the east and west sides. This coverage also includes  $90^\circ$  in azimuth. In PHENIX, two kinds of technologies are used in the EMCAL: the lead scintillator sampling calorimeter (PbSc) and the lead glass homogeneous Cherenkov calorimeter (PbGl). Of course, these two types of EMCAL have slightly different responses to incident particles, which helps complement each other better. Each type of calorimeter has different functionalities: PbSc offers better linearity and is optimized for high-time resolution, whereas PbGl provides better granularity and is optimized for high-energy resolution.

**Lead-Scintillator (PbSc) Sampling Calorimeter** The PbSc EMCAL module, as shown in Figure 2.11, is made up of Pb tiles alternated with a scintillator, which is why it is called a shashlik-type sampling calorimeter. It consists of a total of 15,552 “towers” [18]. The smallest units of calorimeters are called “towers”, which can be read independently via the electronics. PbSc has a tower size of  $5.5 \times 5.5 \text{ cm}^2$  laterally and 37.5 cm deep that contains 66 sampling cells. The module is made up of four towers (optically isolated). To collect light, the towers are optically connected at the end using wavelength-shifting fibers, which lead to the PMT’s. A total of 36 (6x6) modules are combined to create a supermodule and then 18 (3x6) supermodules are attached to form a sector. These EMCAL sectors were later installed on both spectrometer arms. The PbSc demonstrates superior linearity and is specifically

designed to achieve high timing resolution. PbSc is a type of sampling calorimeter. The energy resolution of the PbSc calorimeter can be determined as follows:

$$\frac{\sigma_E^{PbSc}}{E} = \frac{8.1\%}{\sqrt{E}} \bigoplus 2.1\% \quad (2.3)$$

The terms on the right-hand side of Equation 2.3 is a result of the natural processes that lead to a degradation in the resolutions of the EMCAL. The first term originates from the fluctuations associated with the development of the shower in the EMCAL, while the second term is a consequence of the intrinsic nonuniformities present in the EMCAL; added in quadrature to calculate overall PbSc EMCAL energy resolution. The timing calibration of PbSc EMCAL is better than 200 ps.

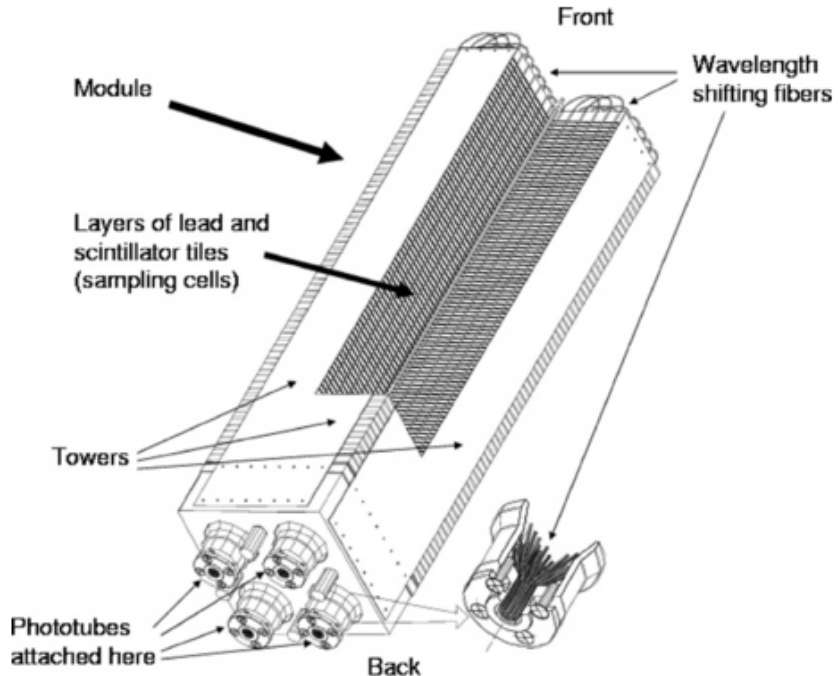


Figure 2.11: A cutaway view of module of PbSc showing the alternating Pb and scintillator tiles and other components [18].

**Lead-Glass (PbGl) Calorimeter** The PbGl EMCAL supermodule, shown in Figure 2.12, offers improved granularity and is specifically designed for high energy resolution. It is composed of a homogeneous medium consisting of lead, glass, and lead oxide. The PbGl towers have dimensions of  $4 \times 4 \text{ cm}^2$  on the lateral side and a depth of 40 cm. A supermodule is formed by combining 24 (6x4) PbGl modules, and a sector is created by grouping 192 supermodules. The energy resolution of the PbGl calorimeter is shown in Equation 2.4 and the timing resolution is better than 300 ps.

$$\frac{\sigma_E^{PbGl}}{E} = \frac{(5.9 \pm 0.1)\%}{\sqrt{E}} \bigoplus (0.8 \pm 0.1)\% \quad (2.4)$$

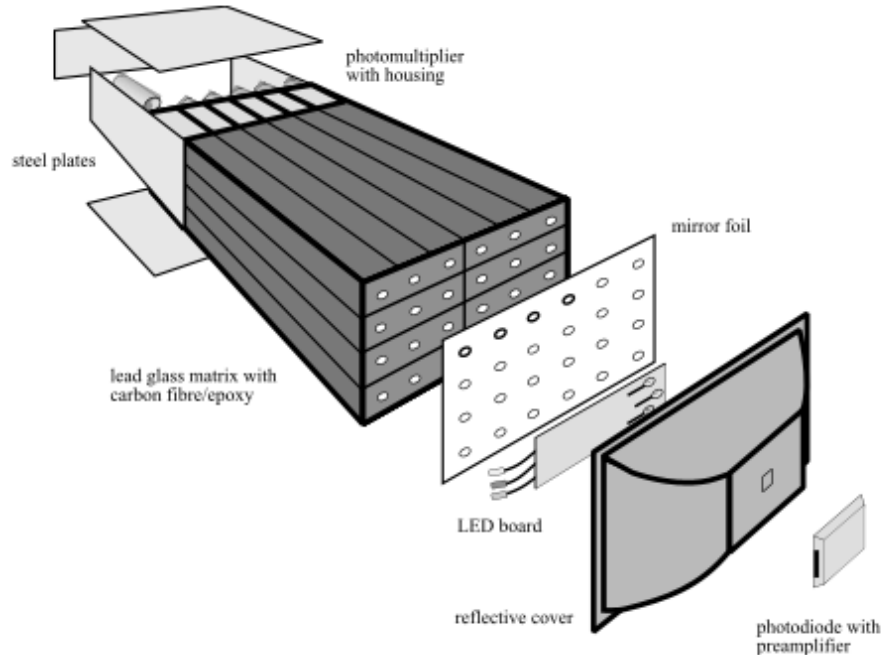


Figure 2.12: The exploded view of the PbGl supermodule [18].

In the east arm of PHENIX, there are 2 sectors of PbSc and 2 sectors of PbGl, while the west arm contains all four sectors of PbSc calorimeters.

#### **2.2.4 *Software and Data Acquisition and Trigger Systems (DAQ) in PHENIX***

The PHENIX software development mainly contains two frameworks [39]. They are:

- PISA: simulation framework based on GEANT3
- fun4all: This is the main reconstruction and analysis framework.

The Redhat Scientific Linux operating system is utilized on the BNL scientific computers. Users, including graduate students, can remotely access these computers using SSH to perform their analysis. The `tcsh` shell is employed on the BNL Scientific computers for the PHENIX experiment. The primary software used for analysis after the data are obtained from the “Train” jobs is ROOT but users can perform their analysis using the Python packages. Train jobs, also sometimes called “Taxi” jobs, are the way to submit users’ individually written analysis codes into the PHENIX computing framework. Then the Taxi runs the analysis code over the PHENIX dataset that is saved in the computing farms. Taxi jobs are submitted through the PHENIX internal webpages that are behind the firewall and cannot be accessed without having the proper verified account for each individual. When submitting the taxi, users have the opportunity to select various run-year PHENIX dataset that are of interest to the analyzers.

The Data Acquisition system (DAQ) of PHENIX is composed of granules and a partition system. These components enable the subdetectors to operate in coordination and collect data from each part. Figure 2.13 illustrates the schematic diagram depicting the flow of data within the PHENIX system and its collection process.

The module closest to the detector, known as the Front-End Module (FEM), is responsible for collecting input signals. These signals are stored in digital and analog memory units, which come from sources such as BBC, ZDC, EMCAL, and RICH. The Local Level 1 Trigger (LL1) performs a quick analysis using the data obtained from these sources. LL1 then sends the analyzed data to the Global Level 1 Trigger (GL1), which makes the final

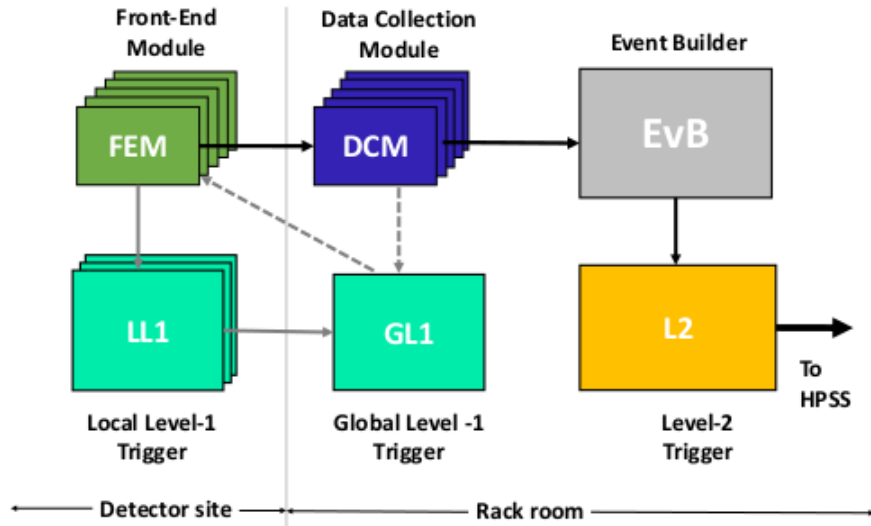


Figure 2.13: The flow of data in PHENIX system. The Local Level-1 Trigger and Global Level-1 Trigger helps to collect the events that are of higher importance and interesting for physics analysis.

decision regarding the analysis. If the GL1 trigger conditions are satisfied, the trigger is sent to the FEM to transmit the data to the Data Collection Module (DCM). The Event Builder (EvB) combines the data into data packets, which are then sent to BufferBox machine for recording. The data packet is eventually sent to the High Performance Storage System (HPSS) and stored on tapes.

### 2.2.5 Trigger Systems

In the context of a collider system, a significant amount of data is acquired during collisions. However, due to the enormous volume and time-consuming nature of processing and computing, it is not feasible to collect data from every collision. Moreover, not all collision events produce data that are relevant to physics analysis and for our purposes either. Hence, a trigger is used to selectively collect data from events that meet specific conditions.

The trigger system in the PHENIX system comprises two levels. The Level 1 triggers, located closer to the detector system, make decisions for each beam crossing using data from a few subsystems in parallel. Following the Level 1 triggers, PHENIX also had a Level 2 trigger system capability that could perform a more complicated rapid analysis of the data that have passed the Level 1 triggers to determine whether it should be stored or discarded. However, the level 2 trigger system was only used in the early years of PHENIX runs. It is worth noting that the requirements of the trigger system differ depending on the run, the species under investigation, and the physics that we are interested in. In the PHENIX data collection, two primary types of Level 1 triggers are utilized: the Minimum Bias Trigger and the EMCal/RICH Trigger.

#### **2.2.5.1 Definition of Minimum Bias (MB) Trigger**

The Minimum Bias (MB) trigger is responsible for capturing data or events that have minimal data collection conditions set up. It is designed to identify the occurrence of events based on minimal conditions. The MB trigger collects data with minimal interference from the detector systems. MB events are triggered using BBC global detectors located on the North and South sides of the collision region. The criteria of the PHENIX minimum bias events are such that there is at least one hit on PMT of both the North and South BBC. The z-vertex must be at least within  $\pm 30$  cm from the collision region. In addition, both the north and the south ZDCs should measure non-zero energies.

#### **2.2.5.2 EMCal/RICH Trigger (ERT)**

The EMCal/RICH Level-1 Trigger (ERT) is responsible for identifying events that contain electrons or high  $p_T$  photons. This trigger utilizes the EMCal and RICH detector subsystems. In the case of photon triggers, only the EMCal is utilized to calculate the combined energy of specific groups of EMCal towers. If the energy sum in these trigger

towers exceeds a predetermined threshold, the event is flagged for recording. However, for electron triggers, both the EMCal and the RICH detectors are employed.

### **2.2.6 *EMCal Clustering in PHENIX***

In the PHENIX experiment, a cluster refers to a group of adjacent towers in the calorimeter system that are struck by an EMC shower. The size of the cluster is determined by the *Moliere Radius* ( $R_M$ ). Approximately 90% of the shower energy is contained within a radius of 1  $R_M$ , indicating that most showers span two or more towers in the EMCal. Furthermore, a single tower can receive hits from multiple showers, leading to the issue of *energy-sharing*. Energy-sharing occurs when a single tower shares the hits and energies of multiple showers. One of the challenges in the Au+Au environment, where there are a lot of particles, is to effectively distinguish between each cluster that strikes the calorimeter. The PHENIX clustering algorithm is briefly summarized as follows:

1. Identify the group of neighboring towers whose energy exceeds a certain threshold, referred to as a cluster of towers.
2. Within the cluster, determine the tower with the highest energy, known as the local maximum of the cluster. The local maximum must have an energy value above a specific peak energy threshold and be surrounded by a 3x3 region of towers with significantly higher energies. It is possible for a cluster to have multiple local maxima.
3. Perform a fitting process around the local maximum to determine the peak using a shower shape fitting function. If a tower has multiple peaks due to being part of multiple clusters, the energy is divided among each peak using a shower profile fit function.
4. Define the “core” cluster as a smaller cluster of towers around the peak that contains almost all of the cluster’s energy.

### 2.2.7 *Centrality Determination in PHENIX*

The objective of centrality calculations is to classify collision events according to their initial geometry and the number of nucleons involved in the collisions. Ideally, to characterize collisions, we would like to know the impact parameter, which is the distance between the centers of the two colliding nuclei. However, currently it is impossible to measure the impact parameter in a high-energy collision environment, where the distance would be on the order of femtometers. Therefore, a proxy measurement called centrality is used instead. The centrality value that we use conventionally is inversely related to the amount of overlap in the collisions. The most central collisions exhibit nearly 100% overlap between colliding bodies, resulting in the production of a large number of final-state particles, but we call these central events with centrality 0% and larger. In contrast, peripheral collisions involve less overlap and produce fewer final-state particles, and we call these peripheral events with centrally 100% and less.

The PHENIX experiment utilizes two detector systems, BBC and ZDC, to assess the centrality of collisions. In highly central collisions with significant overlap, a substantial number of charged particles are generated in the mid-rapidity region, as observed by the BBC detector. In contrast, the ZDC detector registers a smaller number of spectator neutrons in these collisions. However, in peripheral collisions, the BBC detector detects fewer charged particles in the mid-rapidity region, whereas the ZDC detector observes a larger number of spectator neutrons. This information is used to quantify the centrality class using two methods, i.e. the clock method and the BBC only method. The clock method utilizes BBC and ZDC data to determine centrality, whereas the BBC-only method relies solely on information from the BBC detector. Figure 2.14 shows both the clock method and the BBC-only method. In the clock method, each red and blue bin is of type 5%, where the most central collisions are in the right-hand bin. In BBC only method, the final-state charge distribution in the BBC is divided into percentiles where each percentile has the same

number of events. Again, red and blue in the BBC-only method represent the 5% intervals with the most central collision on the right-hand side bin.

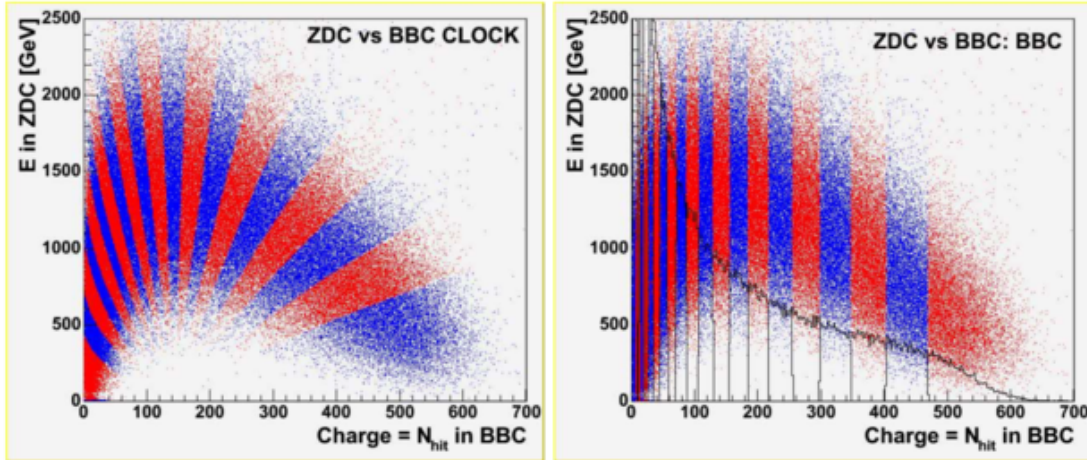


Figure 2.14: Left: Clock method. Right: BBC only method. They helps to determine the centrality in the PHENIX [19].

Once the centrality of an event is determined using either of the above methods, it can be used in the Glauber Monte Carlo model to calculate other experimental parameters such as the number of participating nucleons ( $N_{part}$ ), the number of colliding nucleons ( $N_{coll}$ ) and the impact parameter ( $b$ ) of a collision, which can be seen in Figure 2.15. The Glauber Monte Carlo model is used to map the experimental measurements in order to estimate the geometrical parameters of the collisions.

### 2.3 sPHENIX

sPHENIX [29] is the first RHIC experiment in more than two decades, succeeding the PHENIX experiment. The primary objective of sPHENIX is to investigate quark-gluon plasma (QGP) and other phenomena related to cold Quantum Chromodynamics (QCD) with enhanced capabilities, such as coverage over full azimuth and pseudorapidity  $|\eta| < 1$ ,

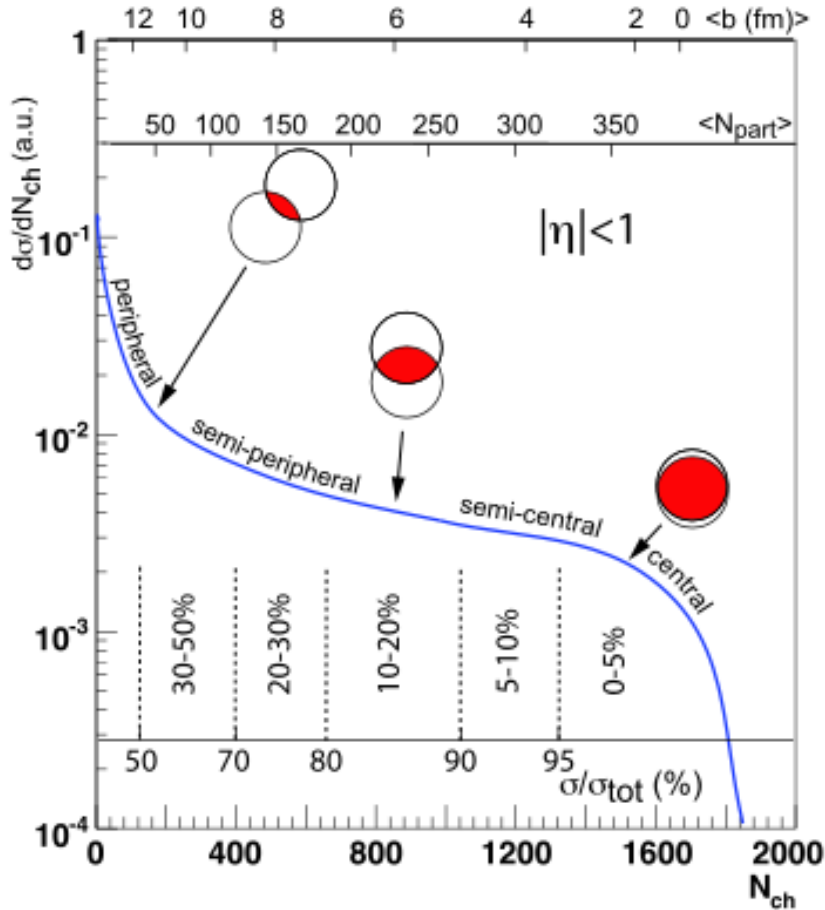


Figure 2.15: Correlation of the final state observables  $N_{ch}$  and the observables calculated by the Glauber Monte Carlo model [20].

including a wider kinematic range, faster data acquisition / trigger system, and the inclusion of both hadronic and electromagnetic calorimeters (EMCal). Detailed specifications for the sPHENIX detector can be found in the Technical Design Report [22]. The general structures showing the cutaway view with most of the sub-detectors labeled in the sPHENIX detector are shown in Figure 2.16. In the first part of this thesis, the focus is on development of a new calibration method for the calibration of the sPHENIX electromagnetic calorimeter. It is important to note that the sPHENIX upgrade is a collaborative effort that involved

about 80 universities and laboratories from 14 countries and nearly 400 collaborators. Detailed calibration processes are described in Chapter 3. This section provides only brief descriptions of the sPHENIX electromagnetic calorimeter.

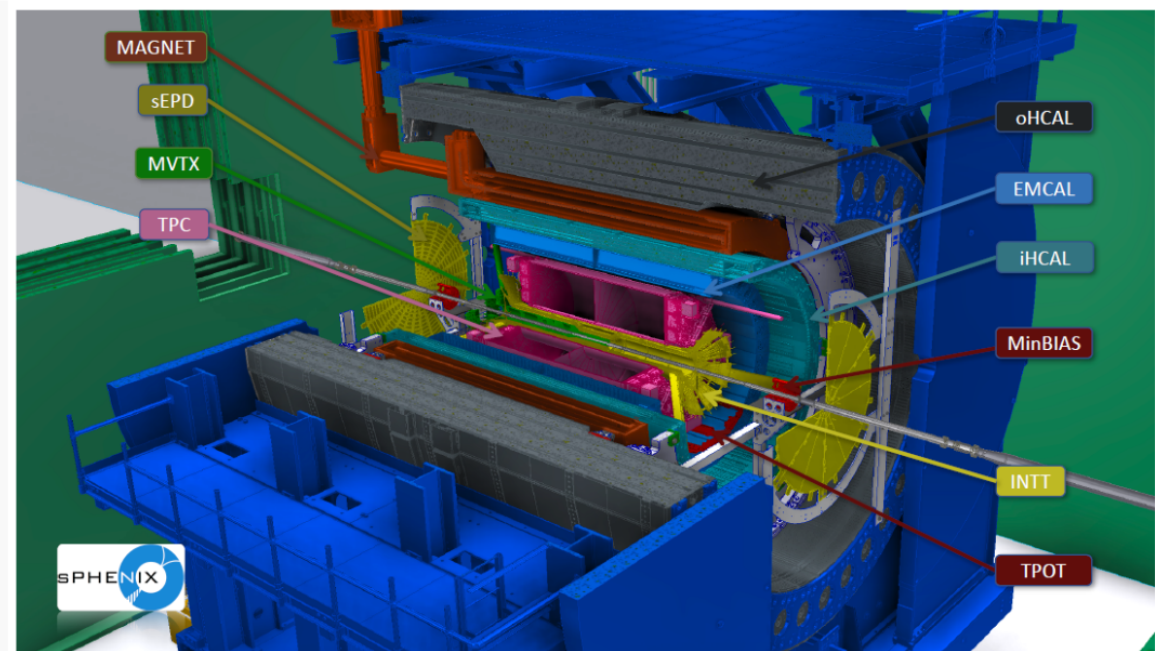


Figure 2.16: The cut-a-way engineering plot of sPHENIX Detector [21]. The height of the detector from the ground to the top of the rack is about 15-20 m. The beam-pipe is shown in the silver color that runs through the center of the detector which is then surrounded by several layers of detector subsystems.

### 2.3.1 *sPHENIX Electromagnetic Calorimeter (EMCal)*

The sPHENIX electromagnetic calorimeter plays a crucial role in the success of the sPHENIX experiments in general. Its design requirements are heavily based on the physics goals of the sPHENIX experiment and also on the budget and resources available from the PHENIX experiments. To read about the goals and prediction of the sPHENIX experiment

as a whole, see [40]. sPHENIX EMCal measures the energy and momentum of photons, electrons, and positrons with better accuracy than its predecessor, PHENIX. The EMCal along with the hadronic calorimeters plays a crucial role in the jet reconstructions, which are considered to be one of the best probes for studying the partonic interactions with the QGP. sPHENIX EMCal together with the hadronic calorimeter has a total depth of about 4.9 hadronic interactions. The dimensions of the sPHENIX EMCal must be compact enough to fit inside its magnet which was obtained from a previous experiment, (BABAR), and accommodate the tracking system within it. The BABAR now sPHENIX magnet is a cylindrical shell with an inner radius of 1.4 m, and the EMCal also reflects this geometry being a cylindrical shell with an inner radius of about 1.0 m. The actual installation of the sPHENIX EMCal is shown in the Figure 2.17. The sPHENIX EMCal offers an improved coverage of  $\pm 1.1$  in  $\eta$  at a forward angle and a full azimuthal coverage of  $2\pi$ . The EMCal is designed to be projective in both  $\eta$  and  $\phi$  directions as can be seen in Figure 2.18 where the event vertex at the center of the detector would be located 1m below the left end shown and thus particles will traverse up through the bottom of the sector shown in the directions of the “block/tower” segments shown. The projective design of EMCal helps to improve uniformity of response. A small “tilt” angle in both phi and pseudorapidity is added to break the perfect projectivity, however, in order mitigate the channeling of the energy through the small gaps along the EMCal.

Within this geometric acceptance, the EMCal is designed to measure electromagnetic showers in the energy range of approximately 0-70 GeV in order to measure direct photon-jet pair with photon energies up to this range. The expected resolution of the sPHENIX calorimeter, determined by its design and materials making up a block, and verified by prototype testing with testbeams, [22], [41] is approximately given by the expression  $\sigma_E/E = 13.5\%/\sqrt{E} \oplus 4\%$ .



Figure 2.17: The cylindrical shaped sPHENIX EMCal housed inside of the Inner Hadronic Calorimeter (IHCal) is being installed. The lower inset image shows the actual sPHENIX EMCal sectors being laid around the barrel shaped IHCal. The EMCal sector is shown in Figure 2.18.

The block, which is the smallest singly constructed unit of sPHENIX EMCal, is made up of 2668 scintillating fibers to transport the signals lights enclosed in a mixture of tungsten powder and epoxy as an absorber. At the end of the EMCal, silicon photomultipliers (SiPMs) are employed as readout converting the light generated in the fibers from the shower particles into an voltage pulse. Analog-to-digital converter (ADC) will digitize the received pulse from SiPMs, enabling them to be eventually converted into photon and electron energies. Before finalizing the current design, various prototypes were tested using simulations and test beam experiments [42].

The EMCal of sPHENIX consists of a total of 24,576 towers, organized into 6,144 blocks. Each block is therefore divided by attaching the SiPM's in four separately and symmetrically divided regions of the fibers, which then define 2x2 tower “sections” in each block. The segmentation of the EMCal towers is  $0.024 \times 0.024$  radians in terms of  $\Delta\eta \times \Delta\phi$ . The EMCal sector, which is a larger piece connected to the sPHENIX supporting systems, is made up of a combination of 96 blocks. The sPHENIX EMCal is divided into 64 sectors, with 32 azimuthal sectors and 2 longitudinal sectors. These sectors are supported by the inner hadronic calorimeter. Figure 2.18 shows the arrangement of the blocks within an EMCal sector, as well as other electronic components.



Figure 2.18: The sPHENIX EMCal sector layout showing blocks and electronics components [22].

### **3 sPHENIX Pi0 TOWER-BY-TOWER CALIBRATION TECHNIQUE: DEVELOPMENT AND METHOD**

The first part of this dissertation describes my development of a new calibration technique to apply to the sPHENIX Electromagnetic Calorimeter (EMCal) using the  $\pi^0$  particles. The core of the method, a technique for the iterative unfolding of the multi-tower, 2-photon calibration, into single tower calibration constants, was developed previously on the PHENIX experiment by several individuals including one of us, Justin Frantz, thesis advisor for this dissertation. However, this technique itself was never formally published by PHENIX. In this dissertation the technique was adapted and expanded for sPHENIX including a full new implementation. This dissertation work includes several improvements to the overall methodology and novel expansions of the technique, for example unique algorithms for automated checking fit quality and refitting in order to make it robust for the larger tower-count (24576) in sPHENIX, and the eta-ring by eta-ring method. At the time of writing this thesis, June 2024, sPHENIX has applied our implementations to both Run 2023 and 2024 data successfully, some of which is presented here.

#### **3.1 Calibration of sPHENIX Electromagnetic Calorimeter**

In simple terms, calibrating a device involves making sure that the device accurately shows the correct value of what it is trying to measure. In our study, we are focusing on calibrating the sPHENIX detector Electromagnetic Calorimeter (EMCal). The EMCal responsible for measuring the energy of photons, electrons, and positrons in the expected energy range of around 0 to 70 GeV, that are produced during particle collisions near the interaction region (IR) of sPHENIX. Important characteristics of the sPHENIX EMcal such as its resolution are given in section 2.3.1.

It is important to fix the detector's response to these and others because the initial readings of the detector do not give an accurate idea of the actual energy of the particles that hit it. When particles strike the detectors, the detectors are only able to capture the brief voltage fluctuations from their electronics that are simply a bunch of digits, which are then needed to be translated into meaningful physical variables. The main purpose of calibration is to translate the electronic digits into some useful variables. These fluctuations are recorded as analog-to-digital converter (ADC) values based on analog voltage pulses from the silicon photomultipliers (SiPMs) for each towers/channels, which are related to the energy of the particles that impact them. Through the calibration process, these ADC values are converted into the actual energy of the particles using the following linear equation 3.1.

$$E_{tower} = C_{gain,tower} \times N_{ADC,tower} \quad (3.1)$$

Here,  $C_{gain}$  is often referred to as the “gain” in many experimental nuclear and particle physics.  $N_{ADC,tower}$  referred to as the voltage or amplitude recorded by the SiPMs for the particular tower of interest. In equation 3.1, we can see that a calibration correction is required to correct the gain of the tower if we wanted to read the true energy of the incident particles  $E_{tower}$ .

The calibration of EMCal involves multiple steps and different methods that complement each other, one of which is a preliminary calibration that aims to equalize the relative values of all channels in the EMCal. This is called *relative* calibration. Once the EMCal undergoes a relative calibration, the very final calibration steps carried out are referred to as *absolute* calibrations.

The specific method of calibration we developed is called “Pi0 Tower-by-Tower” method, pi0 method hereafter. It can be considered a partially absolute method but only to within a certain precision in practice as discussed below at the end of section 4.3, we mostly use it as a relative calibration method. This pi0 method involves collecting energies from the

hits of  $\pi^0$  particles on the EMCal and comparing the resulting output with the true invariant mass energy of  $\pi^0$  of approximately 0.135 GeV by PDG [43]. Eventually we define and apply corrections that can force the detector to reproduce the pi0 mass at this PDG value, so at this stage the calibration can be considered nearly absolute. But as discussed below in section 4.3 because of many practical limitations such as detector resolution, non-linearity, and other effects, a further single constant generally needs applied to more accurately fix the absolute calibration. Thus for the final calibration, our method actually serves more like a relative calibration method, and even sometimes we make modifications that reflect this as discussed in section 4.3.

The process is carried out by initially reconstructing the  $\pi^0$  from the two photons using Equation 3.2.

$$m_{\gamma_1\gamma_2} = \sqrt{2E_{\gamma_1}E_{\gamma_2}(1 - \cos(\phi_{\gamma_1\gamma_2}))} \quad (3.2)$$

where  $\gamma_1$  and  $\gamma_2$  are the two (decay) photons of the particles  $\pi^0$ ,  $E_{\gamma_1}$  and  $E_{\gamma_2}$  are the energies of the two photons, and  $\phi_{\gamma_1\gamma_2}$  is the opening angle between the two photons.

When two nuclei collide at high energies (specifically, 200 GeV per pair of nuclei) in a particle collider, a large number of particles are produced. These particles are scattered in all directions and eventually detected by subsystems placed around the collision region. One of the most common particles created in these collisions is the neutral pion ( $\pi^0$ ), which is the lightest meson. Therefore, it is logical to use these pions to calibrate the EMCal detector, as many of them are produced. There are several reasons to choose  $\pi^0$ : first, a large number of pions are produced, resulting in greater statistical significance; second, the true energy value of  $\pi^0$  (0.135 GeV) is known from the Particle Data Group (PDG), making it easy to correct detector settings. When pions are created, they rapidly decay into two photons ( $\pi^0 \rightarrow \gamma\gamma$ ). Each of these daughter photons strikes the EMCal and creates an electromagnetic shower via the two processes called Bremsstrahlung and Pair production until the energy of the last

pair produced electrons and positrons runs out of energy, the shower is then recorded by multiple towers and forms a *cluster*. Clusters, which are in the form of electrical signals, are saved using a data acquisition system (DAQ) consisting of various groups of electronic devices using sPHENIX clustering algorithms. The data is then stored on a computing farm, accessible to the end user as a “node tree”. Cluster information can be accessed using the “Fun4all” sPHENIX software framework [44]. In addition to photon clusters, the EMCAL also records electromagnetic clusters from electrons and other charged particles, such as positrons. Due to the various combinations of clusters, there will be background pairs that are uncorrelated to the same  $\pi^0$  mother, in addition to the true correlated pairs. To select the true daughter photon clusters from the true parent pion, suitable cuts or constraints need to be applied when selecting the photon pairs. Figure 3.1 illustrates how photon cluster pairs can occur.

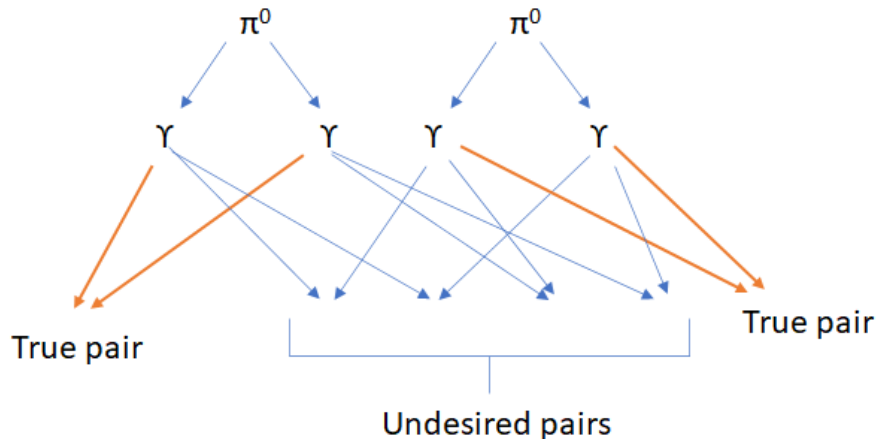


Figure 3.1: Decay of  $\pi^0$  and the possible combination of photon pairs in the case of two  $\pi^0$ . True pair reflects the photons from common parent, while undesired pair forms from the pairing of photons from different parents creating huge background.

When constructing the invariant mass distributions we encounter a mixture of photons originating from different sources than pi0's or just cases where we combine two photons from different pi0's, resulting in some background noise during the calculation. To mitigate this issue, a comprehensive investigation involving numerous trials is necessary to identify the most effective selection criteria that can minimize background interference. Fortunately, we can rely on established standard selection criteria from previous studies as a starting point and adjust them based on the signal-to-background ratio. One such study I conducted focused on determining the optimal transverse momentum ( $p_T$ ) cut for pi0-photon pairs described in the chapter 4. This study allowed us to select an optimal  $p_T$  value for the photon that maximizes the signal-to-background ratio while minimizing statistical errors. The pi0 peak is observed on top of the background originating from these combinatory photon pairs. Considering the aforementioned discussion, we can conclude that pi0 particles can be utilized to calibrate the sPHENIX EMCal.

### **3.2 Development of Pi0 Tower By Tower Method**

The process of calibrating the EMCal using the pi0 method involves accessing the information about the stored clusters from the EMCal detector. The invariant mass is then calculated from pairs of clusters, and the resulting mass is saved as a root histogram. The index of the histogram corresponds to the tower/channel of the EMCal that contains the cluster with the highest energy, known as the “max-Tower”. It should be noted that there are a total of 24,576 towers/channels in the sPHENIX EMCal. Then a histogram fit is performed in the region around the peak, including the peak itself. If the tower (the tower with the maximum energy from the cluster) is not calibrated, the mean value of the reconstructed invariant-mass peak will deviate from the true value of the pi0 mass. To correct for this, the correction value for the tower is calculated using Equation 3.4:

$$\text{tower correction value} = \frac{0.135}{\text{mean value of the pi0 peak from tower's inv. mass}} \quad (3.3)$$

The correction constants obtained from Equation 3.4 are used to adjust the energies of the original cluster. This is done by multiplying the raw tower energy by the correction value. In doing this, in subsequent iterations when we reconstruct  $\pi^0$ s, the histogram peak will be closer to the desired value of invariant mass  $\pi^0$ . The process described above is performed for the subsequent iterations until the tower energies converge to the PDG pi0 mass value. The detailed step-by-step process of the  $\pi^0$  tower-by-tower method can be summarized as follows.

1. Compute the invariant mass by considering the two photon pairs from all events. Before calculating the invariant mass, apply various cuts to reduce the background. Fill the histograms with the values of the invariant mass, where the binning is based on the max tower of the first photon (i.e., the leading photon with slightly higher energy than the other).
2. Fit each histogram around the peak of  $\pi^0$  for each tower using a Gaussian + polynomial function. Extract the peak mean and other parameter values from the fit.
3. Determine the correction factor for each maximum tower based on each cluster. The correction factor is obtained by dividing the desired invariant mass of  $\pi^0$  by the mean peak of the histogram corresponding to that tower. The correction factor varies between towers and iterations. Save the correction factor for all towers in a ROOT “NTuple” file.
4. Apply the corrections and recalculate the invariant mass for the towers. Repeat the steps described above, iterating until the correction values converge to the desired accuracy of the true values. This process typically requires 8-9 iterations, with each

iteration taking approximately 4 hours to complete with the full statistics (referring back to PHENIX). After a certain number of iterations, the maximum mean of the fit  $\pi^0$  closely approximates the desired invariant mass value of  $\pi^0$ , and further iterations do not produce significant improvements. At this point, convergence is achieved. We would have obtained 24,576 constants, each corresponding to an EMCAL channel, which represent the correction factors needed to accurately interpret the EMCAL responses to the incident particles.

A flow chart view of the  $\pi^0$ -calibration method is shown in Figure 3.2.

### 3.3 Basic Method Algorithm and Implementation

The code for this calibration technique's application in sPHENIX is implemented as a C++/ROOT *class* based on the internal sPHENIX *Fun4all* framework. The source files containing this code are named **CaloCalibEmc\_Pi0.cc** and **CaloCalibEmc\_Pi0.h**. The location of this class code is on the official Github page of sPHENIX [44]. Please note that the coding process is a process that is always evolving, and the structure of how the codes might be written and arranged could be changed over time. A brief discussion of the important functions defining the its core functionality for this calibration class is provided below.

- **Initialization:** Initialization of class variables efficiently, such as the arrays containing the correction values, and histogram arrays to store the inv mass. For efficiency to avoid the need to re-process all data from scratch for later iterations, we also initialize and a TTree which is used to store data after the initial analysis run from the sPHENIX Fun4all framework. In this case, a ROOT TTree object is used to store cluster information, such as cluster energy,  $p_T$ ,  $\eta$ ,  $\phi$ , etc.
- **Main Processing of Two-Photon Reco: Process\_Event:** The Process\_Event method is the main methods in this class. It accesses the data nodes which holds the raw

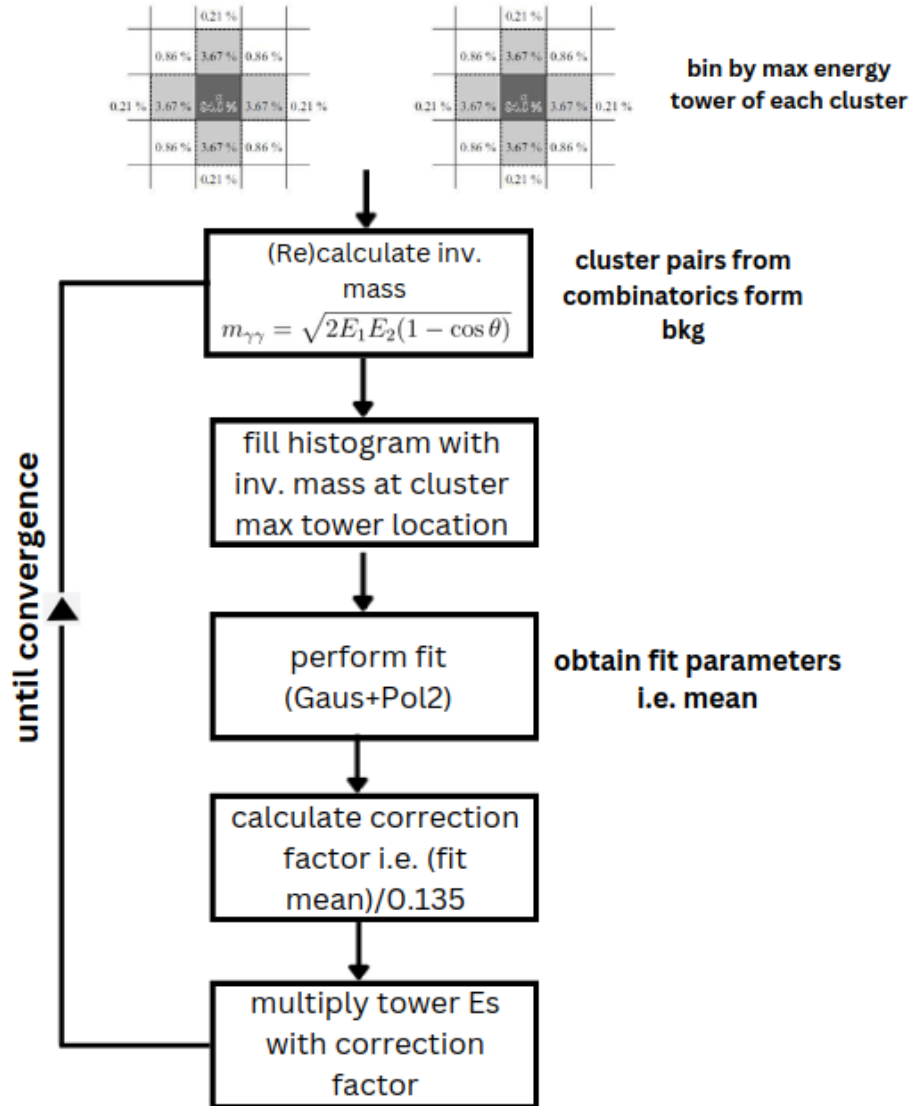


Figure 3.2: Basic flow-chart of the  $\pi^0$ -calibration method. The top cross-line shapes are a representations of the clusters in sPHENIX EMCal.

tower cluster information and saves the data in the TTree. This method is executed for each event, i.e. each collision event. When saving cluster information, some basic cuts are applied to minimize background noise. Cuts are implemented multiple times later on to further minimize background and identify true photon pairs from the same

parent pion. The same two-photon reco processing that occurs in the first iteration is repeated in a slightly different class method in later iterations. This subsequent "Loop" method loops the saved photon clusters from the TTree and reconstructs  $\pi^0$ . It takes the TTrees as input, which contain cluster information for each event rather than the raw data files, which makes it much faster. The invariant mass of  $\pi^0$  is then calculated and saved in histograms for the location of the maximum energy tower of each cluster. It also takes a correction file as input that contains correction constants obtained from previous iterations. These correction values are applied to the original clusters after each generation of new correction files is available to apply in the current iteration. The first iteration does not have a correction file because it is where the correction values are being collected by fitting the  $\pi^0$  histogram for the first time.

- **Histogram Fitting: Fit\_Histos:** This method is used to fit the peak histograms of  $\pi^0$  to obtain the correction values needed for the subsequent steps. Correction values are accumulated from each iteration in a cumulative manner. After the final iteration is complete, all correction values obtained from each step would have been applied.

### 3.4 Implementation

Once the basic functionality of the method has been established, in our implementation in the class described above, it is necessary only to call this functionality in the right order. In our implementation we achieve this with "macro" functions that will utilize the class's functionality. We have developed several macros, each defining specific tasks.

1. Main sPHENIX Raw Data Processing Fun4All\_G4\_Pi0\_Tbt.C a dedicated code to actually run the analysis which uses the sPHENIX software framework is developed into a driver "macro" called Fun4All\_G4\_Pi0\_Tbt.C. It runs the analysis class discussed above, mainly the processing functions/part of the class. Therefore it is during this processing step where is generated initial information about clusters that

hit the EMCal in the form of a ROOT TTree object. After extracting this information, subsequent functionality needs called in order to process the cluster data and calculate the pi0 mass and make the relevant histograms. As described above for all iterations after the first iteration, the same functionality is accomplished more efficiently by driving the same functionality over TTree's stored in the first iteration. Thus a slightly different driving code (in our implementation called the `runLCELoop.C` macro) runs the **TTREE Loop** functionality described above. It iterates over pairs of clusters to calculate the pi0 mass and fill histograms at appropriate locations. In the first iteration, a correction value of 1.0 is used for all cluster energies. In subsequent iterations, correction values are generated from Gaussian fits of the pi0 peak and multiplied with the corresponding cluster energies to calibrate the detector. The correction values are accumulated in each iteration and used to update the corrections to the clusters, fully calibrating the EMCal.

## 2. Fitting and Storing Results from Iterations

(`save_correc_value.C`) The final piece of driving code development involves simply calling the Fitting functionality over the many invariant mass distributions for each tower (or as described later, an integrated group of towers in something called the eta-slice method extension). In our implemenation this driving code is implemented in a macro called `save_correc_value.C` takes the input file generated by the previous step which contains reconstructed pi0 histograms for each EMCal tower location. As described above, this is where the fitting the histogram peak using a second degree polynomial plus Gaussian function is called. The correction values are then calculated as the ratio of 0.135 to the fit mean and saved in a ROOT TNTuple file. This file is read in the next iteration of the `runLCELoop.C` driving macro code, now using this new correction file. This process is repeated until the desired level of accuracy is achieved. The goal is to have histograms for all

EMCal towers with a pi0 peak close to the true pi0 mass of 0.135 GeV, indicating that the EMCal towers are calibrated with the necessary correction values.

### 3.5 Iterative Aspects of the Method

**Iteration 0:** We initiate the process of calibrating EMCal by executing the default driving code as discussed earlier. The output file generated by this code includes properties of all clusters (with energy above 1 GeV), such as energy, pT, eta, phi, and the cluster’s “maxTower” information, which are saved in the ROOT TTree. This file represents the initial state of the EMCal detector clusters from the collision events, without calibration. Initially, the output file is not calibrated and therefore does not produce histograms at the correct pi0 invariant mass location if we reconstruct the pi0. Subsequent iterations involve generating correction files, which are then applied to this initial TTree.

#### Iteration 1:

**Step I:** Execute the TTree ”Looping” `runLCELoop.C` functionality. The input for this file is the TTree output file (which remains the same for all subsequent iterations) and the correction file (which is not provided in the first iteration as it has not been generated yet). The correction values are initially set to 1.00, indicating that if no correction file is provided, the corrections are not actually applied. The ”looping” `Loop()` method of the class is executed, where the correction values are applied to the clusters and the pi0 invariant mass is calculated, and the histograms are filled. The output file contains the histograms for the eta-slices and for each tower in the sPHENIX EMCal. It is important to note that calibrating all the sPHENIX EMCal towers demands a substantial amount of data. Each tower must have sufficient hit information to define a well sampled inv mass peak for pi0. If this condition is not met, we can merge the towers located along each etabin ring of the sPHENIX EMCal in a method extension described below. This approach results in a total of 96 correction factors, one for each etabin ring of the sPHENIX EMCal.

**Step II:** In the next step, we execute the Fitting/Saving `save_correc_value.C` macro functionality. This stage requires two input files. The first file is the output of the previous step i.e. `runLCELoop.C`, which contains the histograms without the fit. The second file is the correction file, which has not been generated yet, so the corrections applied in this step are still 1.00 (that is, no corrections applied). Newly fit histograms are produced and an ntuple containing these fit results with the “real” correction values defined by equation 3.4 to be applied in the next iteration. In this way it saves the correction constants for each sPHENIX EMCal tower.

Our initial iteration has been finished, resulting in the creation of a correction file for the next iteration. This correction file will be used in the second iteration. Each iteration consists of two code blocks implemented in our method as macros: the first one is the `runLCELoop.C` macro, followed by the `save_correc_value.C` macro. These macros are executed with the necessary input files, and the correction files are applied at each stage of the iterations.

### Iteration N:

**Step I:** Subsequent iterations starts by running the “looping” `runLCELoop.C` functionality again. One of the input files is still the original/raw TTree containing the fun4all output file. This file will be calibrated with the optimal correction values obtained from the previous iterations until the end of the process. Additionally, the correction file from the previous iteration (`save_correc_value.C` macro run) is also inputted. Applying the corrections involves multiplying the  $p_T$  and energy of the original EMCal clusters with the aggregate correction values obtained from all the previous iterations up to the current one. Correction files are generated at the end of each iteration, so the latest correction file needs to be applied at every stage. Once the correction file is applied to the original clusters, the histograms should show some improvement and peak around the approximate true pi0 mass energy value of 0.135 GeV. It is worth mentioning that fitting the histograms and

obtaining the peak locations are done in the next step of the iterations during the run of the `save_correc_value.C` macro. The output of this step is again the histogram from the previous iteration of the `runLCELoop.C` run, but this time the histograms are slightly better due to the application of the correction values.

**Step II:** Execute the `save_correc_value.C` macro. The inputs required for this step are the output from Step I of the current iteration, which includes a slightly improved histogram compared to the previous version. Additionally, the correction file from iteration (N-1) is necessary to aggregate the correction values from all the previous iterations.

This process can be repeated until the desired accuracy is achieved. Examples are shown mainly in the next Results chapter, but an initial demonstration of performance is shown in the next section.

### 3.6 Histogram Fitting and Small Simulation Demonstration of Method

Fitting a histogram in ROOT can be quite complex, especially when we need to fit multiple regions of the histogram with different functions. In addition, there is the challenge of tailoring the fitting functions if the distributions are low in statistics. In our case, we used Gaussian fitting for the regions around the peaks of the plots and a second-degree polynomial ("pol2") for the regions on both sides of the peaks. To perform the histogram fitting, we utilized a user-defined combined function that combines a Gaussian function and a second-degree polynomial. An example of such a fit and its appearance can be seen in Figure 4.2. It is important to note that a good fit requires accurate initial parameters provided to the fit function. The detailed steps of the fitting process are described below:

1. While fitting all the individual tower-by-tower etabin-phibin histograms...
2. E.g. for the first tower encountered:

- Find the highest peak (pi0 peaks are quite prominent) of the tower and perform the Gaussian fit around the peak. Only the width parameter has been set to a limit in almost all of the fits.
  - We make TGraph from the data points just below and above the Gaussian region, then we just fit pol2 to this background region. An example of this part of the process is shown in Figure 3.3 on the left panel.
  - The motive of the above two processes is to get the good seed fit parameters for all of tower histograms.
3. We make the total fit function from addition of the above two; and set the initial fit parameters to be as obtained from the above two individual fittings. An example of the total fit is shown in the right panel of figure 3.3. The parameters of the gaussian and pol2 defined by this first fit parameter for the first tower histogram fitted, are also quite good seed values for individual eta-phi histograms with small variations.
4. Once the first fit is done, it is basically doing the same thing as above for each additional tower as well.
5. Using the fit parameters from the seed, most of the time the fit works, but there will surely be a few fit failures here and there. To handle fit failures, we developed a robust "fit rescue" algorithm.
- Since most of the time we are expecting fit peak to be at 0.135 (pi0 mass), I fix the mean parameter to be 0.135 and let the total fit function fit whole range. One advantage of fixing the known parameters is that it will not let the fit fail. Later, we can relax this parameter and unfix the mean parameter to be more realistic.

- Next, just limit the mean parameters (remove the fixparameter, use parlimits) and only fit your 0.06 - 0.3 (your total fit function range). Empirically it is found this fixes 90% of failed fit cases.
- But it is still not complete. So we then perform the above step, i.e. fixparameter and limiting the mean parameter, one more time. This time 98% of fit failures are fixed. The idea of fix and limit is that each time we get closer to the good fit and re-doing fit again because of the previous step good fit parameters re-doing a few times the fit tends to improve and find almost optimal fit parameters.
- For the remaining 2% of fit fails, just repeating above steps will not work, because in the above step we assume that there is peak at 0.135, but because of the de-calibrations, fit peak locations changed and using the fit parameters that assume 0.135 peak will likely most of the time fail.
- So, we needed to come up with conditions that will tell us more information about why the fit failed. For that we employed the  $\chi^2/ndf$  ratio; ideally, this ratio should be 1 for the perfect fit. We will not get that in the real-world, but empirically for our main simulation tests (shown in the results section) we find that a limit of 2.7 of the  $\chi^2/ndf$  ratio as a good threshold to consider as the good fit. This max chi2 value needs re-adjusted according to the statistical sample being analyzed generally. Any fits with a ratio greater than this value were considered to be failed and were treated separately inside the condition loop of the code. It is first tested if the peak has moved below 0.135 for example, maybe to 0.128. So we do the same thing. i.e. fix the parameter to 0.128 and next time just limit around it, this fix peaks that were moved lower due to decalibrations.
- Pi0 peak might also move above 0.135, say 0.145. This will also give the  $\chi^2/ndf$  ratio larger, so it also goes into conditions and when it is tested with 0.145 peak

assumption conditions, this will also work. Once we incorporate all the different scenarios we get 100% fits working. No fit fails.

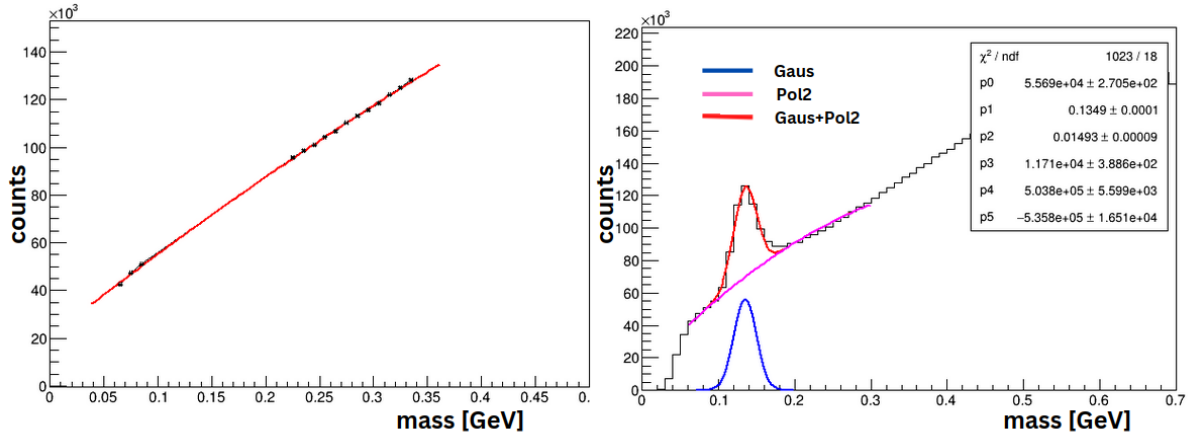


Figure 3.3: Demonstration of the fit method I devised. Left: Plotting only the background part of the histogram just below and above the peak area with second degree polynomial. The idea is to gather as many good seed as possible for the later total fits of the histogram. Right: All three part of the fitting function shown together.

Figure 3.3 illustrates the fitting method that I developed as discussed above. On the left side of the figure, we observe the second-degree polynomial function fitted to data points that are collected from just above and below the nominal  $\pi^0$  peak region. This approach aims to provide a good seed for the overall total fit function needed later, which is depicted on the right side of the figure. The plot on the right shows that the overall fit function (shown in red), which is a combination of a Gaussian and a second-degree polynomial, aligns with the histogram data very well.

Quality Assurance (QA) checks are carried out by looking at each individual fit of all histograms with the eye. Although  $\chi^2 / \text{ndf}$  was by definition in an acceptable range, as indicated in the above algorithm components, we wanted to verify that each fit looked



Figure 3.4: Fits on all the eta slices (or eta rings) to do the sanity checks by eye that the fits are not failing in any of the eta slices.

reasonable. An example is Figure 3.4 for the eta ring method, which will be described in a subsequent section of this chapter which involves only 96 fits at a time. The figure shows all 96 fits in a single plot. Even though each fit is small, it allows us to verify that every fit looks reasonable and, if not, easily identify any failed fits.

In the case of tower by tower, there are 24,576 such fits to inspect. Pages with similarly large number of fits on each page, using a full 8x16 plots per page showing 128 fits that required looking through 192 pages, were also made. One such page with 128 fits is shown in Figure 3.5. All fits were found to look reasonable, since the chi<sub>2</sub> / ndf requirement was designed to ensure.

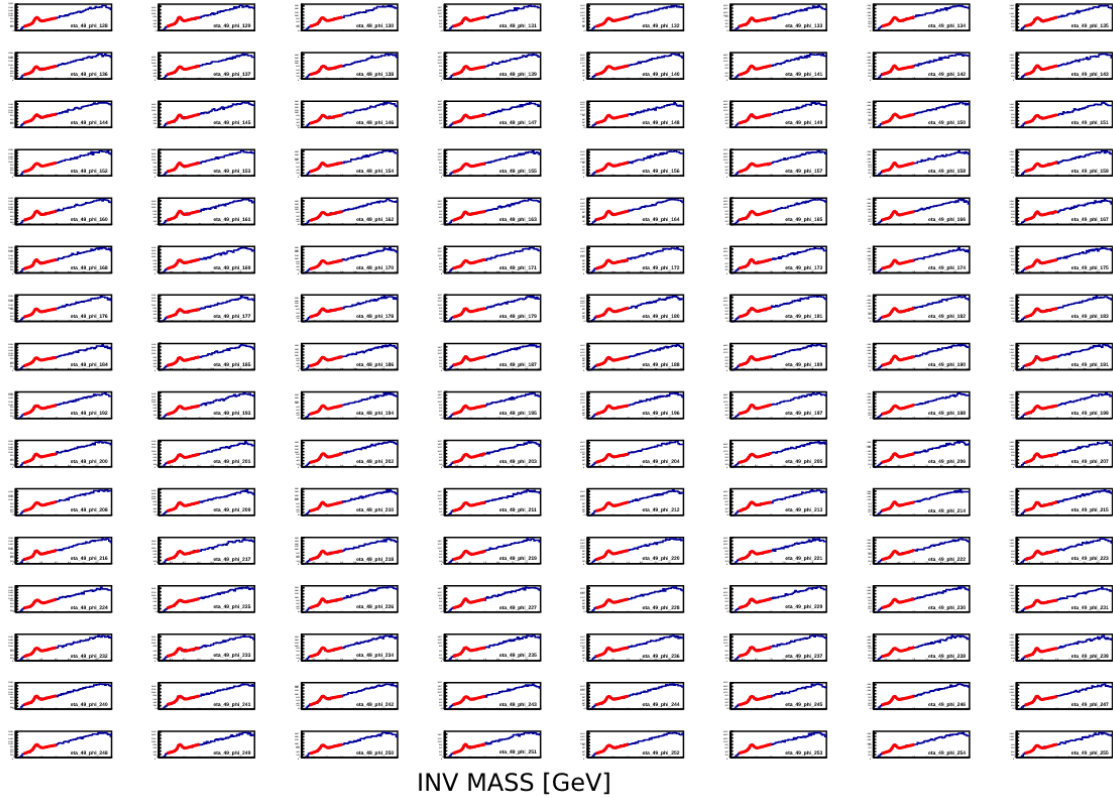


Figure 3.5: One of 192 pages of each tower fits. Each page consists of 128 fits to inspect. Quickly inspecting such plots is a good way to do the sanity checks if the fit fails or not.

With the base method established, an initial demonstration of the method, we first applied it to a small 16x16 tower detector subsection. A decalibration was applied that can be seen in the first panel of Figure 3.6. The x-axis is the etabin and the y-axis is the phibin of the sPHENIX EMCAL detector. The z-axis of the plots shows the pi0 peak values for these 16x16 towers. In each iteration, we apply the correction factors to the towers as discussed previously. It can be observed that the initial pattern observed in iteration 0 becomes smoother after iteration 7. Furthermore, most of the towers' pi0 peak aligns with the desired pi0 mass value of 0.135 GeV.

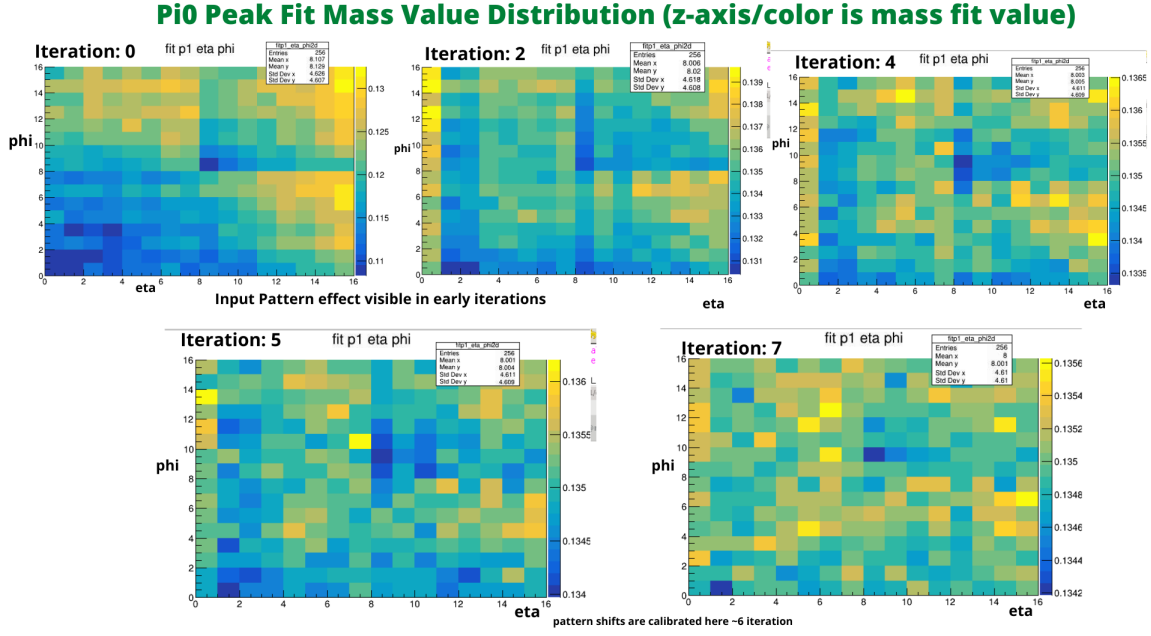


Figure 3.6: Pi0 Tower by Tower (TbT) method applied to calibrate small 16x16 region of sPHENIX EMCAL. Initially we see some decalibration shifts i.e. some kinds of pattern which is removed after few iterations. All of the towers in the final iteration aligns pi0 peak mass of 0.135 GeV.

### 3.7 Method Extension: Eta Ring by Eta Ring Method

The sPHENIX EMCAL is essentially a cylindrical detector, as illustrated in Figure 3.7. The letters 'S' and 'N' at the top denote the South and North directions, through which the beamline passes. If you imagine unfolding the cylinder into a flat plane, it resembles the figure at the bottom. Each vertical column in the bottom figure represents an eta slice, or eta ring. Each eta slice comprises 256 towers aligned in the phi direction. The sPHENIX EMCAL consists of a total of 96 such vertical columns, ranging from bin numbers 0 to 95 from left to right.

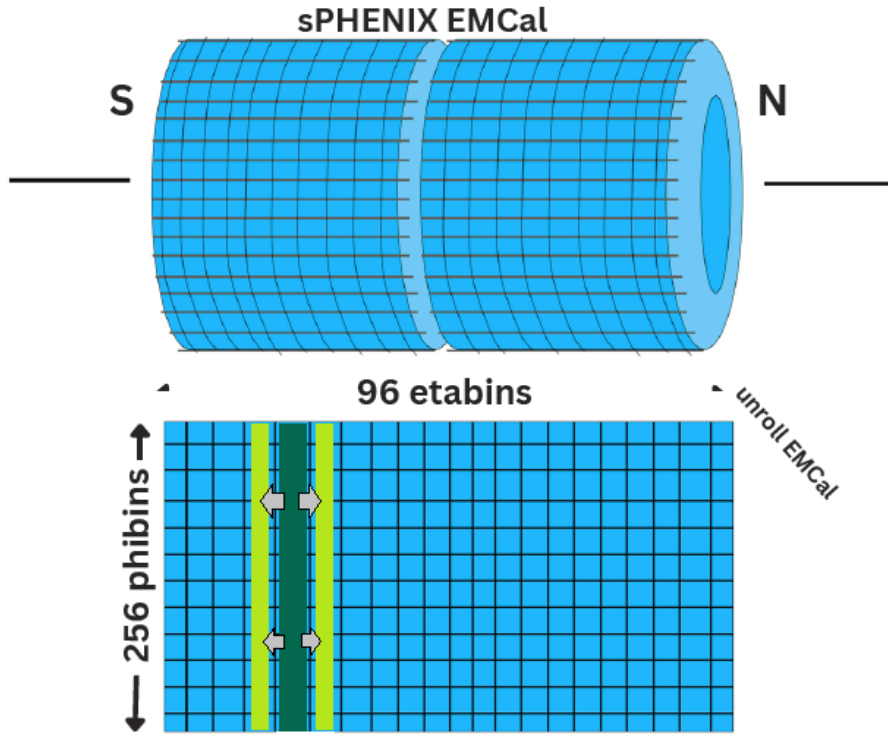


Figure 3.7: sPHENIX EMCAL barrel shape representation. S and N represent the South and North direction where beamline runs through. The bottom part is the representation of the unrolled sPHENIX barrel shape. Each column is considered at eta slice i.e. eta ring with 256 towers in them. There are total of 96 eta slices in the sPHENIX EMCAL.

The primary aim of the pi0 method is to calibrate each of the 24,576 sPHENIX EMCAL towers. However, this method requires a large statistical sample to adequately fill all towers with a sufficient number of entries. For instance, during RHIC Run-23, we had a smaller statistical sample. Despite this, we still need to calibrate the sPHENIX EMCAL detector. An alternative to the tower-by-tower calibration approach is calibrating the EMCAL using eta slices (eta ring). The eta slice calibration follows the same procedure as the tower-by-tower method, with the only difference being that instead of calibrating each individual tower, we calibrate each eta slice. This means that all towers within a single eta slice will share the

same calibration constants. Essentially, we integrated 256 towers into one tower, allowing us to combine the statistics and perform the pi0 method to obtain the fits and calculate the correction values. The calibration technique performed effectively at the eta slice level because of the ample statistics.

The method of utilizing the eta slice and aggregating all towers in the phi direction is based on the idea that the physics of pi0 reconstruction remains essentially consistent for the towers within the eta slice. That means that towers within the same eta-bin can be considered to have the same correction factors because the detector's response to a pi0 impacting the towers within the same eta-bin should be fairly consistent, given that these towers are symmetrically equidistant from the sPHENIX detector's collision region.

In this case we integrate an entire eta slice's (all towers within) invariant mass distributions. The correction value is obtained as before from the fit to the pi0 peak but now for the entire eta-slice:

$$\text{eta slice correction value} = \frac{0.135}{\text{mean value of the pi0 peak from integrated eta-slice inv. mass}} \quad (3.4)$$

This is defined for one iteration as for the tower method above. The correction values are then applied to each entire eta-slice (every tower within) and the invariant mass reconstruction is re-run again with the integrated eta-slice inv mass histograms collected again and again in the later iterations. Now there is a somewhat reduced probability that the 2nd photon lies in a different eta-slice (for example the adjacent slices) because some decays will produce both photons within the same slice. Therefore we expect this kind of “1-D” calibration unfolding to require less iterations than for the full 2-D tower by tower technique. As shown in the results section next we indeed do observe this to be the case.

## 4 sPHENIX Pi0 TOWER-BY-TOWER CALIBRATION TECHNIQUE :

### OPTIMIZATION AND RESULTS

In this chapter, we will discuss some of the quantitative results obtained using the tower-by-tower and eta ring by eta ring pi0 calibration method. First we also present the results of a study to optimize the method by determining what are the best kinematic cuts in order to maximize the statistical precision, or equivalently, minimize the time-span/integrated data needed to perform the method.

#### 4.1 Optimization of Kinematic Cuts for Maximizing Statistical Precision

We first set out to determine the optimal pi0 photon transverse momentum ( $p_T$ ) value that minimizes the relative statistical error, improves the signal-to-background ratio (S/B), and ensures reliable fits for each of the 24,576 sPHENIX EMCal towers. The primary requirement for the calibration analysis module is to ensure that the fit of each EMCal tower with a pi0 peak is successful. Manual adjustments to correct failed fits are not preferred. To increase statistics, the value of the energy parameter of the photon can be lowered during the selection of pi0 particles. Because it is known that the spectra of all particles at RHIC increase very sharply at very low energies (around the QGP temperature of  $\sim 300$  MeV), reducing the  $p_T$  cuts of the photon can accumulate more statistics, slightly increasing the signals. However, this will also raise the background counts. If the combinatorial background increases faster than the signal as the photon's  $p_T$  is lowered, there may be optimal photon  $p_T$  cut values to maximize statistical precision. The goal of this chapter is to find an estimator function that reflects either of the behaviors of lines A or B shown in Figure 4.1. If the statistical error behaves according to path A, we aim to determine the photon  $p_T$  value that minimizes the statistical error and also ensuring that the fit does not fail in the later analysis. Conversely, if the statistical error matches path B in Figure 4.1, choosing a

very low photon  $p_T$  could theoretically reduce the statistical errors. However, such a low photon  $p_T$  would significantly increase the background, overshadowing our signal peaks and leading to failed fitting in the later analysis, which we want to avoid. Therefore, the goal is to estimate the curve's behavior and determine the optimal photon  $p_T$  value.

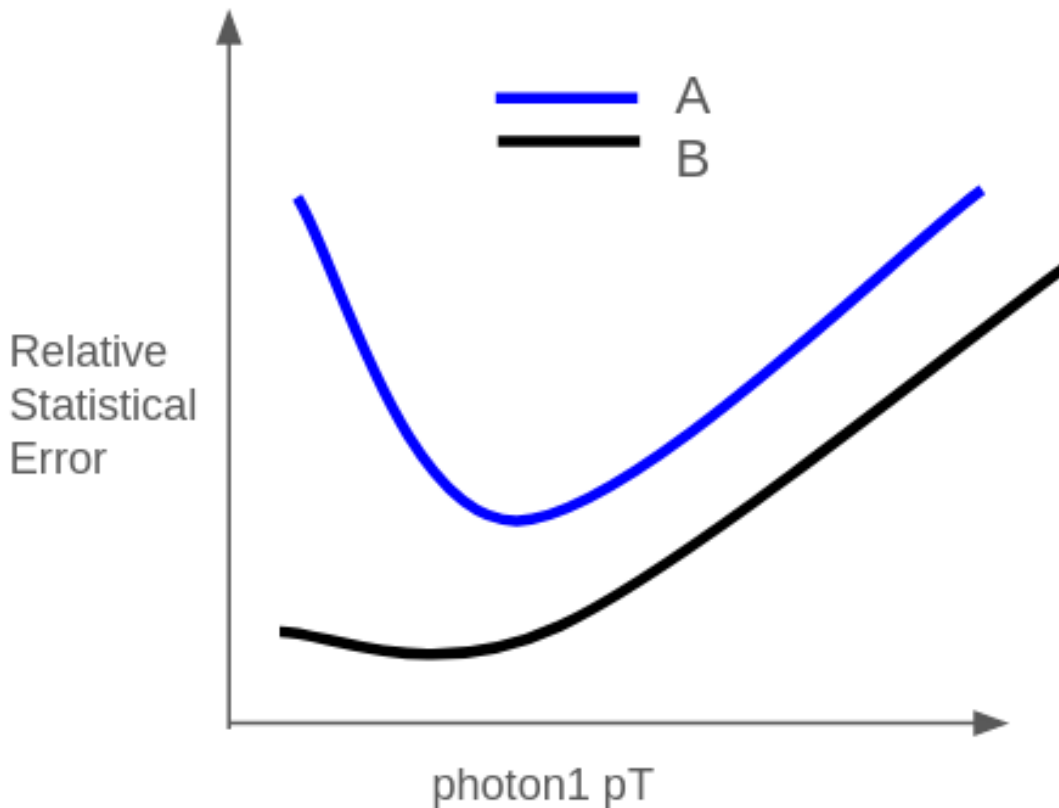


Figure 4.1: An estimator function whose shape needs to be determined. The most likely curve for the estimator function will be the blue (A) [online] as the relative error tends to increase after some lower limit on  $p_T$  because too much background starts to accumulate then. The x-axis photon1 pT denotes the pT of one of the photons of pi0 decay photons.

The purpose of the estimator function is to avoid the need to perform a real analysis for every possible  $p_T$  value of the pi0 daughter photon. It is time consuming to test each

case with a single photon  $p_T$  cut value, and it is also likely that the fit will fail with lower  $p_T$  cuts. Therefore, the estimator function extrapolates the behavior using a few specified  $p_T$  pi0 photon cut values. This allows us to determine the optimal value and minimize the relative statistical error at the same time.

Our analysis module was used with a minimum energy cut of 0.6 GeV for both photons. This lower energy cut was implemented in order to perform an optimal cut study, where we evaluated the effects of varying the  $p_T$  cut for the photon down to 0.7 GeV for one of the leading pi0 photons. We selected the first photon (referred to as photon1) on the basis of higher energy cut values. Specifically, we considered  $p_T$  values of 0.7, 0.9, 1.1, 1.2, 1.35, and 1.65 GeV for photon1, while keeping the  $p_T$  of the second photon (referred to as photon2) just above 0.6 GeV for all cases in the optimal photon study. It is important to note that the optimal photon cut study was conducted for each etabin slice, rather than the entire EMCAL tower-by-tower. Each etabin slice consists of 256 towers, with etabin slice 0 corresponding to a pseudorapidity of approximately -1.1, etabin slice 50 corresponding to a pseudorapidity of approximately 0, and etabin slice 94 corresponding to a pseudorapidity of approximately +1.1. To illustrate the method, let us consider etabin slice 50. We varied the  $p_T$  of photon1 and performed a histogram fit for each  $p_T$  value. The signal and background counts were calculated using a simple side-band analysis. Two background regions were selected above and below the pi0 peak region, as depicted in Figure 4.2.

In this approach, we first compute the mean of the fit. Then, within a range of  $2.5\sigma$  around the fit mean, we identify the signal and integrate to determine the signal value. We then divide the signal range into the same number of bins as the signal covered. Moving to the lower end of the fit, we integrate that region to establish the lower background (bkg) region. Similarly, we calculate the upper background region. After obtaining the counts for all three regions, we calculate the total background for further analysis by taking the average of the two background regions. To determine the signal counts, we subtract this average

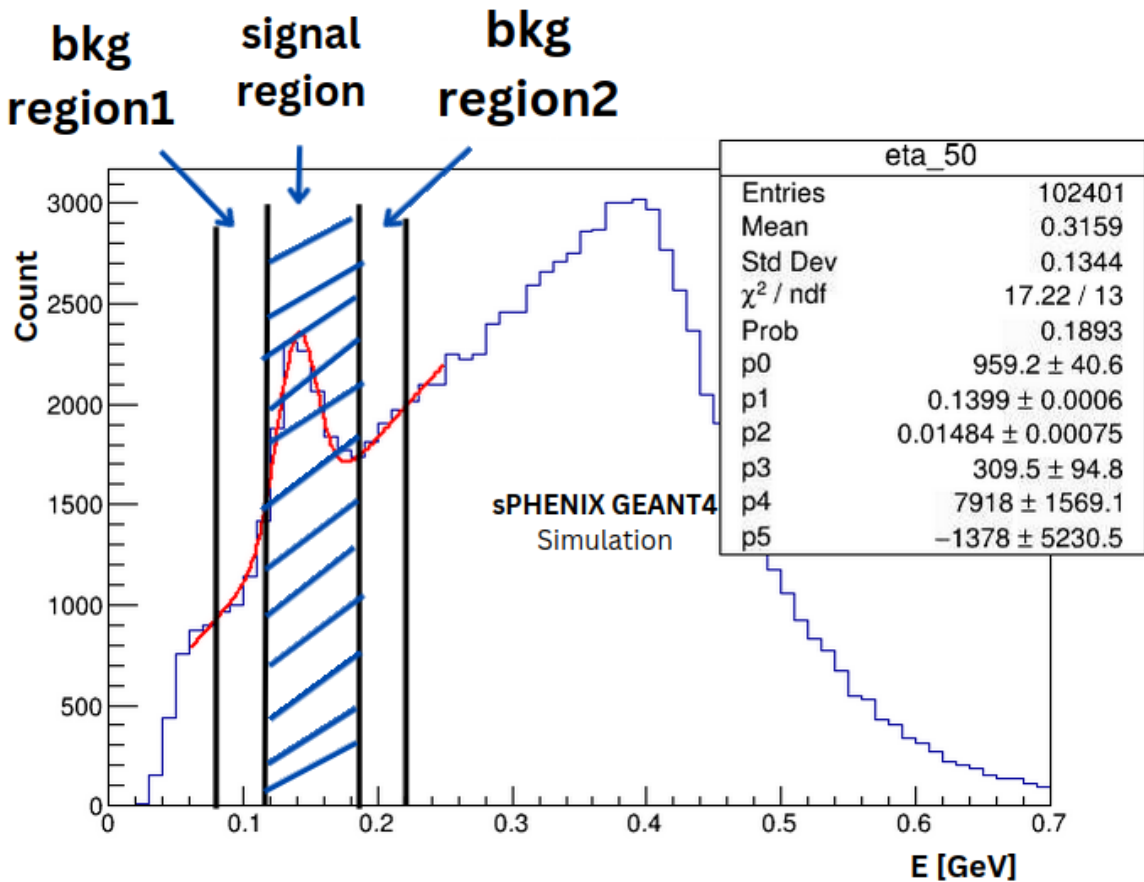


Figure 4.2: Signal and background region selected using the simple side-band analysis method. Once the signal and background regions are selected we can just count use the integral function of the ROOT to calculate the counts of the signals and background values that is used later in the equations.

background from the previously calculated signal. This process yields the signal counts. With available signal and background counts, we can create plots of signal counts versus photon1  $p_T$  for each etabin. In addition, we plot the background counts versus photon1  $p_T$ . For example, refer to Figure 4.3 and Figure 4.4.

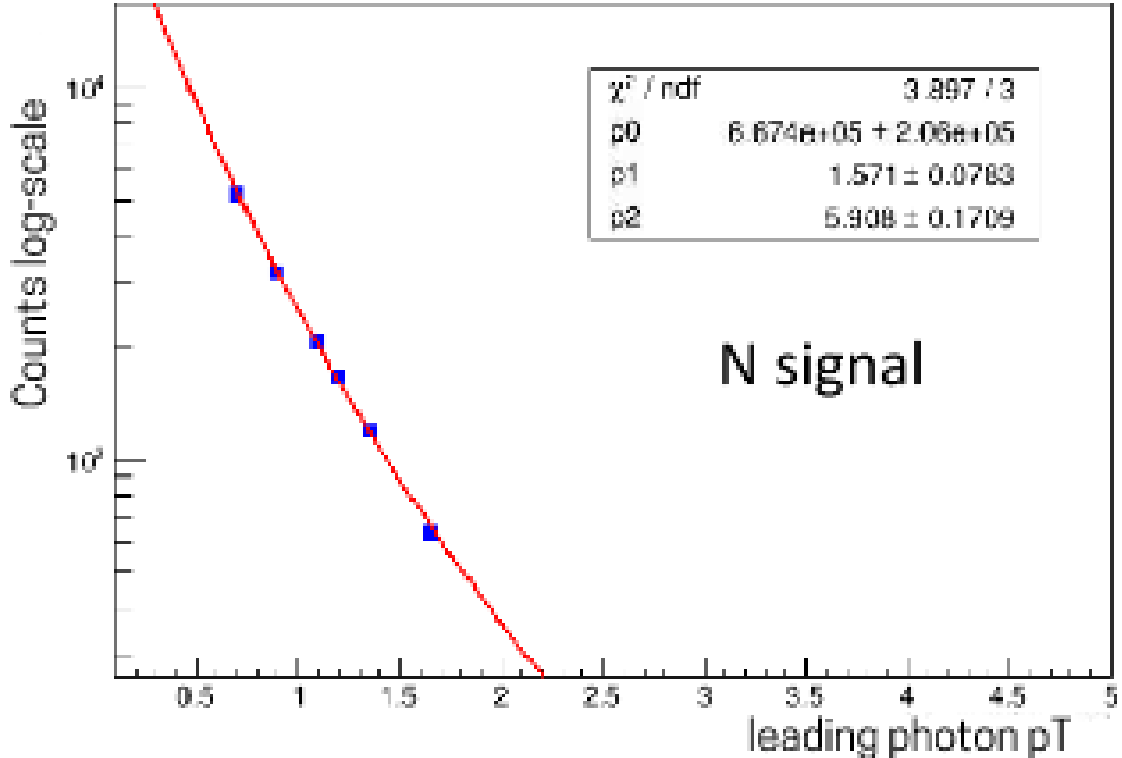


Figure 4.3: Signal vs. photon1  $p_T$ . The blue marks are the counts of signal region. The red line is a fit.

We utilized a modified power law to fit the signal counts and the background counts, which is typically observed in RHIC energy spectra. The specific form of the modified power law that we used is shown in Equation 4.1:

$$\frac{dN}{dE} = \frac{p_0}{(p_1 + E)^{p_2}} \quad (4.1)$$

where  $p_0$ ,  $p_1$ , and  $p_2$  are the three fit parameters of the function.

The fit appears to be satisfactory, and subsequently we gather all three fit parameters. Likewise, we repeat the same procedure for background counts and gather the fit parameters for the background as well.

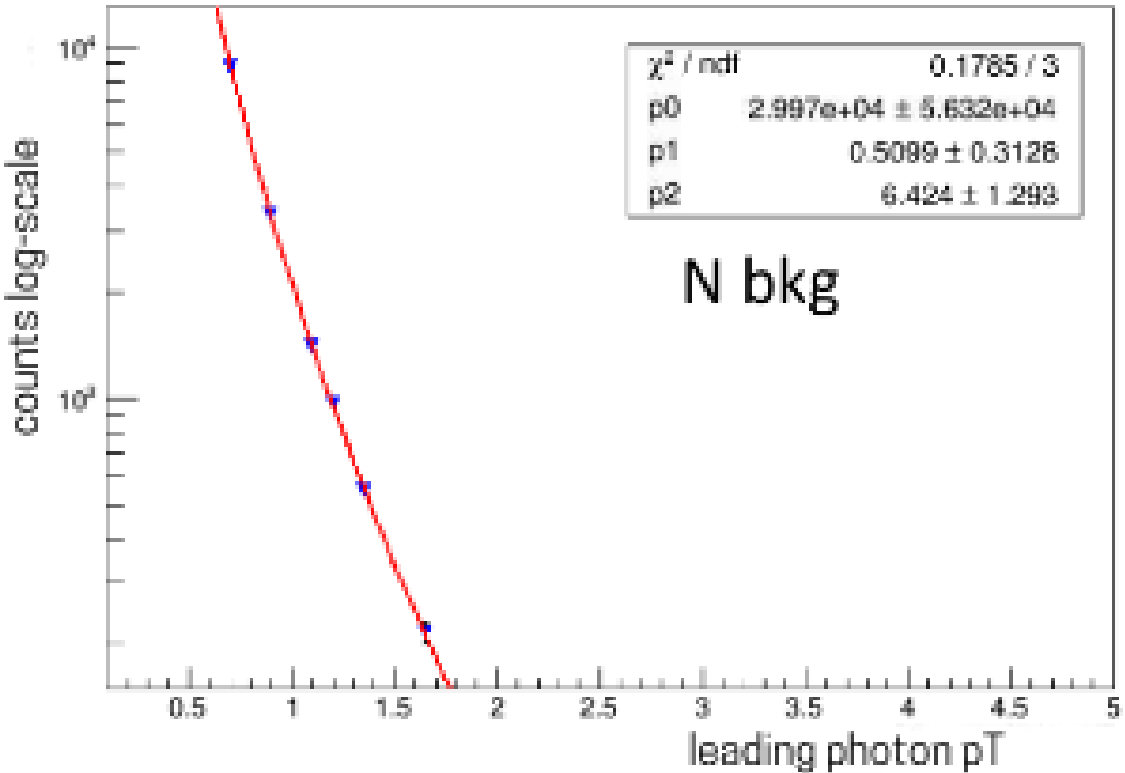


Figure 4.4: Background vs. photon1  $p_T$ . The blue marks are the counts from the background region. The red line is a fit.

After obtaining the fit parameters for both the signals and the background, we proceed to select the most suitable estimator function by exploring various forms that incorporate both the signal and the background counts. Ultimately, we opt for a slightly modified version of the estimator function utilized in PHENIX, as described in the documents authored by Christian Klein-Boesing (<https://zenodo.org/record/4267413>). We prioritize this particular estimator function over other similar alternatives because it yields values that closely align with the true relative error of the fit, which would not have any background contributions in an ideal scenario. This relative error represents the ratio of the fit error in the peak mean to the peak mean itself, and it serves as an ideal scenario when there is no background

contribution. Hence, our chosen estimator should provide a relative error estimate that closely approximates this ideal value.

The Table 4.1 displays the relevant information that I described above (just for one etabin slice number 50) where  $p_1$  means the first parameter of the fit that we obtained from the signal plot and  $p_2$  is the standard deviation of the fit. In the table, the first column  $\sigma_m/m$  represents the relative error of an ideal scenario without background contributions where  $\sigma_m$  is the standard deviation of the pi0 fit value, and  $m$  is the pi0 fit value itself. Only column 4 with estimator form  $p_2/p_1 \sqrt{N_S + 2N_B}/N_S$  contains values that closely match the ideal scenario values in column 1. Thus, column 4 serves as our preferred estimator form. The alternative variations of the estimator function show no better similarity.

The form of estimator function looks like that in Eq. 4.2;

$$\text{estimator of } p_1 \text{ error} = \frac{\sigma_m}{m} \frac{\sqrt{N_S + 2N_B}}{N_S} \quad (4.2)$$

The estimator function demonstrates good performance for the six data points, indicating the presence of a minimum within the range of  $(0.4 - 0.8) p_T$ . This minimum represents an ideal scenario with minimal relative statistical error, but it also corresponds to higher background and overall statistics. Consequently, selecting the minimum for the calibration analysis would introduce a significant amount of background into the histogram plots, resulting in a lower signal-to-background (S/B) ratio. To address this, we choose a different region, specifically  $(0.9 - 1.2) p_T$ , as the optimal cut for our leading photon's  $p_T$ . This region still offers good statistical precision while reducing the background and minimizing the risk of fitting failure. Ultimately, the final decision on the  $\pi^0$  photon  $p_T$  value will also consider the reliability of the fit. Thus, this study provides valuable information to select an optimal photon  $p_T$  value.

Table 4.1: Comparison of  $p_1$  ( $\pi^0$  fitted mean) parameter from the fit with the various possible estimator functions.

etabin number ( $p_T$ )	rel_errfit = $\frac{\sigma_m}{m}$	relerr2_p1 = $\frac{p_2}{p_1} \frac{\sqrt{N_S+N_B}}{N_S}$	relerr3_p1 = $\frac{p_2}{p_1} \frac{\sqrt{N_S+N_B}}{N_S}$	relerr4_p1 = $\frac{p_2}{p_1} \frac{\sqrt{N_S+2N_B}}{N_S}$	relerr5_p1 = $\frac{p_2}{p_1} \frac{\sqrt{N_S+2N_B}}{N_S+2N_B}$
eta_50 (1.65)	0.0046115	0.0043442832	0.00187236	0.005441649	0.00149478
eta_50 (1.35)	0.0048611	0.003714161	0.00109864	0.004427523	0.00084799
eta_50 (1.2)	0.0044739	0.0033104393	0.00087479	0.004361431	0.00066399
eta_50 (1.1)	0.0041369	0.0030849174	0.00071180	0.004103364	0.00053513
eta_50 (0.9)	0.0037698	0.0026500768	0.00049407	0.003568821	0.00036688
eta_50 (0.7)	0.0035029	0.0024345073	0.00031915	0.003328165	0.00023345

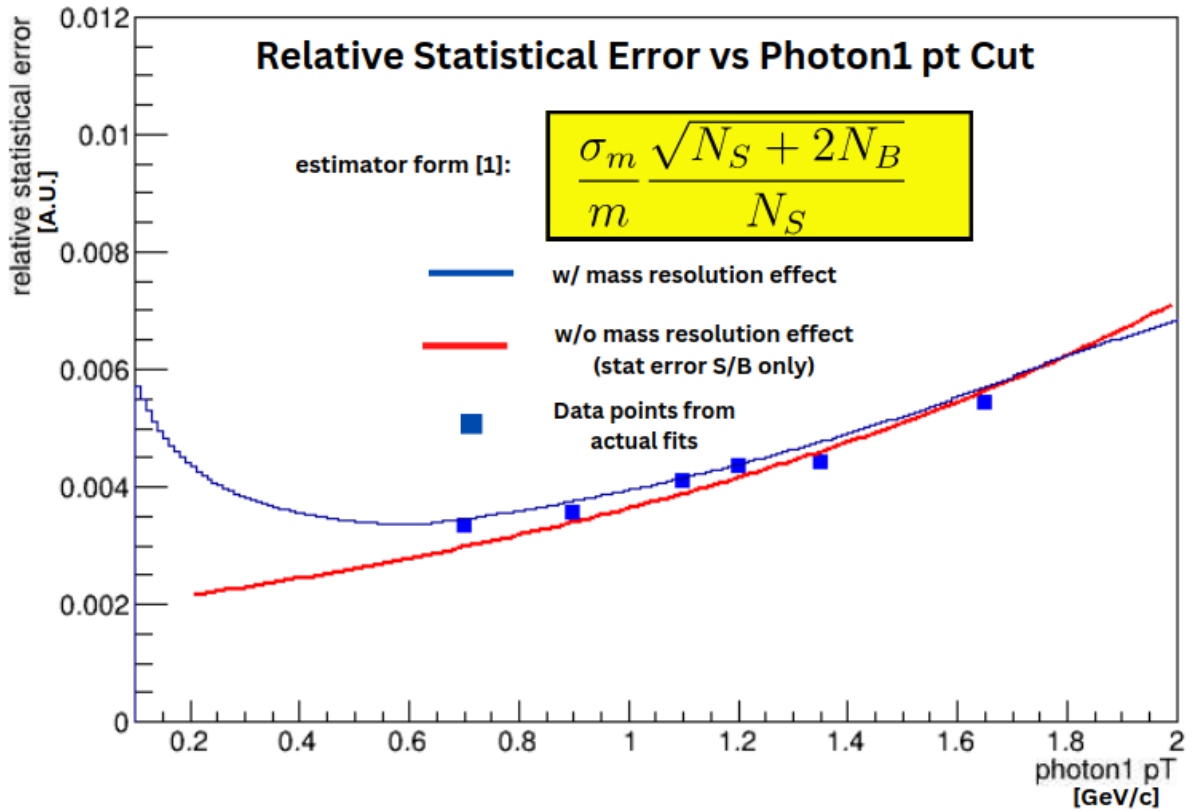


Figure 4.5: An estimator function showing that there exists a optimal photon  $p_T$  that minimizes the relative statistical error. Blue line is taking mass-resolution into account, and red line without the mass-resolution effect. The simple estimator function follows the data-points reasonably.

## 4.2 Simulation Test Results of Pi0 Tower by Tower Method

The sPHENIX EMCAL is initially calibrated at the base level, as illustrated in Figure 4.6. The value of the root mean square (rms) depicted in the figure corresponds to approximately 2% non-uniformities in the responses of the EMCAL towers without implementing the pi0 method. The x-axis is the pi0 mass in GeV obtained by fitting each of the sPHENIX EMCAL

towers. There are 24,576 such EMCal towers. The y-axis represents the number of EMCal towers.

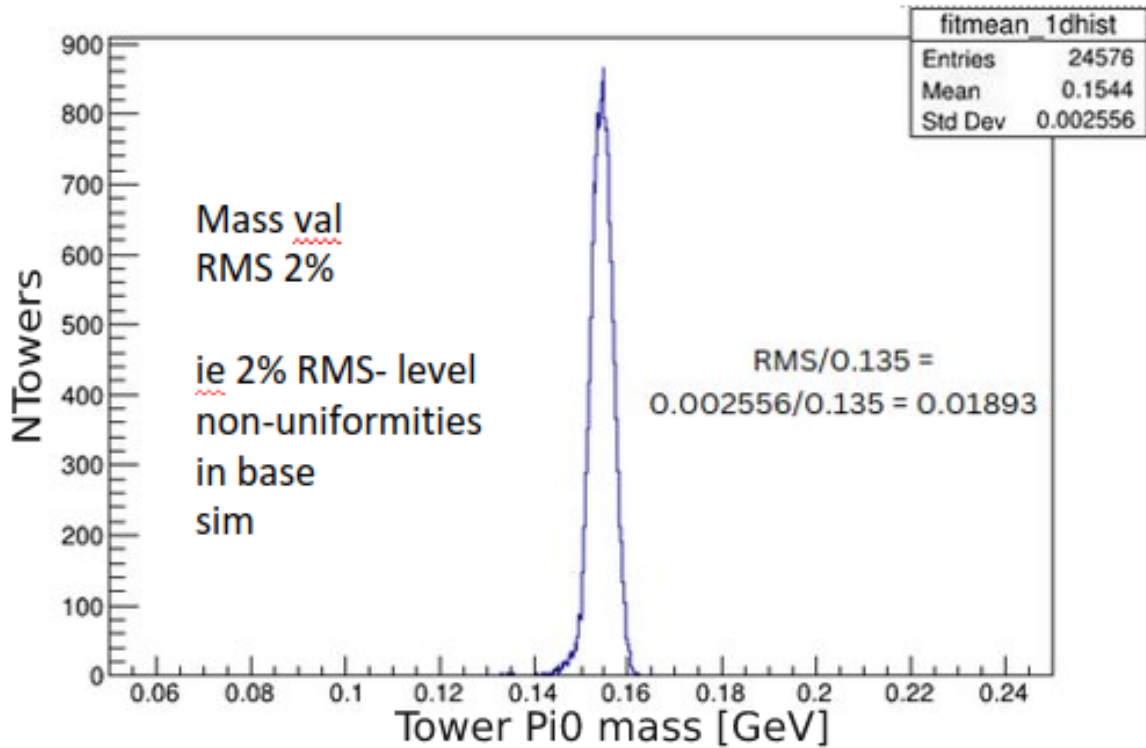


Figure 4.6: RMS of base level sPHENIX EMCal response to  $\pi^0$ s. Base level non-uniformities is within 2.0 %.

Nonuniformities are calculated using equation 4.3;

$$\text{Non-uniformities in \%} = \frac{\text{RMS (Std Deviation)}}{0.135} \times 100\% \quad (4.3)$$

Additional plots were generated to provide an aid for a more comprehensive analysis and improve our understanding of the calibration status. These plots are shown in Figure 4.7 and 4.8. Figure 4.7 represents a 2D-histogram, where the z-axis represents the pi0 mass obtained from the fits. In this plot, we can also observe the TPC support regions at four different locations, which correspond to the configuration of the sPHENIX EMCal. The TPC

is a support structure for the EMCAL, which is made of hard steel, and obviously the towers around those steel structures will not record all the energies they get hit by  $\pi^0$  particles. The x-axis shows the 96 etabins and the y-axis shows the 256 phibins.

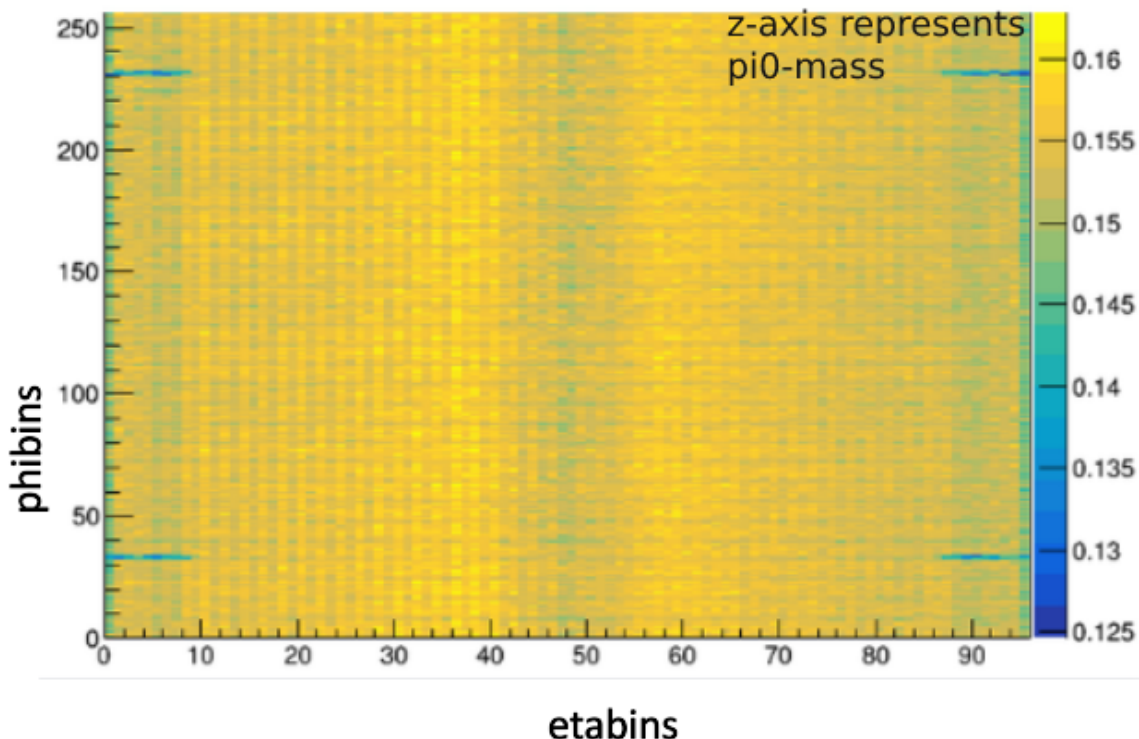


Figure 4.7: sPHENIX EMCAL 2d histogram showing the response to  $\pi^0$  particles. The z-axis shows the mass value of  $\pi^0$  obtained from the fits.

Figure 4.8 illustrates a 1D-histogram, which is a projection of Figure 4.7. It displays the  $\pi^0$  mass locations for 24,576 towers without the  $\pi^0$  tower-by-tower calibration method applied yet. The x-axis indicates the tower numbers, beginning at etabin 0 and progressing through phibin directions, continuing through etabin 1, and so forth until etabin 95 is reached and the phibins for etabin 95 extend to 255. The y-axis depicts the  $\pi^0$  mass values obtained from fitting the histograms at each tower location. The EMCAL baseline calibration exhibits noticeable fluctuations in the figure. Nevertheless, the figure reveals a symmetrical structure,

suggesting that the detector's left- and right-hand sides operate similarly, as the collision point is centrally located within the EMCAL detector. This observation further supports the accuracy of the detector layout and our  $\pi^0$  calibration method.

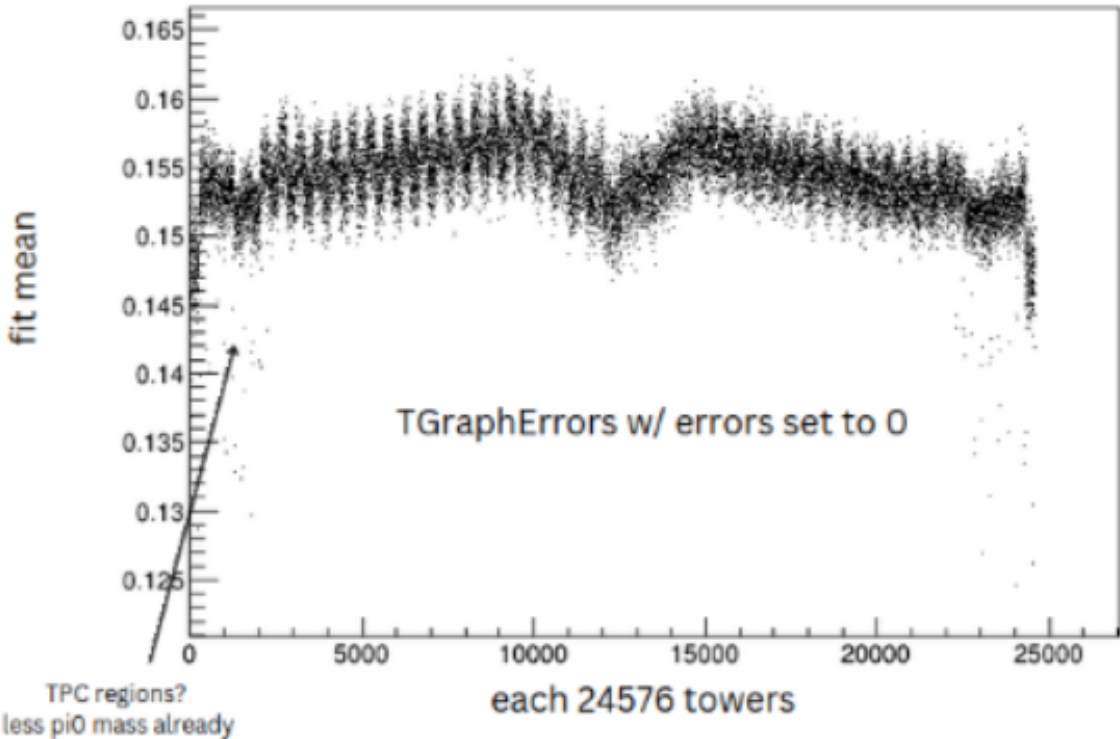


Figure 4.8: The one-dimensional histogram of the Figure 4.7. We can see that several towers near the TPC regions do not have  $\pi^0$  mass values well-aligned with the target of 0.135 GeV.

Due to the base-level sPHENIX EMCAL response having only a slight nonuniformity of approximately 2% as seen above, we implemented a significant decalibration pattern to generate a varying  $\pi^0$  mass range from 0.11 GeV to 0.16 GeV. The decalibration values we applied were intentional and were multiplied to the photon's energy values that gets reconstructed to the  $\pi^0$  particles. This dramatic decalibration pattern was applied in order to do the real testing of our  $\pi^0$  calibration method. After applying the decalibration to the

EMCal, we observed the same 2D-histogram as before, as shown in Figure 4.9. The white spots visible in the plots indicate the histograms that we identified/labeled as dead-towers, where no data is recorded at those locations. We have tried to implement a reasonable amount of decalibrations among the EMCal towers.

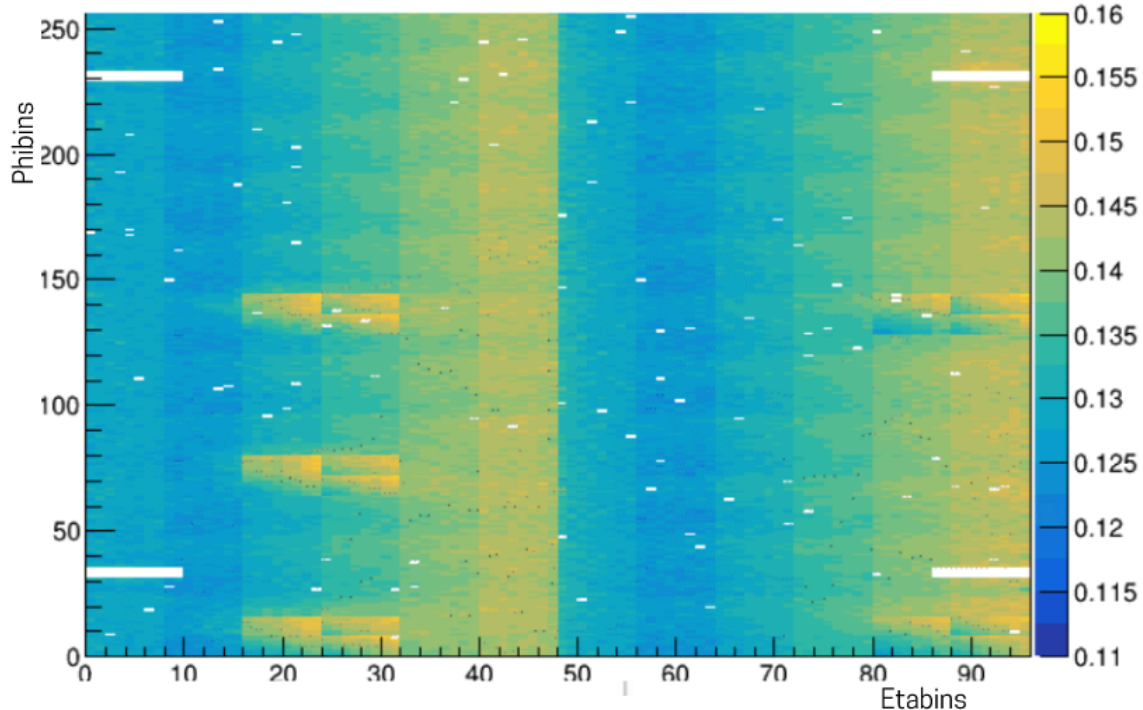


Figure 4.9: Decalibration pattern applied to sPHENIX EMCal which forces  $\pi^0$  mass to vary from 0.11 to 0.16 GeV. The white spots are considered as the dead-towers and so those histograms won't get filled. The z-axis is the fitted  $\pi^0$  mass for each towers.

Figure 4.10 illustrates the extent of the  $\pi^0$  mass fluctuations that we intentionally implemented to the EMCal towers. Upon implementing the decalibration, it becomes evident that the nonuniformities have escalated to a significantly higher magnitude, reaching approximately 4.85%. The pattern on the left part of the EMCal is repeated on the right part of the EMCal along the etabins direction. To make things even more spicy, there is

also small pattern within the left and right side of the EMCAL that makes changes to the  $\pi^0$  mass along the phibin directions. Overall, the pattern is complex enough and should be good testing of our  $\pi^0$  calibration method.

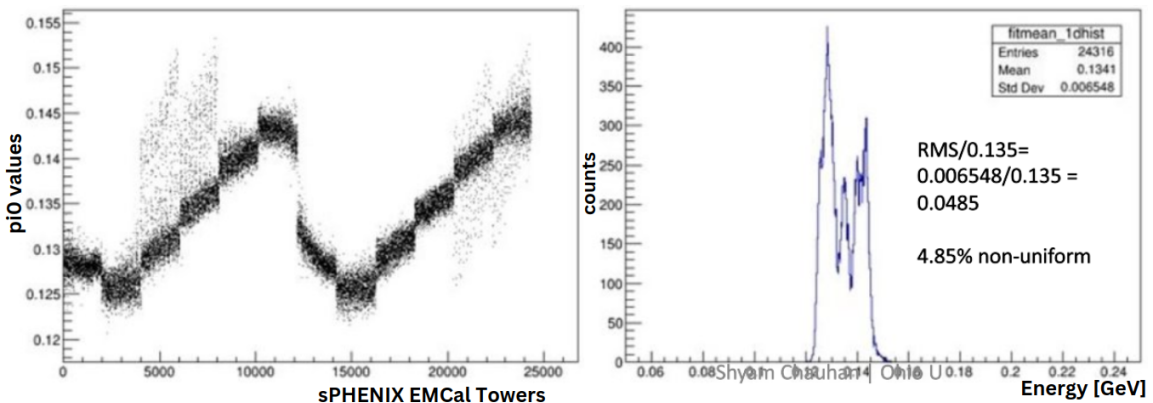


Figure 4.10: Fitted  $\pi^0$  mass values as seen by the sPHENIX EMCAL after applying the de-calibration patterns. Non-uniformities have now increased to about 5% in the EMCAL.

The sPHENIX EMCAL  $\pi^0$  response after completing the calibration is described here. It took approximately 11 iterations to achieve the optimal calibration state for EMCAL using these data. To perform each iterations, with the amount of data and the software setup I had, it took about 30 minutes. Figure 4.11 illustrates the level of precision that has been achieved. Non-uniformities have been reduced to below 0.10%.

Figure 4.11 provides evidence that our method works effectively even at the tower by tower level in addition to the eta slice level described in the section 4.3 and has achieved the desired level of accuracy. However, we also wanted to present an additional plot that demonstrates the successful recovery of the de-calibration pattern that was intentionally implemented at the EMCAL towers using our  $\pi^0$  calibration method. The Figure 4.12 illustrates the extent to which our method has accurately restored the input de-calibration shift values. The z-axis value on the right side of the figure represents the ratio of the input

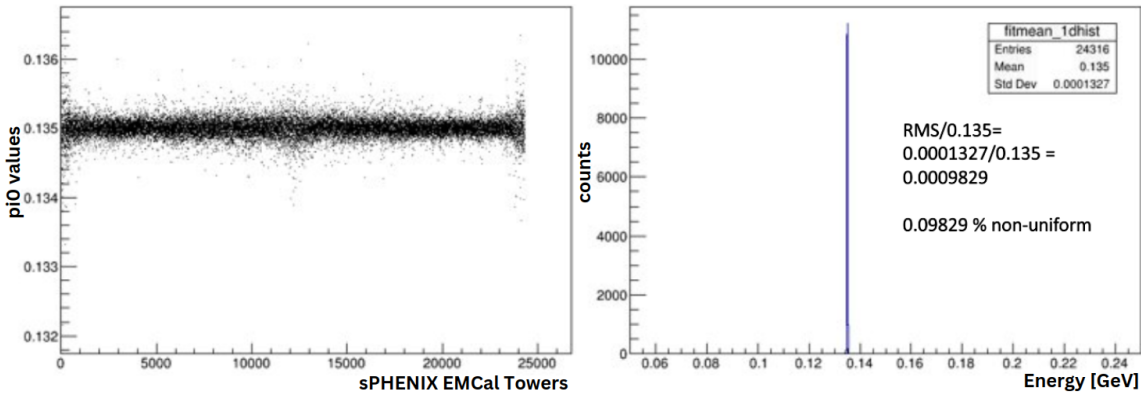


Figure 4.11: State of the calibration after 11 iterations. The non-uniformities calculated using RMS (std. deviation) has dropped to less than 0.10%.

de-calibration to the correction values before calibration, divided by the final best correction values. As the final correction values are an aggregate of the correction values, they should contain information that reverses the effects of the de-calibrations. In other words, z-axis values of 1.00 indicate that our method has perfectly recovered the input de-calibration shifts. The plot on the right also displays a 1D distribution of the plot on the left, providing further evidence that the recovery has been nearly flawless.

### 4.3 Simulation and Data Results of Pi0 Eta Ring by Eta Ring Method

In the scenario where there are not sufficient data to fill each 24,576 sPHENIX EMCal tower, we could still perform the calibrations of the EMCal but in a slightly modified form as discussed in the section 3.7.

The simulation data were acquired using the HIJING<sup>2</sup> event generator. The detector response was simulated employing GEANT4<sup>3</sup>. We used approximately 5 million HIJING  $Au + Au$  events, which generate particles similar to those found in real heavy-ion collisions,

<sup>2</sup> HIJING is a Monte Carlo event generator typically employed in high-energy particle physics simulations based on QCD models. It is designed for the study of jets and particle production in heavy-ion collisions.

<sup>3</sup> GEANT4 is a toolkit for simulating the passage of particles through matter. It is developed in C++ and is extensively used in nuclear and particle physics

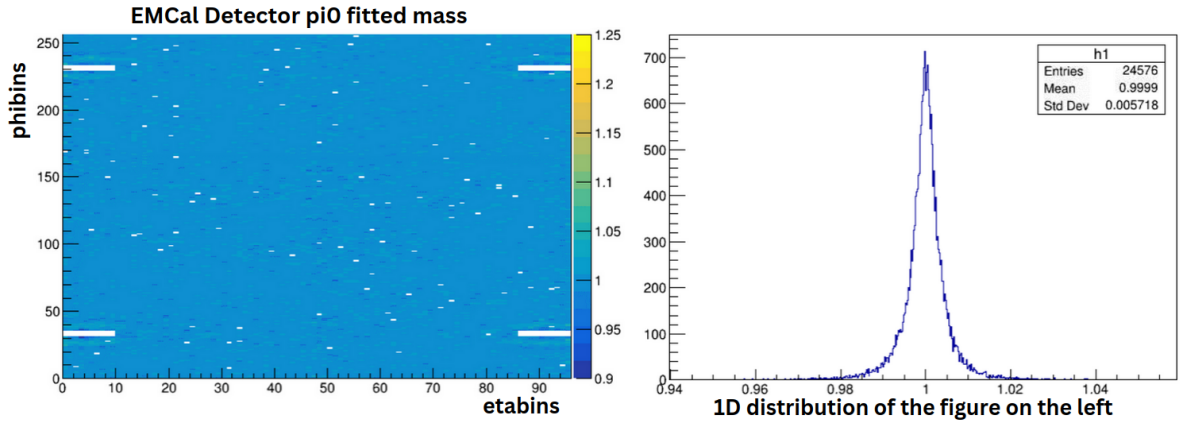


Figure 4.12: Left: The 2D histogram showing how well pi0-tbt method recovered input de-calibration shifts. Right: The 1D distribution of the figure on the left. The value of 1.00 means that the final correction values almost completely recovered the input decalibration.

and these particle responses were recorded using the GEANT4 simulation that mimicked the sPHENIX detectors. Once the data was stored within the sPHENIX framework, we could access it remotely to perform our analysis. We introduced intentional decalibration values, just as we did in the above case of tower-by-tower calibration method, to the pi0 mass of each eta ring of the EMCal, as shown in the top left panel of the figure 4.13. The initial decalibration values caused the mass of pi0 for each eta ring to vary between approximately 0.115 and 0.175 GeV. This initial variation in the pi0 mass provided an ideal ground for testing our method. Figure 4.13 demonstrates the effectiveness of our calibration method, showing that by the sixth iteration, the mean value of the pi0 eta ring converges to our target value of 0.135 GeV, thus confirming that our method functions as intended. The x-axis is the 96 eta ring of the sPHENIX EMCal, and the y-axis represents of the pi0 mass values for each eta ring obtained from the fits.

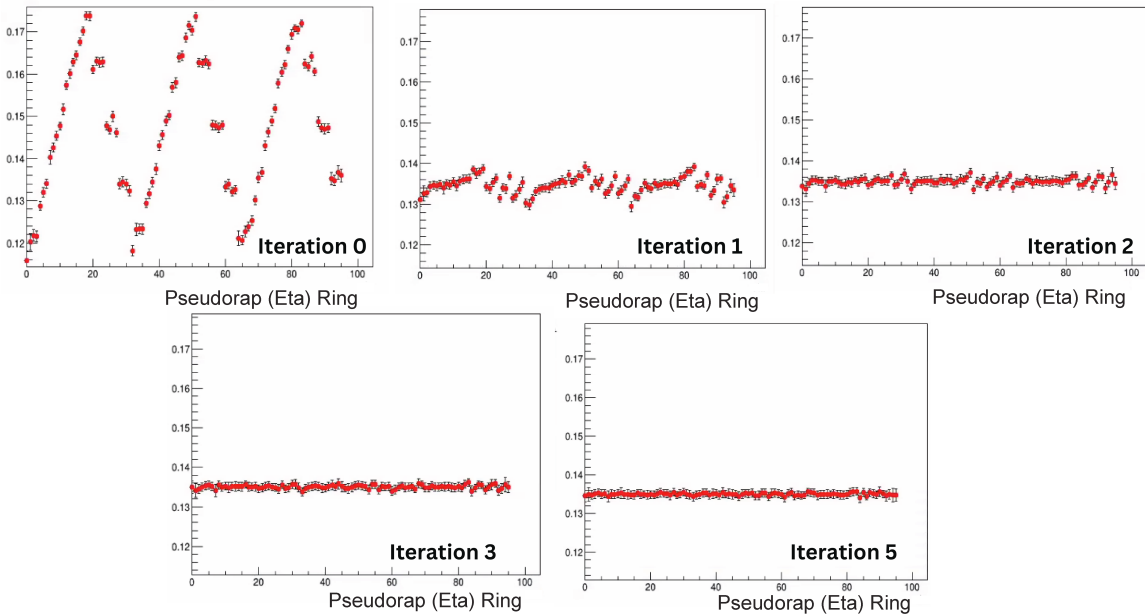


Figure 4.13: Calibration of the sPHENIX EMCAL 96 slices along the  $\eta$  direction using the  $\pi^0$ -calibration method. The x-axis labelled “eta” is actually the etaslices along the  $\eta$  directions of the sPHENIX detector. Each eta slice consists of 256 towers integrated in the  $\phi$  direction embedded into them. This illustrates that the method successfully converges the mean of the  $\pi^0$  for each eta slice to the target value of 0.135 GeV, even within five iterations.

The Figure 4.13 confirms the working condition of our  $\pi^0$  calibration method for the eta ring by eta ring of sPHENIX EMCAL for the data obtained from the simulations. The next obvious thing is to implement the method to the real world datasets.

However, sPHENIX had collected less than expected data for its Run 2023 (Run-23) year due to an unexpected event during the middle of the run period. Current update for Run year 2024 (Run-24) is that the problems have been fixed and data taking is going on strongly. For Run-23, since there were less than expected data, our method of calibrating the sPHENIX EMCAL using eta ring by eta ring came very useful to sPHENIX calorimeter

calibration tasks. Figure 4.14 shows there are way less statistics collected even for each etabin ring. The good thing though, our method didn't fail the fitting of the low statistics histogram pi0 peaks as seen in the figure.

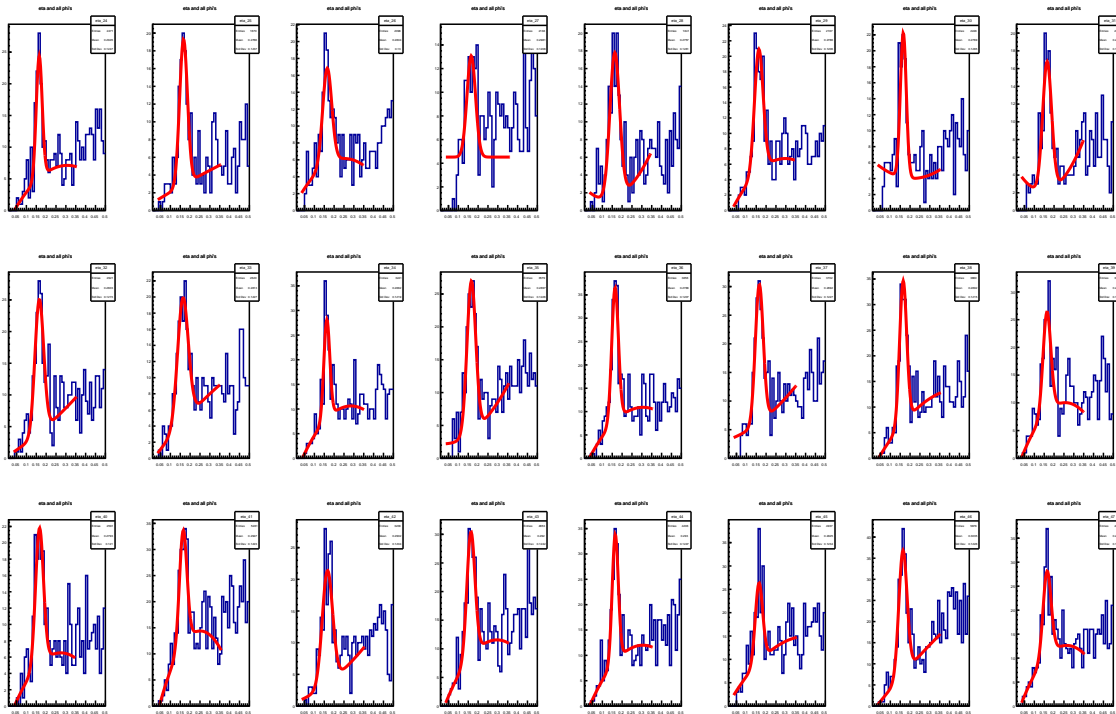


Figure 4.14: Pi0 Peak Fits to Eta bins (2/4th of the expected statistics as indicated by zooming in on the histogram names) for Run 21813. Much less statistics were collected due to a premature end of data-taking during RHIC Run year 2023 because of an accelerator component breaking. Although there were less statistics, the fitting method were able to fit the data without any failure. This also indicates that our method is robust.

The first look at the  $\pi^0$  mass values for each EMCal eta ring is shown in the Figure 4.15 for two example early runs with large enough statistics. Most runs during this period were too small statistics for even this initial calibration method to be applied, since during early commissioning many runs were stopped early—usually each run number is assigned for

the data taking period of about an hour as were these two example runs. The two runs Run 9613 and Run 21813 show example behavior of some of the more extreme non-uniformities present before the calibration is applied, but for which localized deviations of that size were seen in many of the runs that came immediately after these. We can see in Figure 4.15 that the initial values of the  $\pi^0$  fitted mass do not align with the desired value we want. In addition, there are fluctuations of the  $\pi^0$  mass values between the eta ring. Also, it can be seen that there were lots of fluctuations in the  $\pi^0$  mass values initially when the detector was just starting to collect the dataset. It can be attributed to the initial commissioning of the detector components such as the initial onset of radiation damage to the SiPM's which causes a current draw, temperature rises, and a needed adjustment of operating bias voltages. Also for example, the electronics water-based cooling system that cools the SiPM's which have a temperature dependent performance took several weeks to get into a steady state cooling operation at the maximum cooling temperature ( $\sim 0$  degrees Celsius). There is still some variations among the eta rings from the south side and the north side. During this run period, the SiPM bias voltages on the south half of the detector were turned down for testing purposes, while the north half was kept as usual. Despite these rather large imperfections in the initial calibrations, We can correct for this kinds of effects with our  $\pi^0$  calibrations method.

As shown in Figure 4.16, the mass values obtained using the  $\pi^0$  calibration method are 165 MeV, differing from the 135 MeV seen in previous method demonstrations. This does not imply that our method is not working, but instead is a modification we chose to make in the method for this case. To understand this, consider that the  $\pi^0$  calibration method can operate in a “relative” calibration mode. When all towers are corrected to show the same  $\pi^0$  mass peak value (even if not exactly 135 MeV), the final overall calibration can be refined by multiplying all energies from all towers by a single constant, referred to as the “global scale factor”. Hence, if we set the masses to a value of 135+X instead of 135 MeV, the final

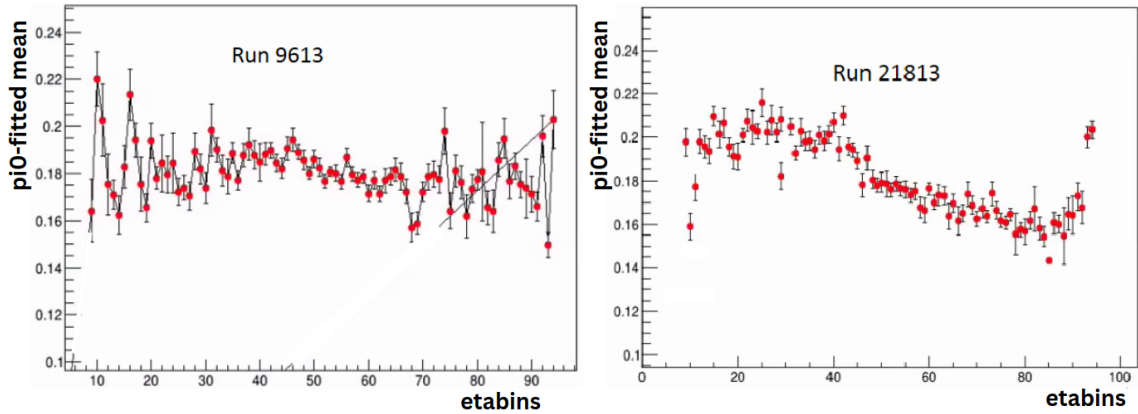


Figure 4.15: First fitting of  $\pi^0$  peak locations at the start of the  $\pi^0$  method steps of the calibration procedure, for runs 9613 and 21813.

global adjustment factor can be determined as  $C_X = \frac{135+X}{135}$ . It was observed in real data that setting the masses in our method to a higher value of 165 MeV is beneficial.

The reason for this is a practical one. As illustrated in any of the previously shown plots of the invariant mass distributions/peak fitting like Figure 4.2, accurately determining the background under the peak, which we do by fitting the background-only region outside the peak area, requires good statistics on both the left and right sides of the peak. However, the left side of the peak has significantly less phase space to populate the left-side background with good statistics, as the background dwindles to 0 as the mass approaches 0 and its range also “compressed” compared to the right-side background. The right-side background area naturally has more phase space, better statistics, and a broader mass range where fitting is feasible, since we can in principle fit as high as the next resonance peak due to the eta meson whose mass peak is at 547 MeV, which gives at least  $\sim 200$  MeV x-range to fit on the right side. Additionally, there are systematic effects due to kinematic selections on the very left side, around  $m = 0$  or just above, that should be avoided in the background-only fit on this side, so that in practice we must start the fit at x-axis mass values  $\gtrsim 40$  MeV, resulting

in a usable fit range more like 70 MeV compared to the  $\sim 200$  MeV range possible on the right side. This left range is also reduced as the relative fluctuations of each tower's calibration within an eta ring increase, which worsens the event-by-event energy resolution and increases smearing, since the  $\pi^0$  peak itself widens since it must be ended before the peak starts.

To alleviate these problems therefore, if we choose a higher mass target value for the method such as 165 MeV, we are effectively artificially stretching out the invariant mass distribution over the whole range, but importantly in this left hand region, giving more room to more precisely select the left region range to include in the background fitting. Then after applying the full method with all iterations having smoothed the eta-ring by eta-ring mass variations, we can just compensate appropriately afterwards by applying the further global adjustment factor, in this case in principle,  $C_{30j} = 165/135$ .

Figure 4.16 shows that our pi0 calibration method is working as intended for the RHIC Run-23 dataset. By the end of fourth iterations, the pi0 mass of all the sPHENIX EMCAL eta ring is converging to the target mass of 165 MeV.

There is one more thing to add which is important to understanding final adjustments to the final EMCAL calibration outside of the scope of our method. This idea is related to the above explanations about our choosing the mass value of 165 MeV in that case, and correcting with a global adjustment factor  $C_X$ . In fact, as it turns out, the true final global correction factor  $C_X$  defined above should not actually be calculated exactly as defined above. The above should be considered a simple definition used for clarity in the above explanations of what is meant by the final global "scale" adjustment factor. The true global adjustment factor  $C_{\text{true}}$  should be defined slightly differently and generally will not be exactly equal to the values described above, even when our method works to accomplish the "relative" eta ring by ring smoothness in the mass value extremely well.

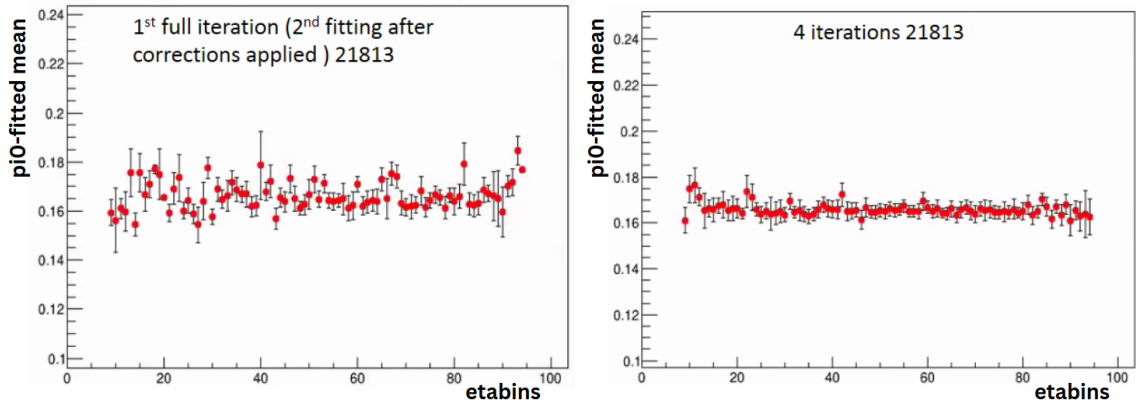


Figure 4.16: Fitting after indicated number of iterations demonstrating readjustment of the  $\pi^0$  peak locations (gaus fit means) from the method converging to the value of the 165 MeV input which in this case was chosen as the target mass value instead of 135 MeV for reasons explained in the text.

Instead, there are several possible additional effects when determining the actual  $C_{\text{true}}$  factor. These effects which affect the  $C_{\text{true}}$  include systematic effects of the fitting of our method, potentially any bias effects due to our GEANT simulation not perfectly matching the real actual situations (and hence our test results having small errors which we need to address), and non-linearity of the energy response of the EMcal towers. The non-linearity effect arises because in our method, we are fixing the calibration at a very small value of energy (at  $\pi^0$  momenta around 1.5 GeV, which implies at even lower photon energies) whereas the place in energy where we are most interested in having the calibration to be most correct will actually be in the range of 25-50 GeV where the most important full jet reconstruction physics sPHENIX is targeting lies in energy. Thus, a non-linear response means that  $C_{\text{true}}$  should in actuality have a small energy dependence which would result in extra factor compared to the simple formulae given previously such as  $C_X$ . Even more numerically larger than all these effects however for determining the global  $C_{\text{true}}$  calibration

adjustment factor in this case, is a simpler effect that is due to a combination of energy smearing, the RHIC spectral shape, and the finite energy/momenta binning/ momentum cut selections of our method. This effect works as follows. First recall that finite energy resolution means that true photon energies get "smeared" with photon by photon fluctuations with gaussian-like distributions, generally with measured final photon energies including many cases of both higher energies than the true energy and lower than the true energy ("smeared up" and "smeared down").

Because energy and invariant mass are perfectly functionally correlated as shown in Equation 3.2, a minimum  $E/p/p_T$  cut (or any momentum bin selection) results in unequal effects for energy smearing in the upward *vs.* the downward directions leading to a net shift in the expected mass peak values, even when the on-average energy calibration is perfect. This shift depends on the underlying spectra shape and the details of the cut or binning selections.

For example, a simple minimum  $p_T$  (or  $p$  or  $E$ ) cut like we employ will result in an excess of upward smears into the cut selection region (greater than the threshold). This is because for true energies below the cut value, smears down are still lost by the cut, but some smears up will then pass the cut and thus are kept. Also there will be an excess of downward smears "lost" below the minimal cut selection for similar reasons. Either an excess of upward smears, or a net reduction in downward smears, will both will cause net shifts upwards in the expected fitted mass peak mass values. This effect is a well known effect in PHENIX where these "shift" effects are known to be on the order of several MeV upward shifts above the PDG mass value.

The exact shift size therefore depends on the underlying truth spectral shape near the minimum cut thresholds, or more generally near the edges of any momentum bin values. RHIC's basic soft hadron physics (such as thermal production due to the QGP) implies all produced particles including the photons and  $\pi^0$ 's we are using in our method,

will follow a very steeply-falling spectral shape, where the number of produced particles reduces by roughly an order of magnitude for every  $\sim 500$  MeV we increase the energy of the particles we use. Because of this extreme “fall-off”, the exact upward shift must be carefully calculated assuming a realistic spectral shape. Thus, applying the results of such a calculation for this effect must also be included in order to obtain the correct  $C_{\text{true}}$  value for our case.

As described in the beginning of Chapter 3 we are really talking here about the final adjustments which will define the final absolute calibration. For all of these kind of final adjustments, sPHENIX employs many other calibration methods and observables, including electron tracking vs electron calorimeter observable comparisons, eta meson calorimetric observables, and prompt-photon jet transverse momentum balance, amongst other observables, to do the final “fixing” of the  $C_{\text{true}}$  value. We call this process of determination of the final global adjustment factor ( $C_{\text{true}}$ ) “fixing of the final EM energy scale” and is beyond the scope of our calibration method.

## 5 PHENIX AuAu 2PC ANALYSIS: DATA PREPARATIONS AND ANALYSIS

For the remainder of the dissertation we discuss my second dissertation topic, the PHENIX analysis of Au+Au two-particle correlations analysis.

### 5.1 Introduction and Motivation

In the Introduction section 1.6.1.2, we briefly discussed the two-particle correlation method that we will employ. This method helps to quantify the extent of jet suppression due to QGP matter. Relativistic Heavy Ion (RHI) collisions with significant overlap, the most central events as described in section 2.2.7, tend to produce a large number of final-state particles and are likely to have QGP formation. In contrast, collisions with minimal overlap, known as peripheral collisions, generate fewer final-state particles, making QGP formation not certain. The latter is similar to the situation for small colliding Ion systems such d+Au,  $^3\text{He}+\text{Au}$  or p+A generally. At the same time this uncertainty about QGP in peripheral A+A and small systems has become one of the most important questions in the field of RHI because it relates to the fundamental question of emergent effects of the basic strong force QCD theory—specifically how are quarks and gluons formed from vaccuum with large occupation numbers and high energy density [45].

My focus is on analyzing two collision regions: central collisions denoted with 20-40% centrality and peripheral collisions denoted with 65-70% centrality for the Au+Au collision system. The purpose is to address the questions about QGP formation in peripheral A+A and small collision systems. The reason for focusing on these two specific centrality ranges is because they are meant to be complementary to a previous set of results already briefly mentionned in the Introduction, and eventually even published together with them. So let me first summarize this previous set of results.

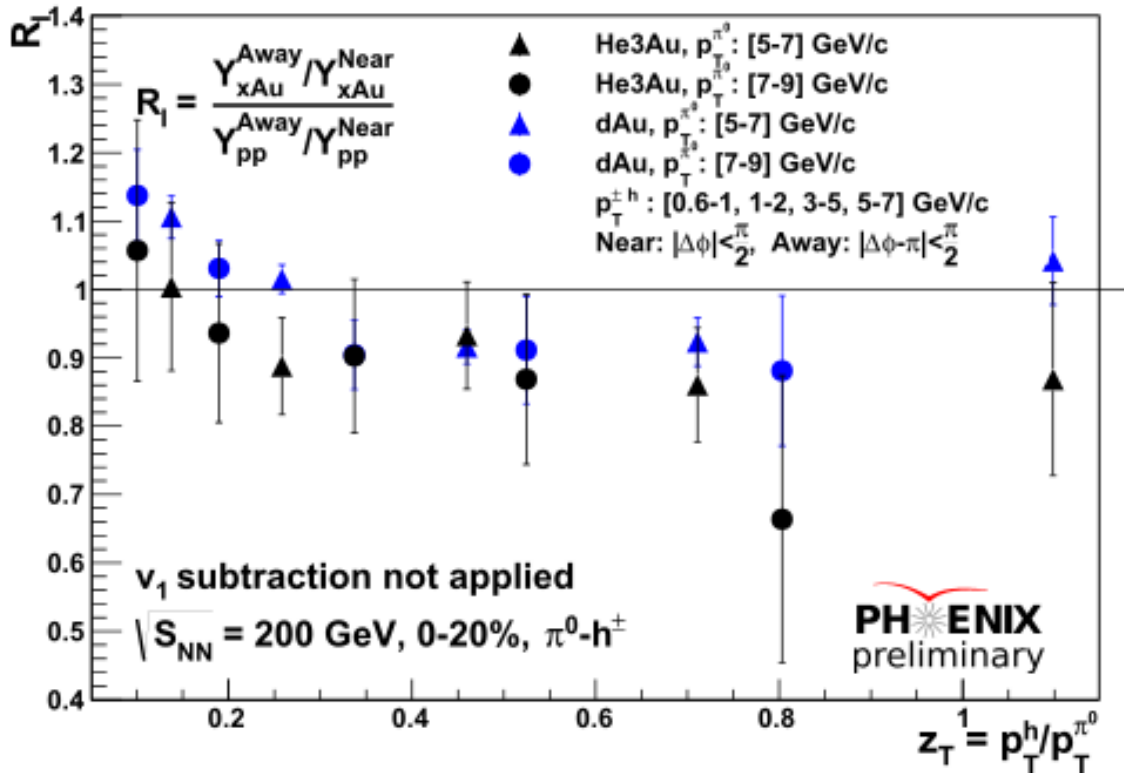


Figure 5.1: Comparing  $R_I$  observable between d+Au and  ${}^3\text{He}+\text{Au}$  collision systems from PHENIX experiment [1]. The two systems demonstrate the dependence of QGP formation that scales with system sizes, with larger systems exhibiting greater suppression due to the formation of a larger QGP (medium) as compared to the smaller system.

The main result in these previous results we are interested in pursuing is demonstrated in Figure 5.1. This result shows a new observable  $R_I$  which was first introduced in these previous works, for two small systems, d+Au by analyzed by Bing Xia and  ${}^3\text{He}+\text{Au}$  analyzed by Abinash Pun, two previous Ph.D. students from our same research group. As will be discussed below in section 5.4.3.2, a value less than 1 of the observable  $R_I$  especially on the right hand side of the plot (those corresponding to higher particle momentum as defined by the variable plotted on the x-axis,  $z_T$  which will be defined 5.4.3.1) could imply

jet suppression due to QGP formation. However the size of the suppression is small, about 15% (since  $R_I \approx 0.85$ ) and there are also other nuclear effects that could cause these size modifications. Further it needs demonstrated that the new observable used  $R_I$  can be trusted to properly quantify suppression by using it to reproduce a previously measured suppression level.

Now it is easy to understand our motivation for the two centrality ranges in A+A. The purpose of studying the 20-40% centrality range is to validate our analysis method and the observable  $R_I$  by comparing our results with other published data on similar systems and centralities but different observables. This 20-40% range is well studied in the traditional jet suppression observables and is known to have a large suppression effect due to QGP formation.

The objective of examining the 65-70% centrality range is to determine whether QGP effects can be detected in such peripheral collisions, which involve a similar number of participating nucleons as other small collision systems such as d + Au and He<sup>3</sup> + Au. We chose our centrality bin of 65-70% directly because it had a similar  $N_{\text{participant}}$  number ( $\approx 22$ ) to the central result of 0-20% <sup>3</sup>He+Au as shown in Table 5.1. So, it is good to directly compare the results we obtained quantitatively with those of <sup>3</sup>He+Au as an example of how much suppression the new result could be reasonably consistent with.

## 5.2 Datasets and Preparations

Before starting any data analysis, the initial task is to acquire and clean the data. Over the years, PHENIX has gathered large datasets, with the largest collections from 2014 and 2016. We will utilize the Au+Au collision datasets from Run-14 (Run year 2014) and Run-16, and using the p+p collision data from 2015 as the baseline. PHENIX stopped data-taking in 2016, so the datasets to be used were already collected between 2014 and

Table 5.1: Comparing the number of participants for various systems [1].

Collision Species	Centrality %	Number of Participants
d+Au	0-20	16.26
$^3\text{He}+\text{Au}$	0-20	22.497
Au+Au	20-40	140.03
	50-55	53.16
	55-60	40.96
	60-65	30.77
	65-70	22.64
	70-75	16.17
	75-80	11.15
	80-93	5.60

2016, and stored at BNL’s SDCC<sup>4</sup> facility. But a larger number of events is available than is best to use for our particular analysis, so we must apply quality checks on which files and runs of data amongst the larger datasets should be used in order to ensure its alignment with the objectives of this thesis; the subsequent step involves conducting the actual analyses, making plots, and drawing conclusions. Here I will describe various steps and processes that I took in order to make the final plots for the thesis.

In addition to quality cuts on the data, to select the necessary particles for the two-particle correlation analysis, various selection criteria or thresholds, commonly called “cuts” in this thesis, are employed. These cuts are designed primarily to eliminate significant amounts of background from being considered as signal data, which is essential for this thesis, or any study for that matter. The kind of analysis that we are performing has already

---

<sup>4</sup> Scientific Data and Computing Center located at Brookhaven National Laboratory

been accomplished on PHENIX many times, so the majority of the cuts specifications used in this analysis have already been established, for example [16], [1].

### 5.2.1 Data Selections

The data used in this study is obtained from the PHENIX experiment conducted in Run-14 and Run-16, which correspond to the years 2014 and 2016. Within Run-14, various collision species were performed, but our focus is specifically on the collision species AuAu. Furthermore, we are only interested in analyzing two centrality classes of the AuAu collisions, namely 20-40% and 65-70%. In addition to the AuAu data, we also require reference data from pp collisions, which will be obtained from the Run-15 data, corresponding to the year 2015. Table 5.2 shows more information on the data selected for this thesis.

Table 5.2: PHENIX Data selected for this thesis analysis.

Run Year	Beam Species	Beam Energy $\sqrt{S_{NN}}$	Integrated Luminosity
2014	AuAu	200 GeV	$7.5 \text{ pb}^{-1}$
2015	pp	200 GeV	$382 \text{ pb}^{-1}$
2016	AuAu	200 GeV	$4.0 \text{ pb}^{-1}$

### 5.2.2 Run Selections

Every data-taking session (called a "run" of the data acquisition system), which lasts approximately an hour, involves recording collisions. Throughout the run, issues with the detector may arise, resulting in the entire set of data from that session being discarded. To ensure the quality of each session, a series of Quality Assurance (QA) tests must be performed. It also ensures that if there were any issues with the detectors or parts of the

detectors during those runs, then they would be removed. Afterward, a list of all successful runs, called “good runs list”, is compiled for the use of all the collaboration who want to perform their own data analysis. In the case of the Run-14 AuAu dataset, the good run lists were obtained from Anthony’s Ph.D. thesis [16]. For Run-15  $pp$  data, the run lists were determined by an analysis by Abinash Pun’s [1].

### 5.2.3 Event Selections

The minimum bias events are events in which the selection criteria have been set to minimal requirements. The MinBias (MB) event is selected when the absolute value of the z-vertex is less than 10 cm from the detector center ( $z=0$ ) and when it falls within the desired centrality classes, specifically 20-40% and 65-70% for the objectives of this thesis. The criterion for having a z-vertex below 10 cm is due to the fact that in the years the data was taken, the PHENIX detector was optimized for data in this range, and the largest fraction of MB events typically occur within this narrower z-vertex range.

### 5.2.4 Particle Selections With Various Cuts

This thesis examines the relationship between two particles, specifically  $\pi^0$  and charged hadrons ( $h^\pm$ ) related via the same collision events. These particles are chosen as triggers and partner particles. The ideal trigger particle should have minimal interaction with the medium and exit the medium with minimal loss of energy or momentum. Direct photons meet these criteria, but their statistics are limited in the PHENIX experiment. This is one of the reasons why the sPHENIX experiment was initiated to address the limited acceptance issues of PHENIX and provide us with higher statistics. Since there is a significant production of  $\pi^0$ , low statistics are not a concern. Furthermore, higher-energy  $\pi^0$  particles are selected to select particles from jet production. The properties of the  $\pi^0$  particles are well understood and can be detected accurately by the PHENIX EMCal with good resolutions. Therefore,  $\pi^0$  is a logical choice as the trigger particle. For the partner particles, charged hadrons with

lower  $p_T$  are chosen to reduce noise and enhance resolutions. The PHENIX tracking system which is more precise than the EMcal at low energies, is used to detect and characterize these charged hadrons.

The particles detected by the detector are not the  $\pi^0$  directly, but the final-state decay particles associated with  $\pi^0$ , that is, two daughter photons. We have to reconstruct  $\pi^0$  considering the two decay photons that originate from it. Consequently, we must choose photons that are the actual daughters of the same  $\pi^0$  trigger. In order to minimize noise and backgrounds, various criteria for selecting these photons are implemented. Some of the criteria to select photons and charged hadrons are briefly described below;

#### 5.2.4.1 Shower Shape Cut: $\chi^2 < 3$

The photons that interact with the EMCAL are responsible for creating clusters, which are groups of towers hit in the detector. However, electrons and positrons can also create clusters and occasionally other hadrons can too, so it is important to be able to distinguish between clusters formed by photons and those formed by other particles. Although the EMCAL is designed to primarily detect electromagnetic showers (which can be thought of as clusters), it is possible for some hadrons to be stopped by the EMCAL and form hadronic showers. Fortunately, the shapes of these clusters (showers) have distinct characteristics that differentiate them from each other. By applying shower shape cuts, we can select most of the photon clusters (showers). The specific shower shape cut used is  $\chi^2 < 3$ , where  $\chi^2$  is defined as follows:

$$\chi^2 = \sum_i \frac{E_i^{pred} - E_i^{meas}}{\sigma_i^2} \quad (5.1)$$

#### 5.2.4.2 Charged Hadron Veto: $r_{emc-pc3}^{veto} < 8.0 \text{ cm}$

Although the removal of hadron clusters through the shower shape cut allows us to select photon clusters, there is still a significant presence of hadron cluster contamination.

To further mitigate this contamination in the photon selections, we incorporate a charged-hadron veto cut. The concept behind this approach is to examine the nearby charged hadron tracks either from the tracking system without the PC3 included, or including the PC3, or sometimes only considering the PC3, the clusters are checked to see if a charged track could've caused this cluster. For example if PC3 hits which are located 5 cm away from the EMCal cluster we are considering are found we may "veto" this cluster. If the distance between the cluster and the tracks is close, we reject that cluster as it may actually be a track.

#### 5.2.4.3 Further Single-Photon Selection Criteria

The energy of either of the two pi0 photons should be at least of 1 GeV at a minimum. The range of  $p_T$  for leading (higher energy) photon in a pi0 pair is set to  $4 \leq p_T \leq 20$  GeV/c. Additionally, the Hot/Dead towers in the EMCal, which are towers that inaccurately record high/low gains, need to be eliminated. Also, the clusters near the bad towers and at the edges of the EMCal are rejected to ensure proper energy containment of the clusters.

#### 5.2.4.4 Cuts on the $\pi^0$ Triggers

Once the implementation of the photon cuts is completed, the reconstruction process of  $\pi^0$  is performed using the pairs of the cluster photons. Several cuts are applied to the reconstructed  $\pi^0$  particles (photon pairs). Some of these cuts are provided below:

- The transverse momentum ( $p_T$ ) of the  $\pi^0$  is limited to the range of 4 to 17 GeV/c. The upper limit is imposed because at higher energies, the two photons from the  $\pi^0$  can merge together and cannot be distinguished for reconstruction.
- The invariant mass ( $m_{inv}$ ) of the  $\pi^0$  is restricted to the range of 0.12 to 0.16 GeV/c<sup>2</sup>. This range accounts for the resolution limitations of the EMCAL detector and includes the smearing effect caused by the detector. The invariant mass is calculated using the

two photons as follows:

$$m_{\gamma_1\gamma_2} = \sqrt{2E_{\gamma_1}E_{\gamma_2}(1 - \cos(\phi_{12}))} \quad (5.2)$$

where  $\phi_{12}$  is the opening angle between the two photons, and  $E_{\gamma_1}$  and  $E_{\gamma_2}$  are the energies of the two photons, respectively.

- For the reconstruction of  $\pi^0$ , both photons should be detected in the same arm of the detector.
- The energy of  $\pi^0$  should be greater than or equal to 4 GeV.
- The asymmetry cut is used primarily in central AuAu collisions to reduce the background from random combinations of photons.

The asymmetry cut is given by  $\alpha \leq 0.15 + 0.85 \left[ \frac{E_{\pi^0} - 4}{1.25} \right]^2$ , where  $\alpha$  is defined as:

$$\alpha = \frac{E_{\gamma_1} - E_{\gamma_2}}{E_{\gamma_1} + E_{\gamma_2}}$$

#### 5.2.4.5 Cuts on the Charged Hadrons

The DC and PC detectors are primarily used to track charged hadrons. In order to be eligible for this analysis, these charged hadrons must meet certain criteria. Specifically, they must have hits on PC1 and be visible in the drift chambers. The following are some of the specific cuts applied to these charged hadrons:

- The transverse momentum ( $p_T$ ) should be between 0.5 and 10 GeV/c
- The quality of the track (a measure of the high probabilities that it is a true track already implemented in the coding framework) should have the value of 63 or 31. The 63 is being considered the highest quality tracks and 31 as the second highest quality tracks.

- The RICH is used to veto electrons from the list of tracks
- The tracks recorded in PC1 and DC chambers are projected onto PC3 for the PC3 and EMCal matching cuts. The signalized distance between the PC1/DC point and the EMCal is used to remove false tracks with high momentum. The signalized distance should be as  $\sqrt{\sigma_\phi^2 + \sigma_z^2} \leq 2$  in order to be considered as the true charge hadrons

The track matching cut can be described as follows: the tracks reconstructed using DC and PC1 hits are projected onto PC3. The projected point on PC3 should correspond to a nearby PC3 hit. This criterion ensures that the tracks were indeed formed in DC and PC1, as confirmed by their alignment with PC3. The same principle applies to the matching of PC3 and EMCal.

Since charge tracks also leave "MIP" hits in the EMCal, it can also be used for track matching. Sometimes, both EMCal and PC3 can be combined for track matching. The elliptical or radial PC3 matching cut combined with EMCal is a technique used to eliminate especially the high- $p_T$  incorrectly reconstructed electrons that are located towards the edges of the detector. This is necessary because the RICH (Ring Imaging Cherenkov) detector may not be able to remove all of these electrons, especially when trying to identify charged hadrons. The cut involves measuring the distance of charged particles from the DC (Drift Chamber) and PC1 (Pre-shower Calorimeter) and projecting this distance onto PC3 or EMCal. We use the PC3 and EMCal (Electromagnetic Calorimeter) information to veto these charged hadrons using the following equations;

$$r_{emc-pc3}^{veto} = \sqrt{dx_{emc-pc3}^2 + dy_{emc-pc3}^2 + dz_{emc-pc3}^2} \quad (5.3)$$

where the charged hadrons with  $r_{emc-pc3}^{veto} < 8$  cm are rejected for the new results of this thesis.

### 5.3 Validating Our Selection Cuts With Previous Work

After any data set analysis is performed and plots begin to emerge, it is natural to question whether the methods and selection criteria used were correct. A useful way to validate your plots or results is to compare them with previously completed and published analysis, if available. In our case, we can compare our Run-14 Au+Au collision with 20-40% centrality analysis to an already published result that had the same run year and centrality system but used a different jet quenching observable [16]. This comparison is shown in Figure 5.2. Both plots are derived from the total datasets that come right after the PHENIX taxi jobs without applying any detector efficiency corrections or subdivisions into smaller bins based on  $p_T$  of the trigger or partner particles. The similar patterns observed in both plots confirm that our analysis is functioning correctly.

### 5.4 RI-Related Analysis Details

#### 5.4.1 *Detector Corrections*

The unique shape of the PHENIX detector makes a limited acceptance to the collision particles to be detected, which requires corrections to the collected data. To address this limitation, a technique called event mixing is used, which is described in more detail below. One of the benefits of using  $R_l$  observable is that it eliminates the need for efficiency corrections for the tracking system and any detected particles. Since there is no detector before the Drift Chambers, any physical processes occurring prior to reaching the DC remain less certain. For example, conversion electrons ( $\gamma + \gamma \rightarrow e^+ + e^-$ ) that do not originate from the primary collision events. Another example is the creation of secondary particles from the decay of primary particles, which is crucial to calculate the efficiency of charged hadrons. Tracking detectors such as the DC and PC trace the movement of charged hadrons. Ideally, all charged hadrons produced at the collision vertex would be immediately detected by the innermost tracking detector. However, certain processes, such as the generation of

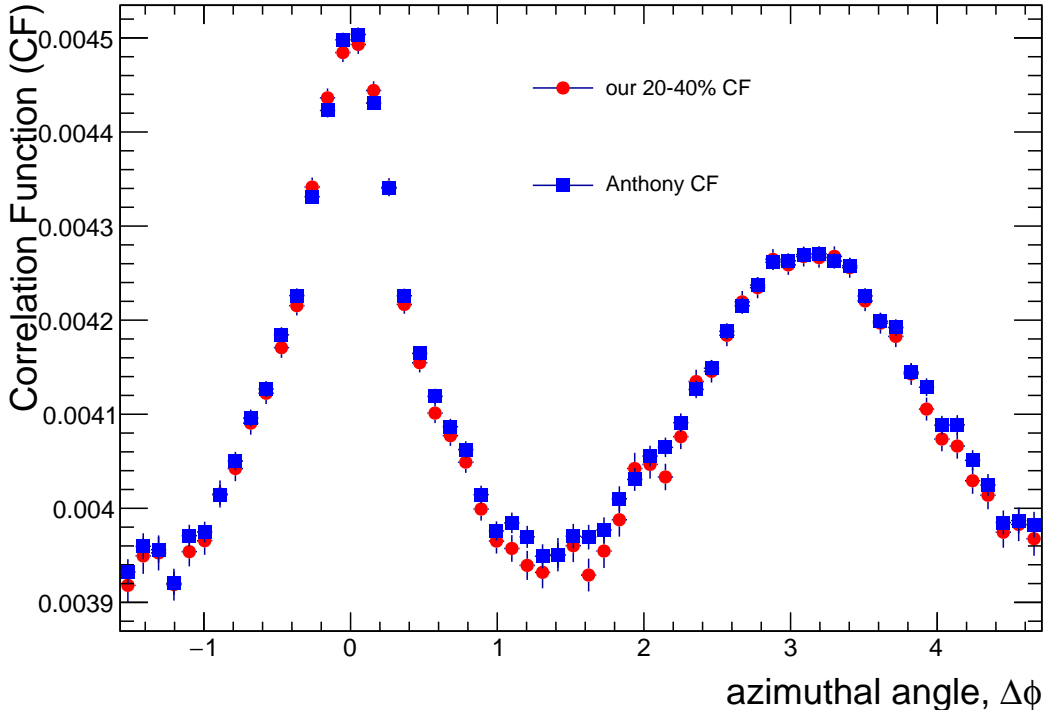


Figure 5.2: Comparisons of the total correlation functions between our dataset with Run-14 Au+Au with 20-40% centrality and Anthony Hodges [16] same run year with same centrality analysis result. The similar structures of the correlation function verifies our selection cuts and the analysis methods are working as expected.

conversion electrons ( $\gamma + \gamma \rightarrow e^+ + e^-$ ), multiple decays of particles with errors in the original vertex, and weak decays of short-lived particles like  $K_S^0$ ,  $\Lambda$ , and  $\bar{\Lambda}$ , can reduce the tracking efficiency before reaching the innermost detectors. Not to mention dead areas and intrinsic inefficiencies of the detectors. The use of the  $R_I$  observable alleviates concerns about detector efficiency issues.

### 5.4.2 Two Particle Correlations

In particle collisions involving hard scattering, two partons that are scattered in opposite directions form two jets. Jets that appear close to the system's surface undergo relatively less alteration compared to the jet that passes through the dense medium. Figure 5.3 illustrates the trigger and partner particles originating from the hard-scattered events.

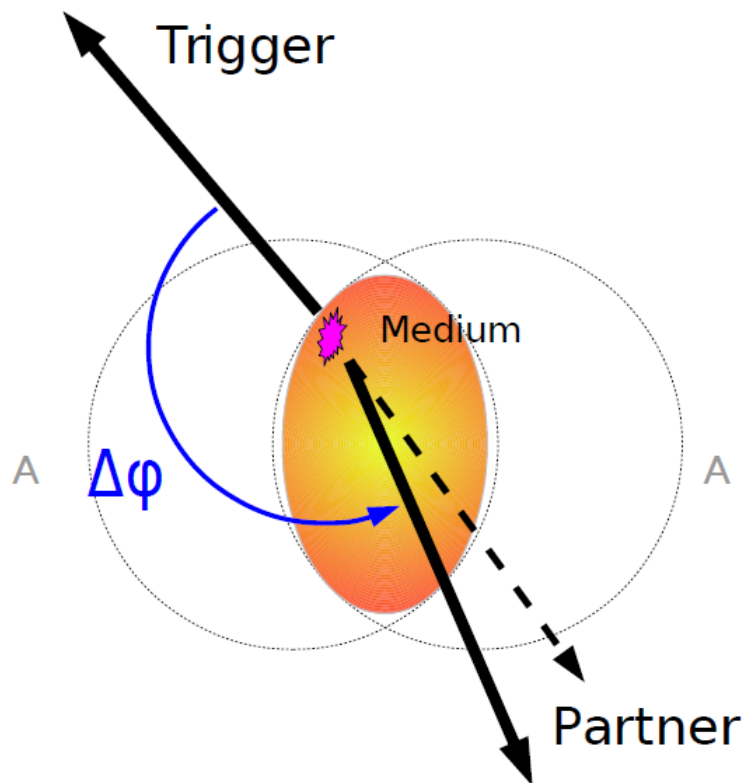


Figure 5.3: Illustration of the two particle correlation study [1].

The two-particle correlation study focuses on selecting two particles that are related through the same physical processes in a given event. One of these particles, called the “trigger” (in this case,  $\pi^0$ ), is of high transverse momentum ( $p_T$ ), while the distribution of the other particles (called the “partner” particles) is examined as a function of the difference

in azimuthal angle ( $\Delta\phi$ ) and pseudorapidity ( $\Delta\eta$ ) between the two particles. Due to limited acceptance in the pseudorapidity region, this thesis specifically investigates two-particle correlations as a function of the azimuthal angular difference only. The trigger particles are selected from the jet with higher transverse momentum, while the partner particles are chosen from the jet that traverses through an evolving dense medium. If both the trigger and partner particles are taken from the same jet, it is termed the “near-side” jet, which exhibits a Gaussian-like distribution around  $\Delta\phi \sim 0$ . On the other hand, if the trigger and partner particles are selected from jets on opposite sides, it is called the “away-side” jet, which results in Gaussian-like distributions around  $\Delta\phi \sim \pi$ .

An overview of the flow has already been discussed in Section 1.6.1. Although our aim is to investigate QGP through jet correlations, the two-particle analysis, which is our primary method of study, also produces results influenced by flow. In this study, flow is treated as a background effect and must be subtracted.

Due to the limited acceptance of PHENIX as mentioned previously, which is inherent to its unique design, a method is employed to address this limitation. This involves generating mixed events by combining triggers from one event with partners from another event. It is important to ensure that the two mixing events are not significantly different from each other in terms of their z-vertex of the collisions and centralities, with only small (about 5%) differences allowed. By calculating the ratio of the same-event distributions to the mixed-event distributions, the effects of limited azimuthal acceptance from the detector are minimized. Consequently, the correlation function can be expressed as being proportional to this ratio as;

$$C(\Delta\phi) \propto \frac{N_{\text{same}}^{AB}(\Delta\phi)}{N_{\text{mixed}}^{AB}(\Delta\phi)} \quad (5.4)$$

where  $N_{\text{same}}^{AB}$  is the total trigger ( $A$ )-partner ( $B$ ) pair from the same events, while  $N_{\text{mixed}}^{AB}$  is from mixed events.

The two-particle correlation offers the advantage of being able to distinguish the correlation distribution because of the effects of jets and flow. The two-source model suggests that the distribution of same-event particle pairs is a result of two components: the pairs from jets produced by hard-scattered partons, and the pairs from the background combinatorial production of particles with anisotropic flow relative to the reaction plane. Therefore, it is possible to separate the total distributions into these two components. Therefore, the total correlation can be written as;

$$\frac{dn_{\text{same}}^{AB}}{d\Delta\phi} = \frac{dn_{\text{jet}}^{AB}}{d\Delta\phi} + \frac{dn_{\text{comb}}^{AB}}{d\Delta\phi} \quad (5.5)$$

where  $n$  represents the particle productions per event. The combinatorial background term is given by;

$$\frac{dn_{\text{comb}}^{AB}}{d\Delta\phi} \propto \left[ 1 + \sum_{n=1}^{\infty} \langle 2v_n^A v_n^B \rangle \cos(n\Delta\phi_{AB}) \right] \quad (5.6)$$

where  $v_n$ 's are the flow coefficients.  $v_2$  corresponds to the elliptic flow contributions,  $v_3$  to the triangular flow, and so on. In this thesis, flow coefficients upto fourth order is used. With some mathematical substitutions, Equation 5.5 becomes;

$$C(\Delta\phi_{AB}) = J(\Delta\phi_{AB}) + b_0 \left[ 1 + \sum_{n=1}^{\infty} \langle 2v_n^A v_n^B \rangle \cos(n\Delta\phi_{AB}) \right] \quad (5.7)$$

The function  $J(\Delta\phi_{AB})$  represents the jet function, which includes only the contributions of the jet pairs in the correlation function. The additional term in Equation 5.7 arises from the particle flow and is described by Fourier analysis. The parameter  $b_0$  represents the level of combinatorial background, which is used to normalize the combinatorial pairs in the correlation function. The background level is determined using methods such as Zero Yield At Minimum (ZYAM) described next.

To determine the background level, we have utilized a technique known as Zero Yield At Minimum (ZYAM). This technique presumes that there exists a region in the correlation function distribution where the jet correlations reach their minimum, which occurs approximately at  $\Delta\phi = \pi/2$ . Additionally, ZYAM assumes that the correlation function distribution is mainly formed by the two components: one from the jets correlations and the other from the background flow correlations. The background level  $b_0$  according to ZYAM is given by the following equation:

$$b_0 = \frac{\langle n_{bg}^{AB} \rangle}{\langle n_{same}^{AB} \rangle}$$

### 5.4.3 Jet Pair Quantification

Some of the observables of jet quenching are described in the introduction chapter. Here we discuss two more observables which are also used quite commonly in the literature.

#### 5.4.3.1 $I_{AA}$

In heavy-ion collisions, there are various experimental quantities that can be employed to measure the effects of QGP on the jets. One of these observables is the nuclear modification factor, denoted as  $I_{AA}$ , which integrates the per-trigger yield over  $\Delta\phi$ . This factor is used to assess the changes in jets by comparing the yields in AA collisions with those in pp collisions. The mathematical definition of  $I_{AA}$  is as follows:

$$I_{AA} = \frac{Y^{AA}}{Y^{pp}} = \frac{\int_{\Delta\phi_1}^{\Delta\phi_2} \left( \frac{1}{n_A} \frac{dn^{AB}}{d\Delta\phi} \right)_{AA} d\Delta\phi}{\int_{\Delta\phi_1}^{\Delta\phi_2} \left( \frac{1}{n_A} \frac{dn^{AB}}{d\Delta\phi} \right)_{pp} d\Delta\phi} \quad (5.8)$$

The integral  $I_{AA}$  can be calculated either on the near-side or the away-side, depending on the range of integration. In the case of  $I_{AA}$ , a scaling factor such as needed for  $R_{AA}$  is not necessary because the ratio is the same for the per-trigger yield in both the numerator and denominator. If there is no formation of the dense medium known as the Quark-Gluon

Plasma (QGP), then the jets are not expected to be modified, and therefore the same amount of yields per-trigger is anticipated in both systems. This implies that the ratio is expected to be close to unity for cases where no QGP formation occurs. Any deviation of  $I_{AA}$  from unity indicates the formation of a dense medium like the QGP and hence the modification of the jets. The typical behavior observed is that in large collision systems like AA, the away-side  $I_{AA}$  deviates from unity, indicating the suppression or quenching of the jets.  $I_{AA}$  is usually plotted with respect to  $z_T$ , which is defined as follows:

$$z_T \equiv \frac{p_T^{partner}}{p_T^{trigger}} \quad (5.9)$$

Even though no scaling is needed for  $I_{AA}$  its value depends strongly on the efficiency of the charge particle measurements, since a large inefficiency in a certain data set will generally result in less per-trigger yield.

#### 5.4.3.2 $R_I$

$R_I$  is also an observable that can quantify the modifications of the jets resulting from the effects of QGP. It is called the double ratio, which involves dividing the yield of the away-side peak from the AA collisions by the yield of its nearside peak first and then dividing the result by the ratio of the away-side yield from the  $pp$  collision to its near-side peak. The Ohio University group, in Bing Xia's Ph.D. thesis [26], was the first to utilize the  $R_I$  observable. Since the ratio is calculated within the same system before being compared to another system,  $R_I$  tends to mitigate numerous systematic errors that originate both within and outside the system.  $R_I$  is defined in Equation 5.10

$$R_I \equiv \frac{Y_{away}^{AA}/Y_{near}^{AA}}{Y_{away}^{pp}/Y_{near}^{pp}} \quad (5.10)$$

There are several benefits of using  $R_I$  as an observable to quantify the jet suppressions in the  $AuAu$  collision events, especially the peripheral centrality collisions, where the effect

of QGP, if formed, is minimal on the jets. Most of the benefits include dividing out the systematical errors from the system when taking the ratio of away-side to near-side of the same system before comparing with the baseline system. Let us briefly discuss the benefits of using  $R_I$  below:

**No Need to Include Single Particle Hadron Efficiency** The single particle detection efficiency poses a significant challenge for  $I_{AA}$ , but this is not the case for  $R_I$ . Since we initially compare the away-side to the near-side system, the single-particle efficiency is consistent on both sides and gets canceled away. This cancels out any efficiency-related issues in hadron detection. On the other hand, the efficiency of the trigger particles is taken into account when calculating the yields using per trigger yield, ensuring that it does not affect the results.

**Low Sensitivity to the ZYAM Normalization** The contribution of the background level  $b_0$  from the ZYAM level is equal for both the near-side and away-side peaks of the correlation functions. Therefore, when calculating the ratio, systematic errors caused by  $b_0$  have no significant impact on  $R_I$  compared to  $I_{AA}$ .

#### 5.4.3.3 Corrections Performed to $R_I$ Observable

Some of the corrections that are applied to  $R_I$  observable are discussed below:

**Rapidity Acceptance Correction** The PHENIX experiment has a distinctive shape that has some disadvantages due to its limited acceptances in the  $\eta$  and  $\phi$  directions. The acceptance correction in  $\phi$  is achieved primarily through the event mixing technique, which generates the background for the correlation functions. This background is then subtracted from the foreground correlation functions to eliminate acceptance issues  $\phi$ . On the other hand, the correction for  $\eta$  acceptance is based on ensuring that the angular jet width is the same in both the  $\Delta\eta$  and  $\Delta\phi$  directions. The correction factor for the near-side can be obtained using Equation 5.11 [23];

$$R_{\Delta\eta} = \frac{1}{\frac{1}{\sqrt{2\pi\sigma_N^2}} \int_{-0.7}^0 .7 \exp\left(-\frac{\Delta\eta}{2\sigma_N^2}\right) acc(\Delta\eta) d\Delta\eta} \quad (5.11)$$

where  $acc(\Delta\eta) = (0.7 - |\Delta\eta|)/0.7$  is the PHENIX pair acceptance function in  $\Delta\eta$  obtained by convoluting two flat distributions in  $|\Delta\eta| < 0.35$ . The resulting  $acc(\Delta\eta)$  function is then the triangular shape which is what we see in the correlation function plots in the results. The away-side correction factor, on the other hand, is a constant value, which is written as;

$$R_{\Delta\eta} = \frac{2(0.7)}{\int_{-0.7}^{0.7} acc(\Delta\eta) d\Delta\eta} = 2 \quad (5.12)$$

The primary concern for the PHENIX experiment for the  $RI$  is the correction factors for the near-side peak in terms of rapidity acceptance. Figure 5.4 illustrates the plot of corrections for  $\Delta\eta$  for the near-side width. These corrections depend on the widths of two systems, namely  $AA$  and  $pp$ . In the event that the ratio of the widths in these two systems differs, minor correction factors are applied to  $R_I$ . Conversely, for the away-side scenario, the corrections for both systems remain constant at 2 and cancel each other out.

**Bleeding Correction** There is an additional correction that is dependent on the widths of the peaks in the correlation function, known as the "bleeding corrections". These corrections account for the possibility that the tails of the near-side Gaussian peaks may extend and reach the other half of the peaks on the away-side, and vice versa. To address this effect, we include the Gaussian tail that leaks from the near-side to the away-side and subtract the Gaussian tail that may have originated from the away-side. Similarly, we include the Gaussian tail that leaks from the away-side to the near-side and subtract the Gaussian tail that may have originated from the near-side. The near-side and away-side regions are separated at an azimuthal angle of  $\pi/2$ , which corresponds to the midpoint between 0 and  $\pi$  angle. The equations used to correct the bleeding effect in  $R_I$  are given by Equation 5.13 and 5.14.

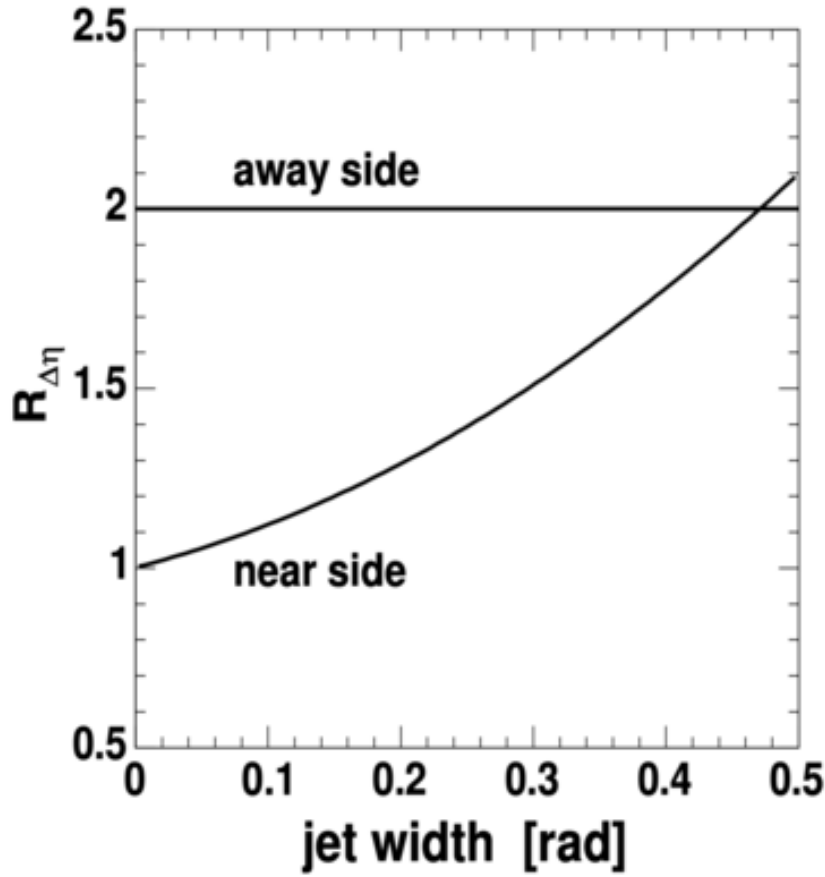


Figure 5.4: PHENIX  $\Delta\eta$  acceptance corrections vs. the jet widths for near-side and away-side. For the near-side, the function looks linear whereas for the away-side corrections is the constant value [23].

$$Y_N = \int_0^{\pi/2} JF(\Delta\phi)d\Delta\phi - \int_0^{\pi/2} Gaus_A(\Delta\phi)d\Delta\phi + \int_{\pi/2}^{\pi} Gaus_N(\Delta\phi)d\Delta\phi \quad (5.13)$$

$$Y_A = \int_{\pi/2}^0 JF(\Delta\phi)d\Delta\phi - \int_{\pi/2}^{\pi} Gaus_N(\Delta\phi)d\Delta\phi + \int_0^{\pi/2} Gaus_A(\Delta\phi)d\Delta\phi \quad (5.14)$$

The first terms come from the histograms of the correlations, whereas the last two terms are calculated from the fitted Gaussian functions. Finally, the corrections are then applied to the yields, which is propagated to  $R_I$  observable.

#### 5.4.4 *Error analysis*

One of the motivations for selecting  $R_I$  as the observable to measure the impact of the QGP on the jets is its ability to mitigate systematic errors. Specifically, uncertainties arising from detector efficiencies are effectively eliminated. This thesis further investigates and analyzes several of these uncertainties, including:

- Statistical uncertainty
- Uncertainty from the mis-constructed  $\pi^0$  combinatorics
- Uncertainty from the ZYAM
- Uncertainty from the bleeding correction
- Uncertainty from  $R_{\Delta\eta}$
- Uncertainty from the  $v_3$  contribution

Statistical uncertainties are handled through the ROOT programming tools. Other systematic uncertainties are elaborated below:

##### 5.4.4.1 **Uncertainty from the Mis-Constructed $\pi^0$ Combinatorics**

Once the sets of cuts have been applied to the photons, they proceed to be reconstructed and contribute to the invariant mass distribution plots. However, it is important to note that not all pairs of reconstructed photons correspond to the genuine decay photons of  $\pi^0$ . There will be other combinations in which two photons do not originate from the same  $\pi^0$ . See Figure 3.1. These instances represent background events that should be subtracted as much

as possible. The true mass of  $\pi^0$  is subject to distortion caused by the smearing effect of the detector, resulting in a deviation from the PDG value of  $0.135 \text{ GeV}/c^2$ . Consequently, we consider a range of  $0.12\text{-}0.16 \text{ GeV}/c^2$  as the region that encompasses the true particles  $\pi^0$ .  $\pi^0$  particles outside this range are commonly referred to as fake  $\pi^0$ . Ideally, the fake  $\pi^0$  should show a similar number of hadron yields per trigger as the nominal  $\pi^0$  region because their photons still come from pi0's of similar momenta. However, it does not happen that way always. Therefore, it is necessary to perform a correlation function analysis using the fake  $\pi^0$  to determine its yield, which allows calculation of systematics (and correction if needed, although we find the correction in this case is small enough to ignore) for the true  $\pi^0$ .

The systematic errors in  $R_I$  caused by fake-pi0 can be determined using the signal-to-background ratio and side-band analysis. Background (B) is obtained by integrating the linear fit of the invariant mass distribution within a range  $2\sigma$  above and below the true pi0 mass of  $0.135$ . Subsequently, the background integral is subtracted from the total integral of the Gaussian fit of the distribution to obtain the signal (S). See Figure 5.5.

Table 5.3: Signal-to-Background (S/B) values for centrality of 20-40% and 65-70% for the  $\pi^0$  trigger- $p_T$  bins of  $5\text{-}7 \text{ GeV}/c$  and  $7\text{-}9 \text{ GeV}/c$ .

Centrality	$\pi^0 p_T (\text{GeV}/c)$ bin	S/B
20-40	5-7	11.48
	7-9	22.48
65-70	5-7	30.25
	7-9	32.01

With the calculation of the S/B ratio, See Table 5.3, we next need to calculate the yields attributed to the fake-pi0. The low-band region for the fake pi0 in the invariant mass distributions is defined as  $0.08\text{-}0.11 \text{ GeV}$ , while the high-band region is defined as

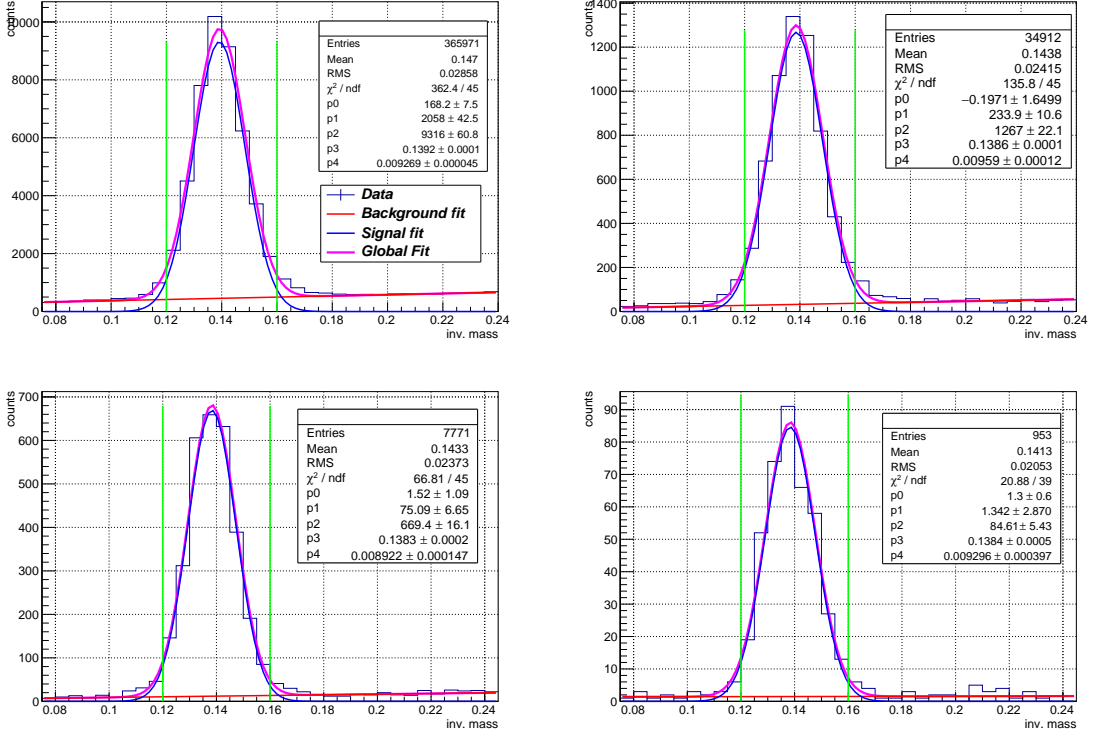


Figure 5.5:  $\pi^0$  invariant mass distribution for  $AuAu$  in Centrality 20 – 40 % (Top row), and 65 – 70 % (Bottom row). The first column is for  $\pi^0$  pT bins of 5-7 and the second column is for  $\pi^0$  pT bins of 7-9. The signal-to-background (S/B) is calculated by dividing the integrals of the blue signal line by the red background line. The integral is calculated within the two green lines, which is also the nominal acceptance region  $\pi^0$  chosen for this analysis.

0.165-0.200 GeV. To calculate the yield, we calculated the  $R_I$  observable itself for both the nominal  $\pi^0$  and side-band regions. Figure 5.6 shows the yields in terms of  $R_I$  for both  $\pi^0$  regions in the case of 20-40% centrality. And figure 5.7 shows the yields in terms of  $R_I$  for both  $\pi^0$  regions in the case of 65-70% centrality.

After we have calculated both quantities, that is, the S/B and the yields, the relative size of the systematics due to the fake  $\pi^0$  is calculated by Equation 5.15 [16].

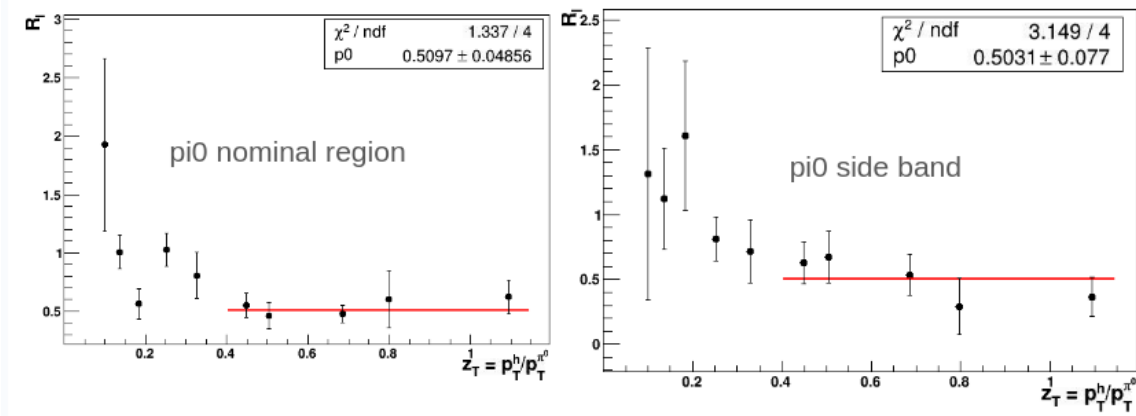


Figure 5.6: Comparisons of yields ( $R_I$ ) for the nominal  $\pi^0$  region and the side-bands region in the case of 20-40% centrality. Left: The red line is a constant fit line showing the average  $R_I$  for high- $p_T$  points to be at  $0.5097 \pm 0.04858$  using the  $\pi^0$  nominal region of selection. Right: The red line shows the fit to the high- $p_T$  values of  $R_I$  showing the average value at  $0.5031 \pm 0.077$  for the  $\pi^0$  from the side-band regions from the  $\pi^0$  nominal region.

$$\frac{\sigma_Y^{\pi^0}}{Y_{Peak}} = \frac{1}{S/B} \left( 1 - \frac{Y_{Side}}{Y_{Peak}} \right) \quad (5.15)$$

where  $Y_{Peak}$  and  $Y_{Side}$  denote the measured yields in the designated  $\pi^0$  region and adjacent regions, respectively.

The analysis reveals that the 20-40% centrality range exhibits negligible systematic effects necessitating corrections. Put differently, the  $\pi^0$  yields per trigger are quite consistent between the nominal  $\pi^0$  region and its neighboring sidebands  $\pi^0$ . In the case of 65-70% centrality, despite a noticeable discrepancy in yields, the Signal-to-Background ratio also influences systematic evaluation. Consequently, the calculated systematics amount to only about 1.9%, indicating a relatively minor impact. In principle this should be applied as a correction, but as we will see in the main result, the statistical errors alone are minimally

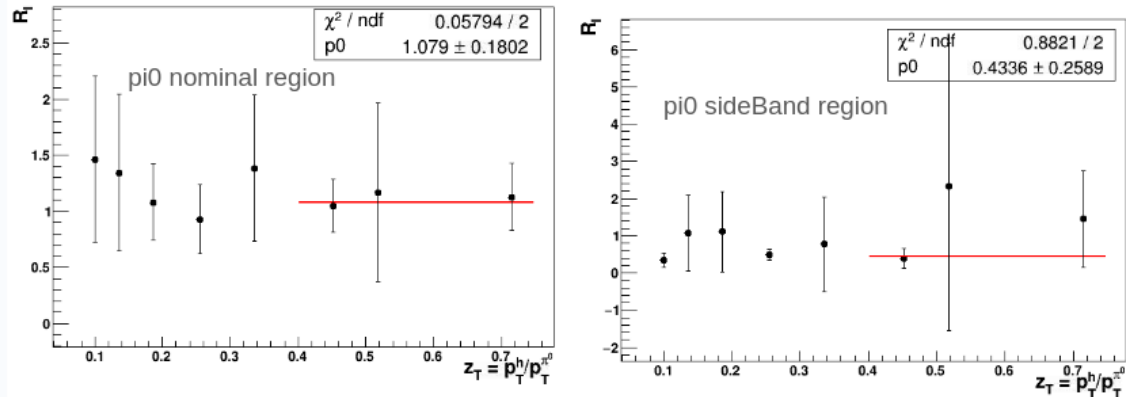


Figure 5.7: Comparisons of yields ( $R_I$ ) for the nominal  $\pi^0$  region and the side-bands region in the case of 65-70% centrality. The plot on the left shows the average  $R_I$  for the last three high- $p_T$  points to be  $1.079 \pm 0.1802$  using the red fit line. It is the plot for  $\pi^0$  in the nominal  $\pi^0$  region of selection. The right plot shows the fit line average value for high- $p_T$  points to be at  $0.4338 \pm 0.2589$ . It is the plot for  $\pi^0$  from the side-bands region of the  $\pi^0$  nominal range.

5 times larger, thus we do not apply the correction itself for these dissertation results, and rather only include it as a systematic error.

#### 5.4.4.2 Uncertainty from ZYAM

The error in the parameter  $b_0$  from the fit of the correlation function plots during the ZYAM applications to determine the background level is used as the uncertainty of the ZYAM level. If we take  $\delta$  as the error in the fit of the ZYAM level, then the yield ratio of the near-to-away side can be written as;

$$\begin{aligned} y &= \frac{a + c\delta}{b + d\delta} \\ &\approx \frac{a}{b} \left[ 1 + \left( \frac{c}{a} - \frac{d}{b} \right) \delta \right] \end{aligned} \tag{5.16}$$

where  $c$  and  $d$  are the integration range for the near- and away-side, respectively, which is  $\pi/2$  for both cases. The systematic error on  $R_I$ , which is the double ratio, due to ZYAM can then be quantified as the root of the sum squares of the collision systems  $pp$  and  $xAu$ , since these systems are not correlated to each other.

$$\sigma_{R_I}^{\text{ZYAM}} = R_I \times \sqrt{\left(\frac{\pi/2}{Y_{xAu}^A} - \frac{\pi/2}{Y_{xAu}^N}\right)^2 \times (\delta_{xAu}^{\text{ZYAM}})^2 + \left(\frac{\pi/2}{Y_{pp}^A} - \frac{\pi/2}{Y_{pp}^N}\right)^2 \times (\delta_{pp}^{\text{ZYAM}})^2} \quad (5.17)$$

#### 5.4.4.3 Uncertainty from Bleeding Correction

The uncertainty attributed to the bleeding effect is determined by taking half of the value of the bleeding correction. The correction is most significant for the lowest transverse momentum ( $p_T$ ) bins where the jet peak widths are much wider than at high  $p_T$ , specifically in the range of 5-7 GeV/c. The correction is derived from the jet width distribution. Due to the double ratio  $R_I$ , the effect is typically partially canceled.

#### 5.4.4.4 Uncertainty from $R_{\Delta\eta}$

The uncertainty in the observable  $R_I$  caused by  $\Delta\eta$  can be determined using the Figure 5.4. As the outside yield remains unaffected by the acceptance of  $\eta$ , the uncertainty arises only from the near-side yield. Therefore, the uncertainty in  $R_I$  is obtained by adjusting the width of the nearside by the error determined from the fitting. This error is then propagated to the near side yield and subsequently to  $R_I$ . Furthermore, since the  $AuAu$  and  $pp$  systems are considered uncorrelated, the total uncertainty in  $R_I$  is calculated by taking the square root of the sum of the squares of the uncertainties associated with these two systems.

#### 5.4.4.5 Uncertainty from the $v_n$

This thesis subtracts the following flow coefficients  $v_2$ ,  $v_3$ , and  $v_4$ . As shown in equation 5.7, to calculate the total flow effects in the correlation functions, coefficients from both trigger  $\pi^0$  and charged hadrons are needed. The PHENIX Collaboration has calculated many

of the flow coefficient measurements in various centrality bins and different  $p_T$  bins for pi0 and charged hadrons such as [46]. Although it is challenging to find an exact match of the flow coefficients for all data bins required for our analysis, the 20-40% centrality case has recently been examined, and the corresponding flow coefficient values for both pi0 and charged hadrons have been used from [16].

For the 65-70% centrality, the RHIC flow coefficients were not available that matched our case. Instead, we used data from the ATLAS experiment at LHC [24]. Figure 5.8 illustrates the flow coefficients for charged hadrons for  $v_2$ ,  $v_3$ , and  $v_4$  measured by the ATLAS experiment.

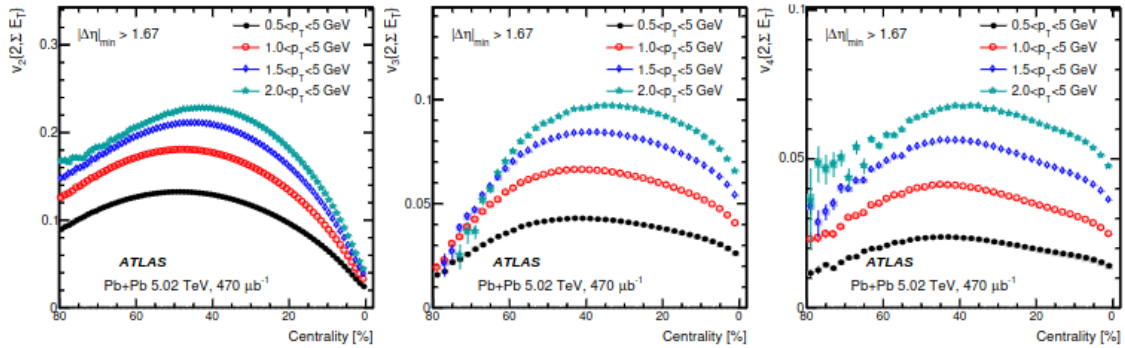


Figure 5.8: The charged hadron higher-order flow coefficients  $v_2$ ,  $v_3$ , and  $v_4$  from the ATLAS experiment [24]. The x-axis shows the centralities from the range of 0 to 80% range for the flow coefficients.

After gathering the flow coefficients of the charged hadrons, we can employ the “acoustic scaling” technique [47] to compute the flow coefficients for the pi0 particles. Acoustic scaling is a method that establishes a connection between higher flow harmonics from the corresponding  $v_2$  coefficients for the same centrality, as described by the equation 5.18;

$$g_n^h = \frac{v_n^h}{(v_2^h)^{n/2}} \quad (5.18)$$

Using the provided data, we are able to determine the  $g_n^h$  values for all charged hadrons. Given the analogous mass composition and properties between all the pi0 siblings, we presume  $g_n^h \sim g_n^{\pi^0}$ . Consequently, we can compute  $v_2$ ,  $v_3$ , and  $v_4$  for  $\pi^0$  particles using equation 5.19.

$$v_n^{\pi^0} = g_n^h (v_2^{\pi^0})^{n/2} \quad (5.19)$$

One caveat to all this is that for 65-70% centrality, the  $v_2$  flow coefficients for both  $\pi^0$  and charged hadrons were derived from prior PHENIX measurements used for to 60-92% centrality. They were already provided in the coding environment and we used it for the convenience given that the systematic uncertainties are small, as depicted in Figure 5.9.

The uncertainty that arises from the flow coefficients must be incorporated into the final results. Fortunately, given the nature of the observable  $R_I$  that we are interested in, systematics due to even flow coefficients cancel each other out when ratios are taken because the even cosine function has equal and flow contributions on both sides namely from  $0 - \pi/2$  and  $\pi/2 - \pi$  of the correlation functions. Additionally, the higher-order even and odd terms of the flow coefficients are nearly negligible. Thus, only the systematics of the  $v_3$  terms need to be calculated. We also exclude the uncertainty from  $v_1$ . To determine the uncertainty due to  $v_3$ , we create final plots of  $R_I$ : one using the  $v_3$  flow coefficients and the other without it. By comparing these overlaid plots, we can ultimately calculate the systematics due to the  $v_3$  effects, as shown in Figure 5.9.

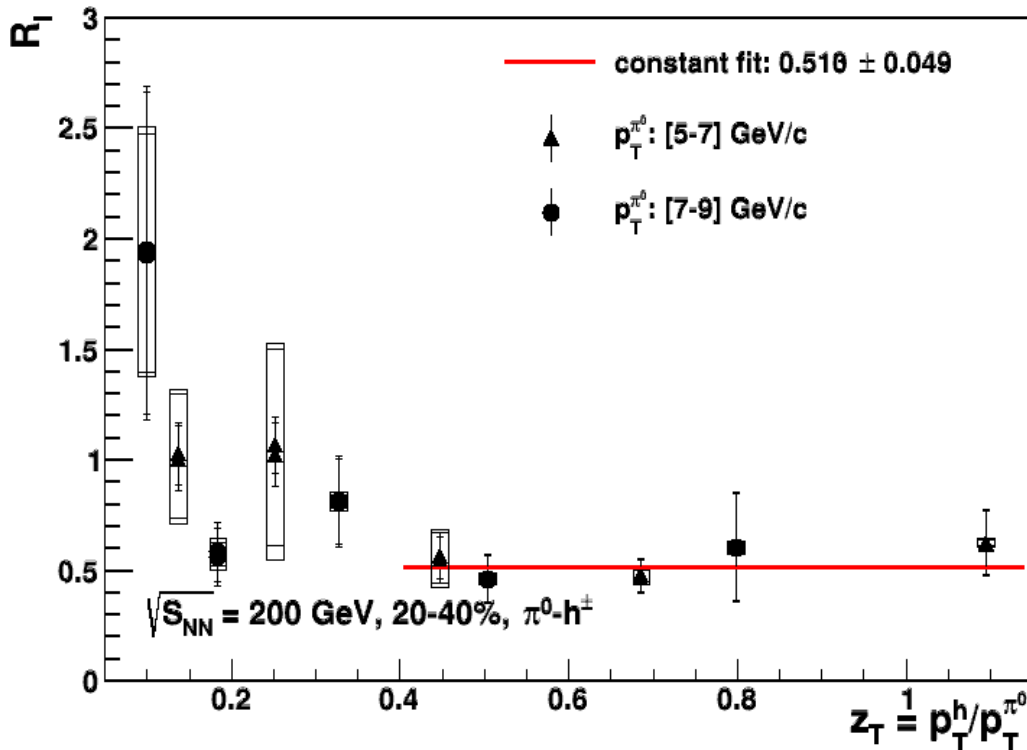


Figure 5.9: The systematics due to the effect of  $v_3$  coefficients on the final  $R_l$  values are calculated by making the  $R_l$  plots with and without  $v_3$  terms used in the calculations. The systematic error values are calculated and shown for each data points.

#### 5.4.4.6 Tabulation of Systematical Uncertainties

The systematic uncertainties are calculated for the following main sources, namely, from ZYAM, bleeding corrections, delta eta corrections, and  $v_n$  flow coefficients. Table 5.4 shows the tabulation of the sizes of the systematic errors in the  $R_l$  values as a percentage for the Run-14 Au+Au collisions with a centrality of 20-40% case. The data tables shown in Appendix B have the absolute values of the sizes of the total statistical and systematic errors for all the  $R_l$  cases.

Table 5.4: Systematic Uncertainties for Run-14 Au+Au Collision data with Centrality bins of 20-40%.

Uncertainty	%	$0.6 < p_T^{h^\pm} < 1$	$1 < p_T^{h^\pm} < 2$	$2 < p_T^{h^\pm} < 3$	$3 < p_T^{h^\pm} < 5$	$5 < p_T^{h^\pm} < 7$
ZYAM	$5 < p_T^\pi < 7$	0.44	0.46	1.26	0.94	0.82
	$7 < p_T^\pi < 9$	1.56	2.14	0.76	1.09	1.34
Bleeding	$5 < p_T^\pi < 7$	2.06	7.05	0.09	2.20e-05	5.19e-03
	$7 < p_T^\pi < 9$	0.96	0.86	3.90e-03	3.15e-05	5.01e-8
Delta Eta	$5 < p_T^\pi < 7$	7.07	3.79	1.93	1.81	1.16
	$7 < p_T^\pi < 9$	11.52	8.91	3.98	1.36	2.07
$v_n$ error	$5 < p_T^\pi < 7$	1	2	1	1	1
	$7 < p_T^\pi < 9$	<1	4	2	2	2

For 65-70% as we will show in the next section, the statistical errors far dominate, making a similar error breakdown for all sources somewhat unreliable. However we find that the propagated error from the  $v_n$  values used in this bin to be conservatively estimated at about 10% at the lowest  $z_T$  point and falling to about 1.5% for highest  $z_T$  points, by comparing the  $R_I$  result with and without  $v_n$  subtraction to the jet functions.

## 6 PHENIX AuAu 2PC ANALYSIS: RESULTS AND DISCUSSIONS

### 6.1 Correlation Function and Jet Function of Baseline pp Collisions

In order to assess the modifications due to QGP that are anticipated to have been produced in heavy-ion collisions, such as Au+Au especially in central collision events, it is essential to establish baseline measurements and remove any contributions from the final results that are not due to QGP. The baseline measurements for this thesis are obtained by analyzing data from Run-15 p+p collisions with a center-of-mass energy of  $\sqrt{S_{NN}} = 200$  GeV, conducted by the PHENIX experiment. Run-15 offers the best statistical precision for the baseline measurements for PHENIX.

Figure 6.1 illustrates the correlation function between  $\pi^0$  and hadrons derived from the PHENIX Run-15  $p + p$  collision dataset. The red curve represents the fits to the entire histogram, while the blue curve indicates the background level obtained using the ZYAM method. For the  $p + p$  baseline collision system, the ZYAM level is determined without incorporating the flow effects which results in the flat-line background shape. The graph is segmented into various trigger  $p_T$  bins and partner  $p_T$  bins. The graph shows two peaks with azimuthal angle differences of 0 and  $\pi$ , which are expected from the back-to-back jets formed during hard-scattered parton collisions.

Figure 6.2 illustrates the jet function derived from the correlation function after subtracting the background level determined by ZYAM. The jet function exhibits good statistics for each bin of trigger and partner  $p_T$ s.

### 6.2 Correlation Function and Jet Function of the Run-14 AuAu Collisions Data

Just like in the  $p + p$  plots shown above, we observe two peaks at the azimuthal angle differences of 0 and  $\pi$  between the trigger and partner particles, which can be attributed to the production of back-to-back jets and the detection capabilities of the PHENIX detector.

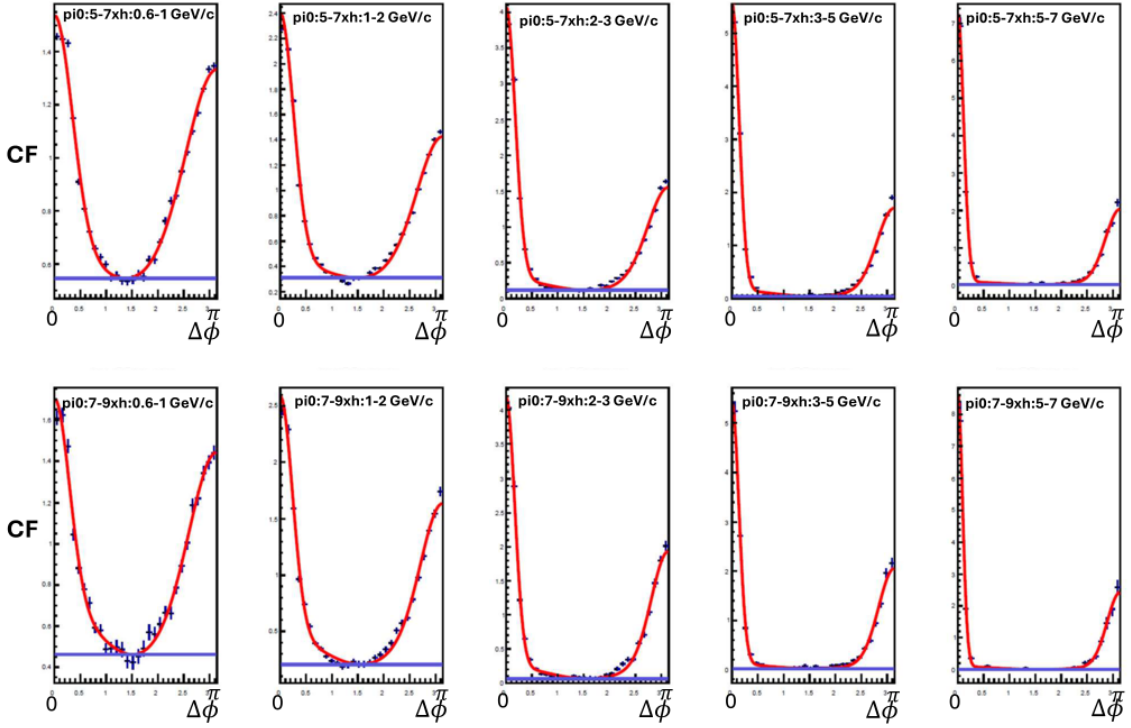


Figure 6.1: Correlation function between  $\pi^0$ -hadrons in the Run-15 p+p collision data. Trigger  $p_T$  bins: [5.0-7.0, 7.0-9.0] GeV/c going along the top to the bottom. Partner  $p_T$  bins: [0.6-1.0, 1.0-2.0, 2.0-3.0, 3.0-5.0 and 5.0-7.0] GeV/c going along the left to right. The red line represents the total fit to the correlation function whereas purple line is the fit to the background level.

### 6.2.1 Run-14 AuAu Collisions For 20-40% Centrality Bins

For Run-14  $Au + Au$  analysis, I have analyzed primarily the two centrality bins, i.e. 20-40% and 65-70%. The correlation function and the jet functions shown in Figures 6.3 and Figure 6.4 correspond to the centrality range of 20 – 40% in Run-14  $Au + Au$  collisions. The 20-40% bin represent more central collision events in which QGP is known to be formed. Consequently, we anticipate observing suppression on the away-side peak due to the QGP effects. The main point of the 20-40% is to demonstrate how the  $R_l$  observable shows the

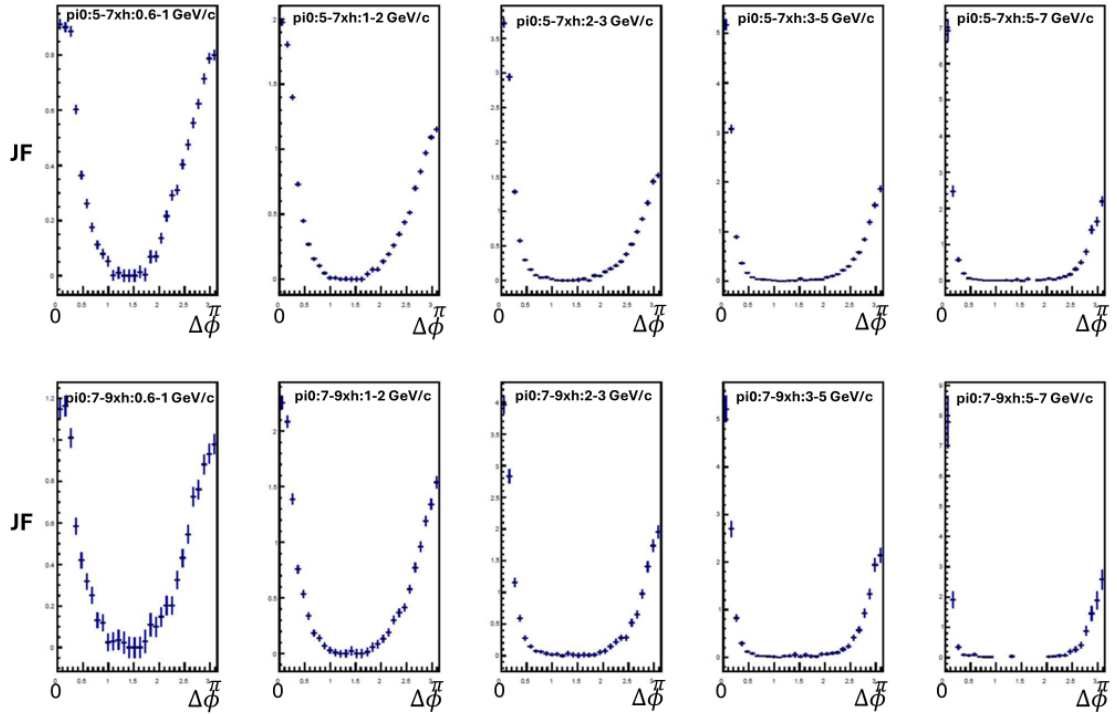


Figure 6.2: Jet function between  $\pi^0$ -hadrons in the Run-15  $pp$  collision data. Trigger  $p_T$  bins: [5.0-7.0, 7.0-9.0] GeV/c going along the top to the bottom. Partner  $p_T$  bins: [0.6-1.0, 1.0-2.0, 2.0-3.0, 3.0-5.0 and 5.0-7.0] GeV/c going along the left to right.

modification for a bin with a known strong suppression signal. The reason we do not choose 0-20% for this comparison is that in the very most central events (0-  $\sim 10\%$ ) there is so much jet quenching that it can also affect the nearside jet peak. Since  $R_I$  also integrates over the near side peak, we avoid using it for most central events, and the 20-40% bin is the next most-central bin which is well explored in other observables as will be discussed.

We observe two peaks at azimuthal differences of approximately 0 and  $\pi$  in all trigger and partner bins. For higher  $p_T$  bins to the right, comparison to the p+p results shows the away-side peaks at  $\pi$  are suppressed at about half the height of the same peaks in p+p. The blue line in Figure 6.3 represents the background level derived from the ZYAM method.

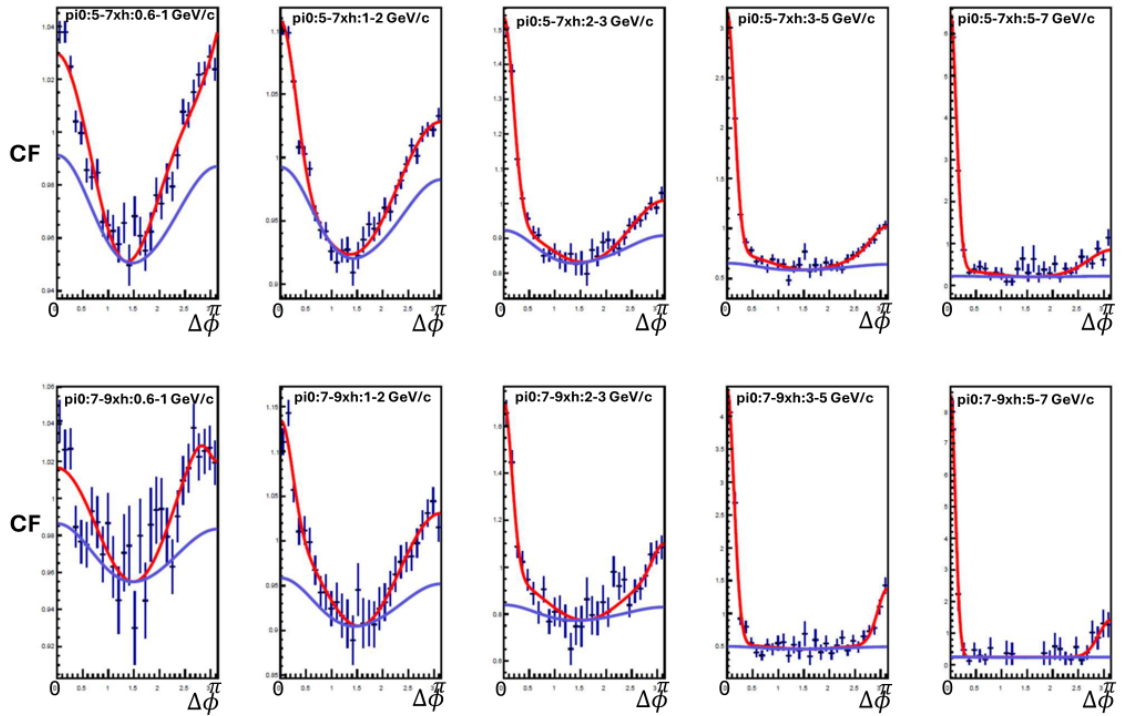


Figure 6.3: Correlation function between  $\pi^0$ -hadrons in the Run-14 AuAu collision data with centrality bins of 20-40%. Trigger  $p_T$  bins: [5.0-7.0, 7.0-9.0] GeV/c going along the top to the bottom. Partner  $p_T$  bins: [0.6-1.0, 1.0-2.0, 2.0-3.0, 3.0-5.0 and 5.0-7.0] GeV/c going along the left to right. The red line is the fit to the total correlation function whereas the purple line represents the fit to the background.

This time due to the flow effects, usually seen in heavy-ion collisions, the background due to flow also has the inherent shapes to it. In central collisions of  $Au + Au$ , the formation of QGP is anticipated, and thus flow is expected. In this case, the ZYAM level is calculated considering the flow effects. We used the flow coefficients  $v_2$ ,  $v_3$ , and  $v_4$  to account for most of the flow effects. The red line corresponds to the fit of the total histogram. Figure 6.4 shows the jet function obtained after subtracting the background from the plot of the corresponding correlation function.

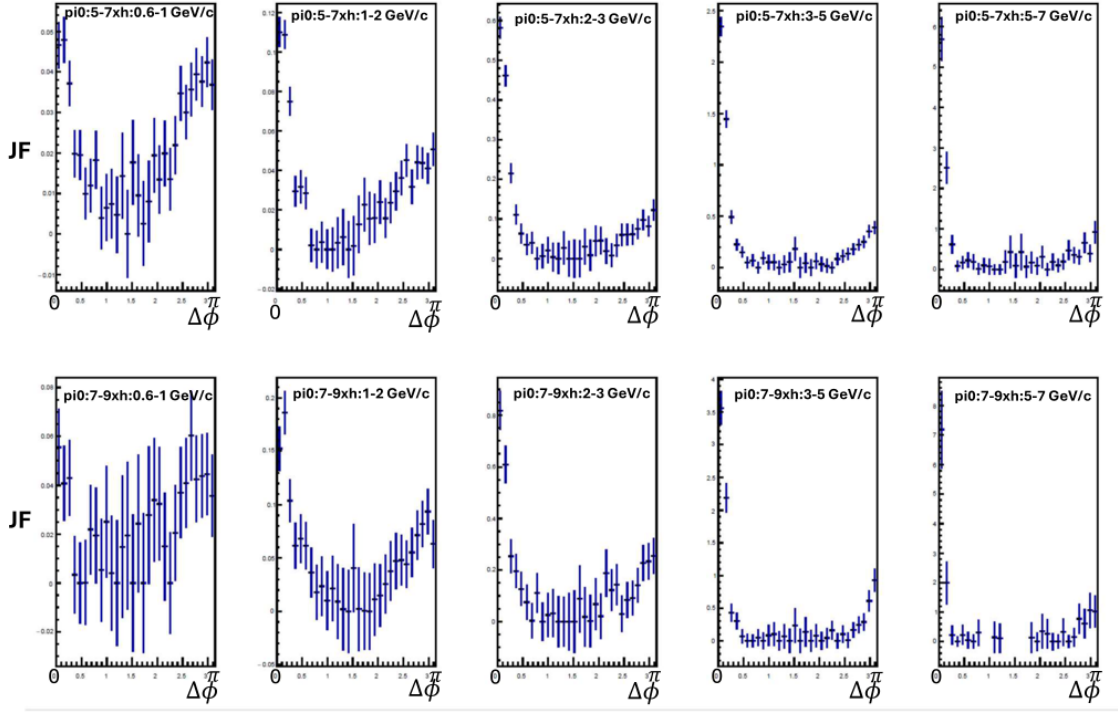


Figure 6.4: Jet function between  $\pi^0$ -hadrons in the Run-14 AuAu collision data with centrality bins of 20-40%. Trigger  $p_T$  bins: [5.0-7.0, 7.0-9.0] GeV/c going along the top to the bottom. Partner  $p_T$  bins: [0.6-1.0, 1.0-2.0, 2.0-3.0, 3.0-5.0 and 5.0-7.0] GeV/c going along the left to right.

### 6.2.2 Run-14 AuAu Collisions For 65-70% Centrality Bins

The correlation function and the jet function for Run-14 AuAu collisions in the centrality range of 65-70% are shown in Figures 6.5 and 6.6. These centrality bins represent the peripheral collision events, where QGP formations are not as well established however, most QGP signatures are found to be present with good significance albeit with much smaller sized modifications. Due to the small sized centrality bin of 5% and the smaller number of effective  $N_{participants}$  the statistics are more marginal in this bin. In fact we exclude the 5-7 GeV/c partner  $p_T$  bin due to insufficient statistics for high  $p_T$  partner particles.

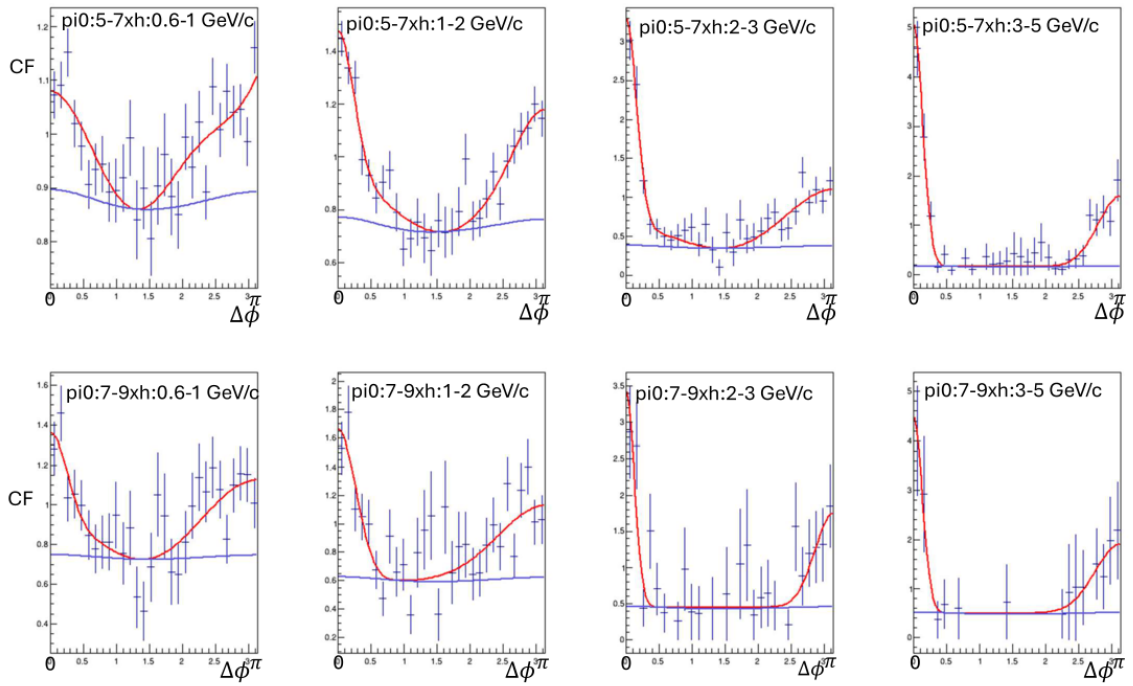


Figure 6.5: Correlation function between  $\pi^0$ -hadrons in the Run-14 AuAu collision data with centrality bins of 65-70%. Trigger  $p_T$  bins: [5.0-7.0, 7.0-9.0] GeV/c going along the top to the bottom. Partner  $p_T$  bins: [0.6-1.0, 1.0-2.0, 2.0-3.0, and 3.0-5.0] GeV/c going along the left to right. The red line represents the fit to the total correlation function whereas the purple line represents the fit to the background level.

Despite less statistics, Figure 6.5 again shows two peaks around azimuthal differences of approximately 0 and  $\pi$  in all trigger and partner bins. The blue line represents the background level derived from the ZYAM method. In this case, the ZYAM level is calculated considering the flow effects, although in such peripheral collisions the flow effect is not much observed. We used the flow coefficients  $v_2$ ,  $v_3$ , and  $v_4$  to account for most of the flow effects. The red line corresponds to the fit of the total data set. Figure 6.6 shows the jet function obtained after subtracting the background from the plot of the corresponding correlation function.

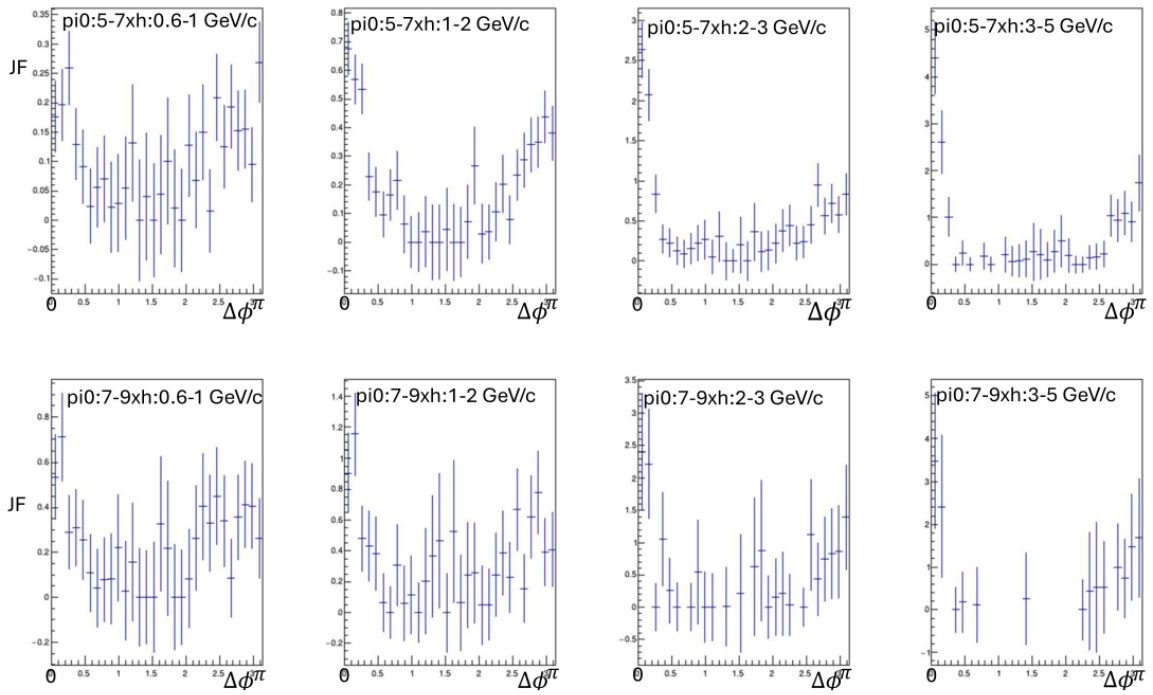


Figure 6.6: Jet function between  $\pi^0$ -hadrons in the Run-14 AuAu collision data with centrality bins of 65-70%. Trigger  $p_T$  bins: [5.0-7.0, 7.0-9.0] GeV/c going along the top to the bottom. Partner  $p_T$  bins: [0.6-1.0, 1.0-2.0, 2.0-3.0, and 3.0-5.0] GeV/c going along the left to right.

### 6.3 $R_I$ Plots

As described in Chapter 5,  $R_I$  observable measures the modifications on the yields of high- $p_T$  particles due to the effects of the QGP. This effect can be realized by the observation of the suppression of the  $R_I$  values for the larger partner  $p_T$  in this study. If  $R_I$  is less than 1, it suggests that a QGP medium has been produced, and thus the yields of the hadrons are reduced. Similarly, if  $R_I$  is 1, it suggests that there is no QGP modification and QGP formation is less likely. We show the  $R_I$  plots for both the 20 – 40% and 65 – 70% centrality bins for Run-14  $Au + Au$  collision data.

### 6.3.1 $R_I$ Plot for Run-14 With 20-40% Centrality

The  $R_I$  plot for the centrality bin of 20 – 40% is shown in Figure 6.7. To make this plot, we have integrated the near-side and away-side jet peak yields from the previous section and also from the Run 15  $p + p$  previously analyzed by Pun [1], and constructed it using equation 5.10, for each of the  $p_T$  bin combinations in the previous section. We choose to plot these data points as a function of the variable  $z_T$  as discussed in section 5.4.3.1.

A notable reduction in  $R_I$  values is observed at high- $z_T$ , whereas an increase is observed at low  $z_T$ , which aligns with the expected behavior when QGP is formed during collision.

As discussed previously, there are several observables that could be used to quantify the jet suppression mechanisms, each of them differ slightly based on sensitiveness to the various parameters of the collisions. One such observable,  $I_{AA}$ , is one of the most widely used observables in the field of heavy ions.  $I_{AA}$  has been recently calculated for the same PHENIX dataset, i.e. Run-14  $Au + Au$  with 20-40% centrality bins by Anthony [16] as shown in Figure 6.8. If we compare the trigger bins  $p_T$  of 5-7 and 7-9 GeV/c with our results of  $R_I$  as shown in Figure 6.7, we can see similar behavior, i.e. the average yields for the high- $p_T$  hadrons are suppressed and has a similar value around 0.5. In that manner, both observables could complement each other's results.  $R_I$  becomes much more precise due to the cancelation of systematics and efficiency effects when searching for smaller signals in peripheral centralities and small system results, which is what we turn to next.

### 6.3.2 $R_I$ Plot for Run-14 With 65-70% Centrality

Figure 6.9 shows  $R_I$  plot for Run-14 AuAu collisions within the centrality range of 65-70%. The statistical error bars are the lines whereas the systematical errors are the boxes around the data points. Just observing the large uncertainty on each data point it is not very significant to make statements on whether there is suppression looking at only individual data points. Averaging all the points above  $z_T \geq 0.25$  with the red constant fit

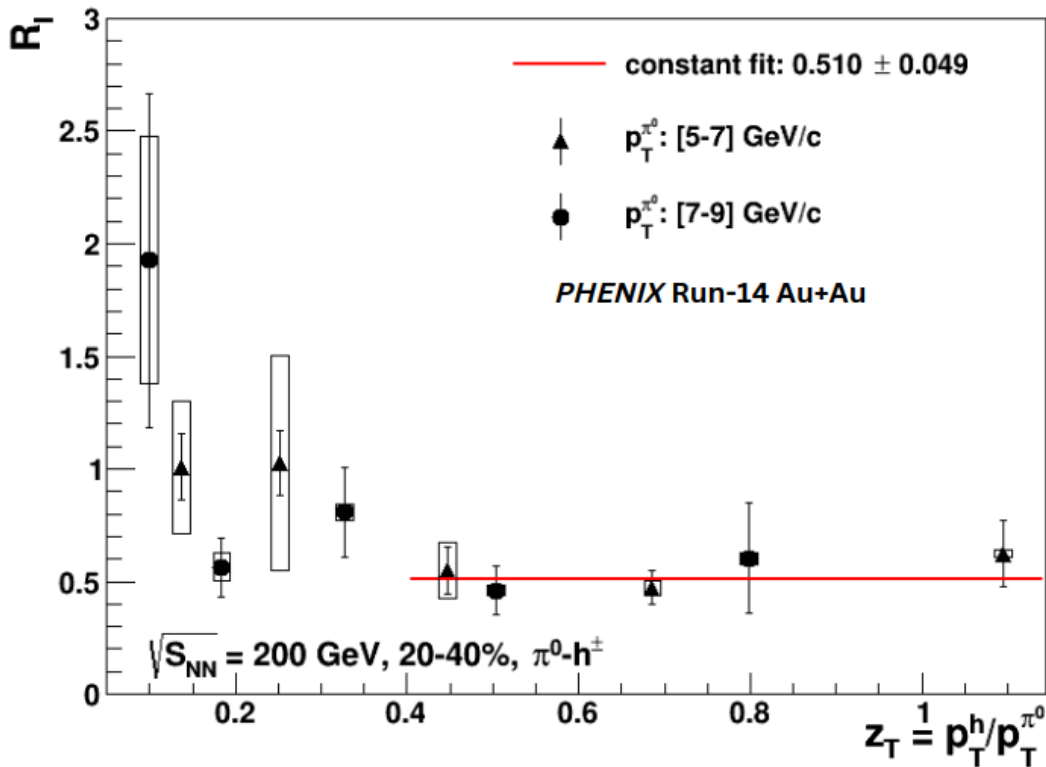


Figure 6.7:  $R_I$  plot of 20-40% Centrality bins of Run-14 Au+Au data with Run-15 p+p data as the baseline. The red line shows the straight line fit to obtain the average value of  $R_I$  for the high- $z_T$ . The average fit value is shown at  $0.510 \pm 0.049$ . The vertical lines represent the statistical error and the systematic errors are shown as the box around the points.

line, the  $R_I$  average is 1.04 with an statistical uncertainty of 0.125. In contrast to the 20-40% centrality bins,  $R_I$  is therefore not suppressed at high  $z_T$ . However the observation of a small enhancement here does not have a high degree of statistical significance, being well consistent with  $R_I = 1.0$ , no modification, and still consistent with  $R_I$  values slightly less than 1. Still especially considering the previous He+Au result, this result might be slightly surprising.

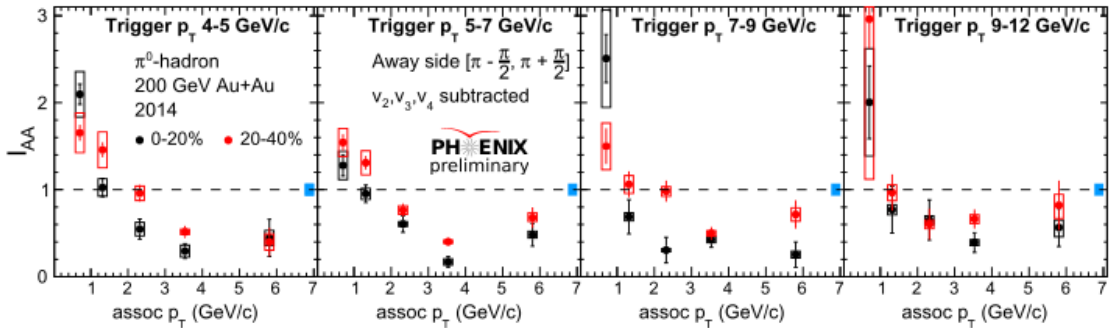


Figure 6.8:  $I_{AA}$  as a function of hadron  $p_T$  for Run-14 Au+Au 20-40% centrality bins [16] used to compare with our  $R_I$  observable with the same centrality and trigger  $p_T$  bins of 5 – 7 GeV/c and 7 – 9 GeV/c.

### 6.3.3 $R_I$ Plot for Run-16 Au+Au With 65-70% Centrality

Because the previous plot might be a slightly surprising result, we wish to cross check it. For this reason, and to possibly improve its statistical precision, we included the full Run-16 dataset statistics and analyzed the 65-70% centrality bin. The procedures for Run-16 were identical to those for Run-14, except for the selection of the good-run-list and hot towers, which differed between the two. Apart from these variations, all cuts applied to the selection of photons, hadrons, and  $\pi^0$ s were consistent.

Figure 6.10 shows the  $R_I$  plot for the Run-16 Au+Au collisions with the 65-70% centrality bins using the Run-15 p+p data as the baseline. As Table 5.2 indicates, the integrated luminosity for this run is about 50% less and we also lost more runs in the QA selection process. The straight line averaging fit shown in the red color again also indicates an average value consistent with 1.05 with even larger uncertainties as compared to Run-14 and also consistent with Run-14 itself. Despite its worse statistics, since the Run-16 is an entirely different dataset occurring two years later than Run-14, this result serves as a nice systematic check of the Run-14 result. Within large uncertainties all points are consistent

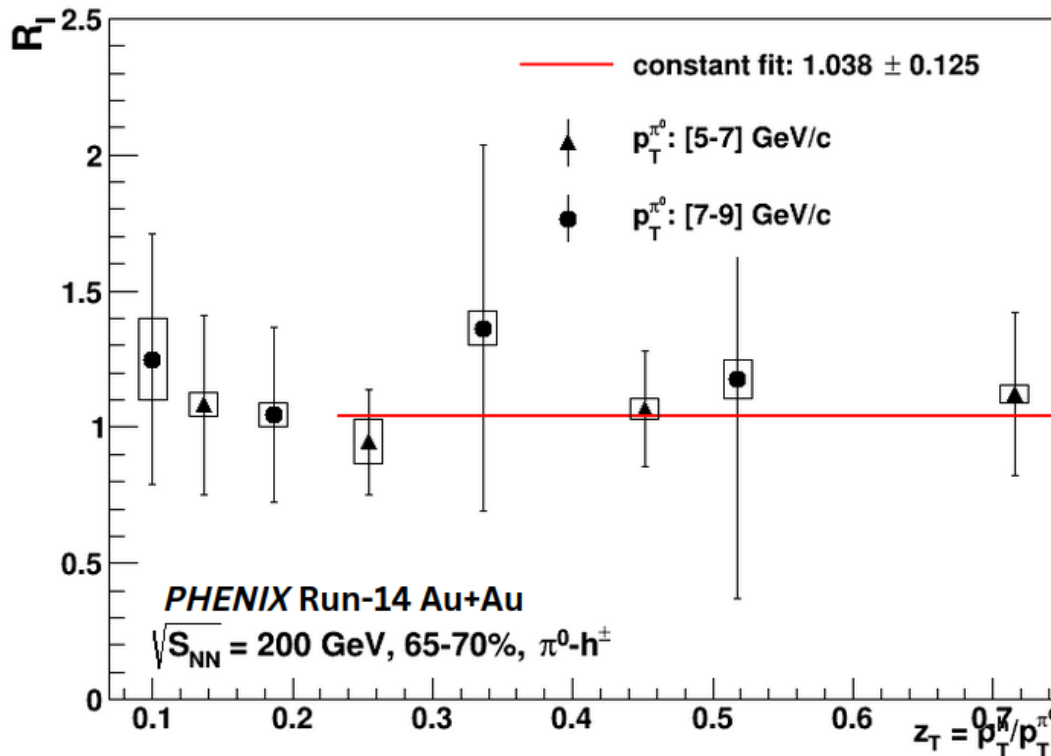


Figure 6.9:  $R_I$  plot of 65-70% Centrality bins of Run-14 Au+Au data with Run-15 p+p data as the baseline. The red line shows the straight line fit to obtain the average value of  $R_I$  for the high- $z_T$ . The average value is shown at  $1.038 \pm 0.125$ . The vertical lines represent the statistical error and the systematic errors are shown in the boxes.

with Run-14. This leads us to even combining the two results in order to maximize the total statistical precision available.

#### 6.3.4 $R_I$ Plot for Combined Data From Run-14 and Run-16

As described in the previous section, having cross-checked the Run-14 result by performing the same measurements again in Run-16, and finding consistency between the two datasets, we decide to maximize the total statistical power of both datasets combined by

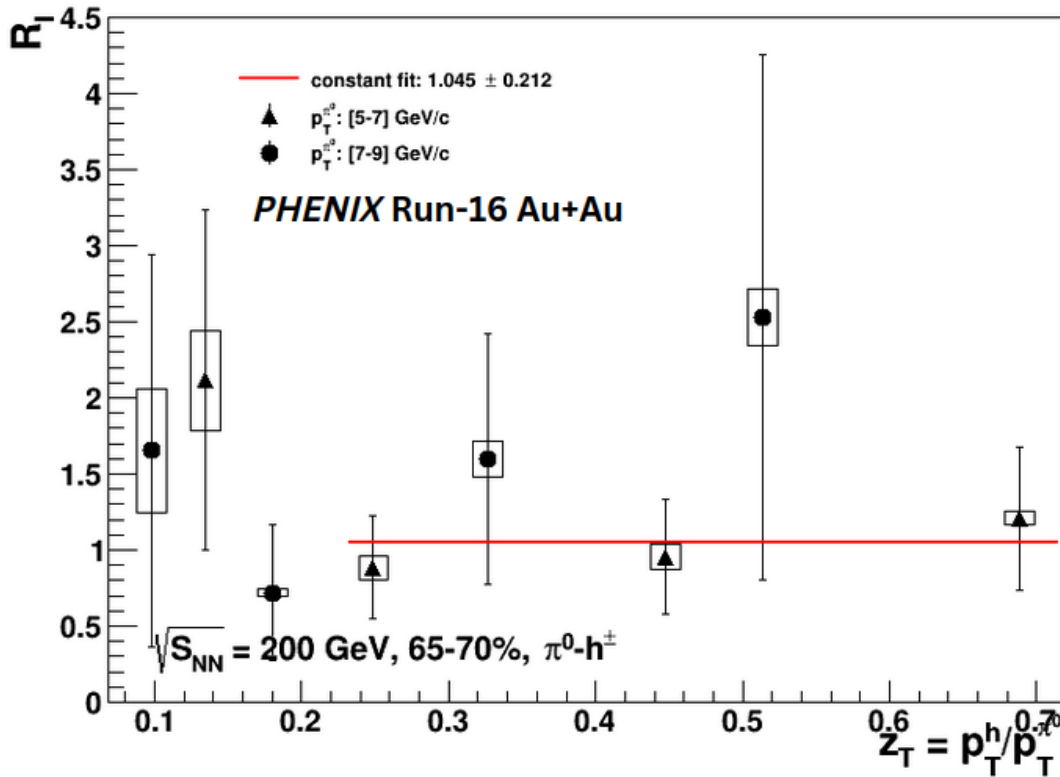


Figure 6.10:  $R_I$  plot of 65-70% centrality bins of Run-16 Au+Au data with Run-15 p+p data as the baseline. The red line shows the straight line fit to obtain the average value of  $R_I$  for the high- $z_T$ . The average values is shown at  $1.045 \pm 0.212$ . The vertical lines represent the statistical error and the systematic errors are showin the boxes.

taking the combined average of the two datasets. For this we use the PDG averaging method [48]. The combined  $R_I$  plot can be seen in Figure 6.11

Not surprisingly, the result is still dominated by the Run-14 result but there is a slight improvement in the relative uncertainty. With the constant fit value being 1.05 with an certainty of 0.123.

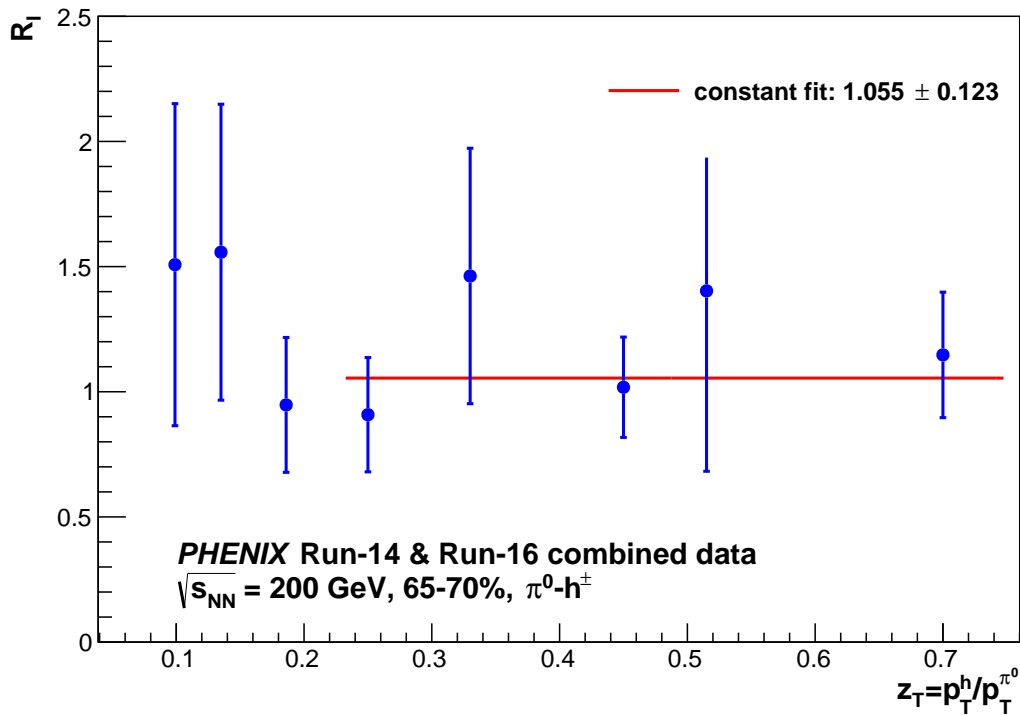


Figure 6.11: RI plot for combined statistics from Run-14 and Run-16 datasets for the centrality bins of 65-70%. The average fit value of  $1.055 \pm 0.123$  is shown by the red line.

#### 6.4 Interpretation and Comparison of $R_l$ of Au+Au Collision Systems With Centrality Bins 65-70% With Previous $R_l$ Plots

Confident that we have maximized the statistical precision that is available in the PHENIX dataset for the 65-70% centrality. We comment further on its significance. As with the Run-14 result alone, we conclude that the  $R_l$  value and thus the amount of suppression modification is very consistent with 1, in fact it is slightly larger than 1 (1.05). Given the statistical uncertainty of 0.12 it could still be consistent with some suppression but it could even also be consistent with some enhancement. Enhancement processes are also possible due to nuclear “Cold Matter” effects such as anti-shadowing and other Nuclear PDF effects,

for reference, such effects were explored extensively for the small system results of  ${}^3\text{He}+\text{Au}$  and  $\text{d}+\text{Au}$ .

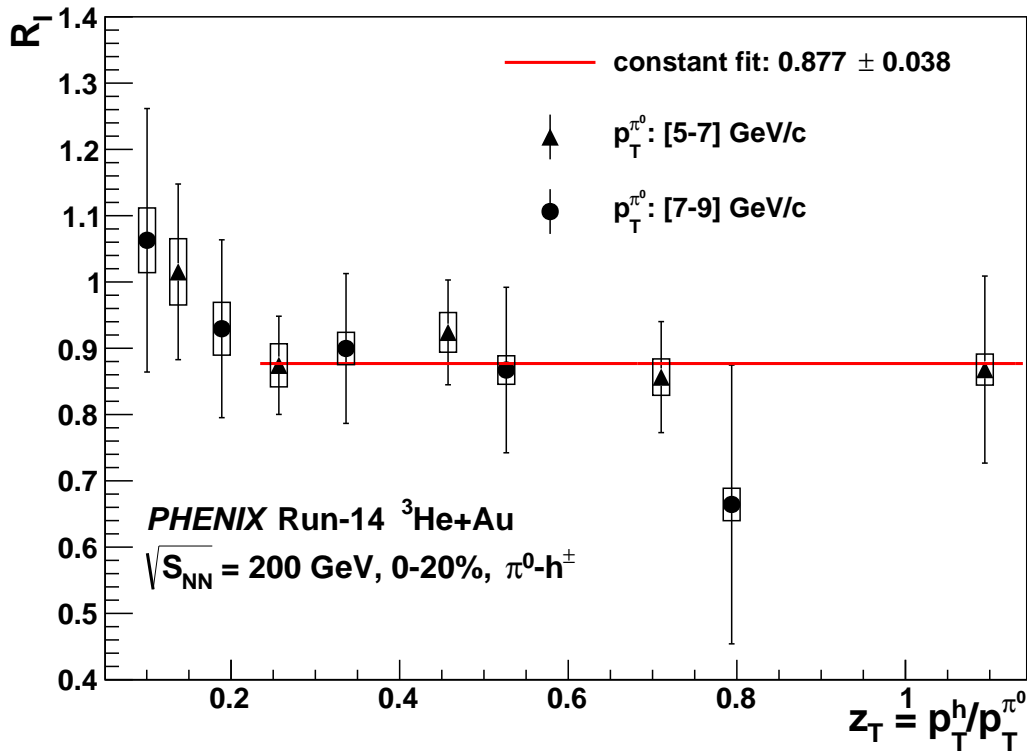


Figure 6.12:  $R_l$  plot for  ${}^3\text{He}+\text{Au}$  reproduced from [1] with more directly comparable new averaging range ( $z_T > 0.25$ ) for comparison to Run-14 and Run-16 datasets 65-70% result. The red-line shows the constant fit to the high  $z_T$  points. The average  $z_T$  shows the value of  $0.877 \pm 0.038$ . The statistical errors are shown by the lines while systematical errors are shown by the boxes.

In Figure 6.12 we refit the  ${}^3\text{He}+\text{Au}$  data to use the same fit range ( $z_T > 0.25$ ) as in the new combined result of Run-14/16 as shown in Figure 6.11. The  ${}^3\text{He}+\text{Au}$  average value is  $0.877 \pm 0.04$ , quite better statistical precision than our  $\text{Au}+\text{Au}$  peripheral results. This represents a mildly statistically significant ( $3 - \sigma$ ) level of overall high  $z_T$  suppression.

In contrast, if we examine our Au+Au 65-70% result from Figure 6.11 of this study to compare, the  $R_l$  observable being at  $1.05 \pm 0.12$  we can see that the results are actually consistent at a level of about  $1.5\sigma$  statistical significance. Taking the interpretation another way, we might say that the results disagree but only at the  $1.5\sigma$  level. Thus we may even go as far as to state that the suppression scenario seen in  ${}^3\text{He}+\text{Au}$  is slightly disfavored, as the result favors a mean value of no suppression or slight enhancement. However, this is not a definitive conclusion due to the uncertainty sizes depicted in Figure 6.11. To enhance this result, a larger dataset would be necessary to achieve sufficient statistics for the 65-70% centrality bins. Given that we have maximized the available statistics for this analysis available from PHENIX, we have shown that the answer will have to remain uncertain using only PHENIX data. Luckily however, sPHENIX will soon provide much higher data collection rates and factors of 10-100 times more data than that was available in PHENIX.

## 7 SUMMARY AND FUTURE OUTLOOK

We analyze the Run-14 and Run-16 Au+Au datasets from the PHENIX experiment at  $\sqrt{s_{NN}} = 200$  GeV, focusing on two different centrality ranges: 20- 40% and 65- 70%. We produced the final  $R_l$  plots exclusively from Run-14 data to compare these results with a previous study on the same system and found that the results of our system were consistent with those of the previous study. Subsequently, we created a combined statistical plot using the Run-14 and Run-16 Au+Au datasets to achieve better statistics, particularly for the peripheral centrality case of 65-70%. For baseline data, we used the Run-15 p+p dataset. The 20-40% centrality  $R_l$  plot indicated suppression of high- $p_T$  charged hadrons and enhancement at low- $p_T$ , consistent with the concept that high-energy partons lose energy to the QGP medium via soft-gluon radiation. However, due to substantial statistical uncertainty, we were unable to definitively conclude whether jets were suppressed in the 65-70% centrality case. We further specifically aimed to compare the peripheral centrality findings of this study with previous research from our Ohio group, mainly involving small systems such as d+Au and  $^3\text{He}+\text{Au}$ , which have similar numbers of participating nucleons during collisions. The simplest explanation would be that if a QGP were produced, they should have generated a similarly sized QGP for all these mentioned systems, especially between  $^3\text{He}+\text{Au}$  and 65-70% Au+Au, assuming the QGP size depends only on the number of participating nucleons. Our Au+Au result can neither confirm nor deny that assumption, as quantitatively as the two results are consistent at only about the  $1.5 \sigma$  statistical level. In other words, their level of disagreement could with high probability be simply a statistical fluctuation. On the other hand the Au+Au values being slightly enhanced at a value of 1.05 (a result supported independently by both the Run14 and Run16 data independently) could slightly disfavor this simplest expectation of QGP size *vs.* number of participating nucleons, (for example indicating other nuclear physics effects) but only with very very small statistical significance.

The primary objective of such data analyses using experimental data is to support theoretical models to understand the characteristics of QGP matter. Increased analysis leads to better understanding. Looking ahead, it is crucial to note that examining peripheral centralities, such as the 65-70% range we attempted, requires a significant volume of data sets. In upcoming RHIC runs, the sPHENIX experiment will collect considerably more Au+Au collision datasets. This will be interesting for investigating and determining whether jets are suppressed in these peripheral centrality bins with reduced uncertainty.

As part of this thesis, we also developed new techniques for improving the sPHENIX EMCal calibration which will directly benefit the  $\pi^0$  analysis and specifically doing a much higher precision  $\pi^0 - h^\pm R_l$  analysis. Therefore, hopefully with the new statistically larger and improved-calibration sPHENIX data included, the data from all these systems regarding the suppression levels of jets by the QGP would provide us with a more comprehensive and complete understanding of how the QGP effects depend on the system size of the collisions.

## REFERENCES

- [1] A. Pun, *Measurements of Di-Jet  $\pi^0 - h^\pm$  Correlations in Light-Heavy Ion Collisions at RHIC-PHENIX*. PhD thesis, Ohio University, 2019.
- [2] Wikipedia, “Standard model.” [https://en.wikipedia.org/wiki/Standard\\_Model](https://en.wikipedia.org/wiki/Standard_Model). [Accessed on Dec 20, 2022].
- [3] G. Prosperi, M. Raciti, and C. Simolo, “On the running coupling constant in QCD,” *Progress in Particle and Nuclear Physics*, vol. 58, pp. 387–438, Apr. 2007.
- [4] J. Gayler, “Proton Structure Function Measurements from HERA,” in *Multiparticle Dynamics*, pp. 274–279, July 2003. arXiv:hep-ex/0211051.
- [5] M. P. McCumber, *Measurement of Fast Parton Interactions with Hot Dense Nuclear Matter via Two-Particle Correlations at PHENIX*. PhD thesis, Stony Brook University, 2009.
- [6] A. Collaboration, K. Aamodt, B. Abelev, A. Abrahantes Quintana, *et al.*, “Higher Harmonic Anisotropic Flow Measurements of Charged Particles in Pb-Pb Collisions at  $s_{NN} = 2.76 \text{ TeV}$ ,” *Physical Review Letters*, vol. 107, p. 032301, July 2011.
- [7] P. Collaboration, S. S. Adler, S. Afanasiev, C. Aidala, N. N. Ajitanand, *et al.*, “High transverse momentum meson production in  $p + p$ ,  $d + Au$ , and  $Au + Au$  collisions at  $s_{NN} = 200 \text{ GeV}$ ,” *Physical Review C*, vol. 75, p. 024909, Feb. 2007.
- [8] J. Adams, C. Adler, M. M. Aggarwal, *et al.*, “Evidence from  $d + A$  Measurements for Final-State Suppression of High-  $p_T$  Hadrons in  $A + A$  Collisions at RHIC,” *Physical Review Letters*, vol. 91, p. 072304, Aug. 2003.
- [9] B. Abelev, J. Adam, D. Adamová, and ALICE Collaboration, “ $K^*(892)0$  and  $(1020)$  production in Pb-Pb collisions at  $s_{NN} = 2.76 \text{ TeV}$ ,” *Physical Review C*, vol. 91, p. 024609, Feb. 2015.
- [10] “Relativistic heavy ion collider.” <https://www.flickr.com/photos/brookhavenlab/7979381212/blah/>. Accessed on Jan 25, 2024.
- [11] “Configuration Diagram Run 14.” <https://www.phenix.bnl.gov/runs/run14.html>. Accessed on Jan 25, 2024.
- [12] K. Adcox, S. Adler, and M. Aizama, “PHENIX detector overview,” *Nuclear Instruments and Methods in Physics Research Section A: Accelerators, Spectrometers, Detectors and Associated Equipment*, vol. 499, Mar. 2003.
- [13] S. Aronson, J. Bowers, J. Chiba, *et al.*, “PHENIX magnet system,” *Nuclear Instruments and Methods in Physics Research Section A: Accelerators, Spectrometers, Detectors and Associated Equipment*, vol. 499, pp. 480–488, Mar. 2003.

- [14] T. Nakamura, “Introduction of PHENIX BBC.” [https://phenix-intra.sdcc.bnl.gov/phenix/WWW/intro/detectors/focus/focus\\_bbc.pdf](https://phenix-intra.sdcc.bnl.gov/phenix/WWW/intro/detectors/focus/focus_bbc.pdf). Accessed on Jan 28, 2024.
- [15] M. Chiu *et al.*, “RHIC Zero Degree Calorimeter.” [https://phenix-intra.sdcc.bnl.gov/phenix/WWW/intro/detectors/focus/focus\\_zdc.pdf](https://phenix-intra.sdcc.bnl.gov/phenix/WWW/intro/detectors/focus/focus_zdc.pdf). Accessed on Jan 28, 2024.
- [16] A. Hodges, *Jet-Like Correlations in 200 GeV Au+Au Collisions*. PhD thesis, Georgia State University, 2022.
- [17] Y. Akiba, R. Begay, J. Burward-Hoy, *et al.*, “Ring imaging Cherenkov detector of PHENIX experiment at RHIC,” *Nuclear Instruments and Methods in Physics Research Section A: Accelerators, Spectrometers, Detectors and Associated Equipment*, vol. 433, pp. 143–148, Aug. 1999.
- [18] L. Aphecetche, T. Awes, J. Banning, *et al.*, “PHENIX calorimeter,” *Nuclear Instruments and Methods in Physics Research Section A: Accelerators, Spectrometers, Detectors and Associated Equipment*, vol. 499, pp. 521–536, Mar. 2003.
- [19] S. Milov, “Centrality determination using BBC in Au+Au and Cu+Cu collisions at  $\sqrt{s_{NN}} = 200$  gev,” *PHENIX internal Analysis Note*, 461.
- [20] M. L. Miller, K. Reygers, S. J. Sanders, and P. Steinberg, “Glauber Modeling in High Energy Nuclear Collisions,” *Annual Review of Nuclear and Particle Science*, vol. 57, pp. 205–243, Nov. 2007. arXiv:nucl-ex/0701025.
- [21] A. Sickles, “Introduction of sPHENIX Physics Programs.” sPHENIX Internal Meetings, 2022.
- [22] The sPHENIX Collaboration, “sPHENIX Technical Design Report (2019).” <https://indico.bnl.gov/event/7081/>. [Accessed on Dec 17, 2023].
- [23] S. S. Adler, S. Afanasiev, C. Aidala, *et al.*, “Jet properties from dihadron correlations in p + p collisions at s = 200 GeV,” *Physical Review D*, vol. 74, p. 072002, Oct. 2006.
- [24] M. Aaboud, G. Aad, B. Abbott, The ATLAS collaboration, *et al.*, “Fluctuations of anisotropic flow in Pb+Pb collisions at  $\sqrt{s_{NN}} = 5.02$  TeV with the ATLAS detector,” *Journal of High Energy Physics*, vol. 2020, p. 51, Jan. 2020.
- [25] The CMS collaboration, V. Khachatryan, A. M. Sirunyan, *et al.*, “Observation of long-range, near-side angular correlations in proton-proton collisions at the LHC,” *Journal of High Energy Physics*, vol. 2010, no. 9, p. 91, 2010.
- [26] B. Xia,  $\pi^0 - h^\pm$  Jet Correlations in d + Au Collisions at  $\sqrt{S_{NN}} = 200$  GeV. Phd thesis, Ohio University, 2014.

- [27] J. L. Nagle and W. A. Zajc, “Small System Collectivity in Relativistic Hadronic and Nuclear Collisions,” *Annual Review of Nuclear and Particle Science*, vol. 68, pp. 211–235, Oct. 2018.
- [28] “The PHENIX Detector.” <https://www.bnl.gov/rhic/phenix.php>. [Accessed on Dec 9, 2023].
- [29] “The sPHENIX Detector.” <https://www.bnl.gov/rhic/sphenix.php>. [Accessed on Dec 9, 2023].
- [30] D. J. Griffiths, *Introduction to elementary particles*. Weinheim: Wiley, 2., rev. ed., 5. reprint ed., 2011.
- [31] M. G. Mann, “A SCHEMATIC MODEL OF BARYONS AND MESONS,” *PHYSICS LETTERS*, 1964.
- [32] H. D. Politzer, “Reliable Perturbative Results for Strong Interactions?,” *Physical Review Letters*, vol. 30, pp. 1346–1349, June 1973.
- [33] K. G. Wilson, “Confinement of quarks,” *Physical Review D*, vol. 10, pp. 2445–2459, Oct. 1974.
- [34] F. Gross, E. Klemp, S. J. Brodsky, and e. Buras, “50 Years of Quantum Chromodynamics,” *arXiv:2212.11107*, 2022.
- [35] G. ATLAS Collaboration, Aad, B. Abbott, J. Abdallah, *et al.*, “Observation of Long-Range Elliptic Azimuthal Anisotropies in  $s = 13$  and 2.76 TeV p p Collisions with the ATLAS Detector,” *Physical Review Letters*, vol. 116, p. 172301, Apr. 2016.
- [36] The PHENIX Collaboration, “An Introduction to PHENIX.” <https://phenix-intra.sdcc.bnl.gov/phenix/WWW/intro/detectors/index.html>. Accessed on Jan 28, 2024.
- [37] PHENIX Collaboration, J. C. Gregory, *et al.*, “PHENIX: Preliminary conceptual design report,” 6 1992.
- [38] C. Adler, A. Denisov, E. Garcia, M. Murray, H. Strobele, and S. White, “The RHIC zero-degree calorimeters,” *Nuclear Instruments and Methods in Physics Research Section A: Accelerators, Spectrometers, Detectors and Associated Equipment*, vol. 499, pp. 433–436, Mar. 2003.
- [39] “Notes on PHENIX Software.” <https://www.phenix.bnl.gov/software/overview.html>. [Accessed on Dec 3, 2023].
- [40] R. Belmont, J. Brewer, Q. Brodsky, *et al.*, “Predictions for the sPHENIX physics program,” *Nuclear Physics A*, vol. 1043, p. 122821, Mar. 2024.

- [41] C. A. Aidala *et al.*, “Design and Beam Test Results for the 2-D Projective sPHENIX Electromagnetic Calorimeter Prototype,” *IEEE Trans. Nucl. Sci.*, vol. 68, no. 2, pp. 173–181, 2021.
- [42] C. A. Aidala, S. Altaf, R. Belmont, *et al.*, “Design and Beam Test Results for the 2D Projective sPHENIX Electromagnetic Calorimeter Prototype,” 2020.
- [43] Particle Data Group, M. Tanabashi, K. Hagiwara, *et al.*, “Review of Particle Physics,” *Physical Review D*, vol. 98, p. 030001, Aug. 2018.
- [44] sPHENIX Collaboration, “sPHENIX Collaboration coresoftware.” [https://github.com/sPHENIX-Collaboration/coresoftware/tree/master/calibrations/calorimeter/calo\\_emc\\_pi0\\_tbt](https://github.com/sPHENIX-Collaboration/coresoftware/tree/master/calibrations/calorimeter/calo_emc_pi0_tbt). Accessed on Jan 29, 2024.
- [45] A. Aprahamian and others (NSAC), “Reaching for the horizon: The 2015 long range plan for nuclear science,” 10 2015.
- [46] PHENIX Collaboration, A. Adare, S. Afanasiev, C. Aidala, *et al.*, “Measurement of two-particle correlations with respect to second- and third-order event planes in Au + Au collisions at  $\sqrt{s_{NN}} = 200$  GeV,” *Physical Review C*, vol. 99, p. 054903, May 2019.
- [47] R. A. Lacey, A. Taranenko, J. Jia, N. N. Ajitanand, and J. M. Alexander, “Scaling of the higher-order flow harmonics: implications for initial-eccentricity models and the “viscous horizon”,” Aug. 2011. arXiv:1105.3782 [nucl-ex].
- [48] Particle Data Group, “Averages and fits.” <https://pdg.lbl.gov/2019/reviews/rpp2019-rev-rpp-intro.pdf>. Accessed on Jul 8, 2024.

## APPENDIX: LIST OF ACRONYMS

List of some of the acronyms that I have used in the thesis.

- Au+Au - Collisions between Two Gold nucleus
- BBC - PHENIX Beam-Beam Counter detector
- d+Au - Collisions between deuterium and gold nucleus
- DAQ - Data Acquisition
- DC - PHENIX Drift Chamber Detector
- EMCal - Electromagnetic Calorimeter
- ERT - EMCal/RICH Trigger
- $h^\pm$  - charged hadrons
- $^3\text{He}+\text{Au}$  - Collisions between helium and gold nucleu
- MB - Minimum Bias, a category of RHI events defined by the minimal requirements to call it an event (single collision where there was scattering)
- MBD - sPHENIX Minimum Bias detector
- PbSc - Lead Scintillator Calorimeter
- PbGl - Lead Glass Calorimeter
- PCX (PC, PC1, PC2, PC3) PHENIX Pad Chamber detector level X.
- PHENIX - Pioneering High Energy Nuclear Interaction eXperiment
- Pi0 -  $\pi^0$  meson

- p+p - Collisions between Two protons
- QCD - Quantum Chromodynamics
- QGP - Quark-Gluon Plasma
- RHIC - Relativistic Heavy Ion Collider
- RICH - Ring Imaging Cherenkov Detector
- SDCC - Scientific Data and Computing Center
- sPHENIX - super PHENIX (not official)
- LHC - Large Hadron Collider
- ZDC - Zero-Degree Calorimeters

## APPENDIX: DATA TABLE FOR $R_I$ OBSERVABLE ALONG WITH ERRORS

### B.1 Data Table of $R_I$ Values for Run-14 Au+Au Collisions

Table B.1:  $R_I$  values of Run-14 Au+Au with 20-40% centrality

Trig  $p_T$  5-7 GeV/c

partner $p_T$ GeV/c	$R_I$	$z_T$	Statistical Error	Systematic Error
0.6 - 1.0	1.00833	0.136636	$\pm 0.146851$	$\pm 0.292783$
1.0 - 2.0	1.02706	0.251469	$\pm 0.141702$	$\pm 0.475582$
2.0 - 3.0	0.548927	0.44764	$\pm 0.103289$	$\pm 0.125574$
3.0 - 5.0	0.473866	0.685915	$\pm 0.0737107$	$\pm 0.0324604$
5.0 - 7.0	0.623246	1.09432	$\pm 0.14515$	$\pm 0.0154205$

Trig  $p_T$  7-9 GeV/c

0.6 - 1.0	1.92678	0.0998454	$\pm 0.741596$	$\pm 0.546807$
1.0 - 2.0	0.564182	0.1839	$\pm 0.130247$	$\pm 0.0610225$
2.0 - 3.0	0.807617	0.32776	$\pm 0.198876$	$\pm 0.0367114$
3.0 - 5.0	0.460795	0.503659	$\pm 0.110253$	$\pm 0.02111$
5.0 - 7.0	0.60422	0.798202	$\pm 0.245835$	$\pm 0.0255919$

Table B.2:  $R_I$  values of Run-14 Au+Au with 65-70% centrality

---

Trig $p_T$ 5-7 GeV/c				
partner $p_T$ GeV/c	$R_I$	$z_T$	Statistical Error	Systematic Error
0.6 - 1.0	1.08323	0.136673	$\pm 0.329404$	$\pm 0.0426921$
1.0 - 2.0	0.946366	0.254435	$\pm 0.192349$	$\pm 0.0825501$
2.0 - 3.0	1.06615	0.451527	$\pm 0.213469$	$\pm 0.039084$
3.0 - 5.0	1.12029	0.715236	$\pm 0.298676$	$\pm 0.0331868$

Trig $p_T$ 7-9 GeV/c				
partner $p_T$ GeV/c	$R_I$	$z_T$	Statistical Error	Systematic Error
0.6 - 1.0	1.24979	0.100168	$\pm 0.461653$	$\pm 0.149045$
1.0 - 2.0	1.04773	0.186448	$\pm 0.320949$	$\pm 0.0434918$
2.0 - 3.0	1.36314	0.336031	$\pm 0.672438$	$\pm 0.0626444$
3.0 - 5.0	1.17575	0.517646	$\pm 0.805294$	$\pm 0.0715755$

## B.2 Data Table of $R_I$ Values for Run-16 Au+Au Collisions

Table B.3:  $R_I$  values of Run-16 Au+Au with 65-70% centrality

---

Trig $p_T$ 5-7 GeV/c				
partner $p_T$ GeV/c	$R_I$	$z_T$	Statistical Error	Systematic Error
0.6 - 1.0	2.11355	0.134897	$\pm 1.11746$	$\pm 0.324764$
1.0 - 2.0	0.884209	0.248863	$\pm 0.338035$	$\pm 0.0778947$
2.0 - 3.0	0.955638	0.447874	$\pm 0.374906$	$\pm 0.0822949$
3.0 - 5.0	1.20783	0.688039	$\pm 0.473206$	$\pm 0.0427406$

Trig $p_T$ 7-9 GeV/c				
partner $p_T$ GeV/c	$R_I$	$z_T$	Statistical Error	Systematic Error
0.6 - 1.0	1.65227	0.0983648	$\pm 1.28955$	$\pm 0.402265$
1.0 - 2.0	0.720786	0.180485	$\pm 0.446091$	$\pm 0.0241358$
2.0 - 3.0	1.59698	0.326805	$\pm 0.821553$	$\pm 0.116085$
3.0 - 5.0	2.52811	0.513647	$\pm 1.72839$	$\pm 0.188151$